

University of St Andrews



Full metadata for this thesis is available in
St Andrews Research Repository
at:

<http://research-repository.st-andrews.ac.uk/>

This thesis is protected by original copyright

Novel Interferometric Techniques and Surface Profilometry

J Paul Lesso

December 20, 1999



Tu Dk 82

Abstract

In this thesis several novel interferometric techniques for surface profilometry are described. In chapter 1 there is a review of the techniques used for profilometry: both non-interferometric, such as use of a stylus, and interferometric, such as phase shifting.

In chapters 2-3 of this thesis the proposal, analysis and demonstration of a novel interferometric technique based on polarisation analysis are featured. This technique uses Stokes parameters and sources with a short coherence lengths to remove any ambiguity associated with fringe counting. Both modelled and experimental results are presented.

Wave plates are used in the technique described above and it is critical that the appropriate wave plate is used. Chapter 4 therefore contains the description of an in-depth discussion of a technique that is appropriate for analysing birefringent wave plates to accurately determine the polarisation state emerging from them for short coherence length pulses.

New research concepts relating to ray propagation in birefringent material are introduced and described in chapters 5 and 6. In birefringent materials Snell's law is not obeyed and ray tracing is considerably more complex. For this reason a ray-tracer was written for birefringent materials and this was used to analyse aberrations in birefringent lenses.

A novel design for a shearing interferometer that can be used for the identification of defects lying within a corrugated surface is introduced in chapter 7. This interferometer uses spatially incoherent light and the design is analysed and experimental results presented.

This subject matter of chapter 8 relates to a detailed analysis of the polarisation properties of Dove prisms. These prisms were used in the shearing interferometer described in chapter 7, but the interesting behavioral characteristic that they rotate the image but not the polarisation is afforded particular consideration.

“Nature and Nature’s laws lay hid in night,
God said, ‘Let Newton be’, and all was light” -A.Pope

Acknowledgements

I would like to thank my supervisors Miles and Wilson for their help and support. Also I would like to thank Shell Research Limited, and Dr Bill Hirst in particular, for their support. Thanks to everybody at St Andrews and also to Roz, Dave and Julian for helping to keep my sanity.

Also I wish to thank the late Alan Duncan for his insight and friendship through out my Ph.D.

Certification

- (i) I, Paul Lesso, hereby certify that this thesis, which is approximately 25,000 words in length, has been written by me, that it is the record of work carried out by me and that it has not been submitted in any previous application for a higher degree.

Date : September 1999

Signature of candidate. . . .

- (ii) I was admitted as a research student in October 1996 and as a candidate for the degree of Ph.D. in October 1996; the higher study for which this is a record was carried out in the University of St Andrews between 1996 and 1999.

Date : September 1999

Signature of candidate. . . .

- (iii) I hereby certify that the candidate has fulfilled the conditions of the Resolution and Regulations appropriate for the degree of Ph.D. in the university of St Andrews and that the candidate is qualified to submit this thesis in application for that degree.

Date : September 1999

Signature of supervisor.

- (iv) In submitting this thesis to the University of St Andrews I understand that I am giving permission for it to be made available for use in accordance with the regulations of the University Library for the time being in force, subject to any copyright vested in the work not being affected thereby. I also understand that the title and abstract will be published, and that a copy of the work may be made and supplied to any bona fide library or research worker.

Date : September 1999

Signature of candidate. . . .

Contents

1	Profilometry Techniques	1
1.1	Profilometry methods	1
1.1.1	Time of flight	1
1.1.2	Focus Methods	2
1.1.3	Stylus Methods	5
1.2	Interferometers	6
1.2.1	Michelson Interferometer	7
1.2.2	Mirau Interferometer	8
1.2.3	Linnik Interferometer	9
1.2.4	Common path interferometers	9
1.3	Interferometric Techniques	14
1.3.1	Phase Stepping	14
1.3.2	White Light	15
1.3.3	Multiple Wavelength	16
1.3.4	Limitations of interferometric Techniques	16
1.4	Summary	17
2	Surface profilometry based on polarisation analysis	18
2.1	Mathematical Analysis	20
2.1.1	Stokes parameters	22
2.1.2	The degree of polarisation	24
2.1.3	Degree of Coherence	24
2.2	Experimental setup	25
2.3	Results	28
2.4	Quantative results	30
2.5	Conclusions	32
3	Further Analysis of μ_{xy}	34
3.1	Numerical modeling	34
3.1.1	Numerical modelling results	35
3.2	Polariser mis-alignment	37

3.3	Wave plate errors	38
3.3.1	Poincaré Sphere	38
3.3.2	Mis-matched wave plate	40
3.4	Chromatic and achromatic wave plates	42
3.4.1	$p_{3(chrom)}$ <i>vs.</i> p_3	44
3.5	$ \mu_{xy} $ and the Fourier transform	45
3.5.1	Sinc spectrum	46
3.6	Hanbury-Brown and Twiss interferometer	47
3.7	Conclusions	48
4	Modelling the performance of birefringent wave plates	49
4.1	Polarisation state of light	49
4.2	Modelling the performance of various wave plate designs . . .	50
4.2.1	Sellmeier Data	52
4.3	Design of birefringent wave plates	53
4.4	Numerical investigation of various design of wave plate	55
4.5	Conclusions	59
5	Ray Tracing in Birefringent Media	61
5.1	Fermat's principle	62
5.2	Huygen's Construction	63
5.3	Snell's Law	64
5.3.1	Vectorial form of Snell's Law	64
5.4	Ray tracing in birefringent media	65
5.4.1	Variable refractive index	65
5.4.2	Poynting Vector <i>vs.</i> the wave vector	67
5.5	Ray Tracing algorithm	68
5.5.1	o-ray	68
5.5.2	e-ray	69
5.6	Conclusions	71
6	Aberrations and birefringent lenses	72
6.1	Assessment of the accuracy of the ray-tracing package	73
6.2	Aberrations	74
6.2.1	Spherical Aberration	76
6.2.2	Coma	77
6.2.3	Astigmatism	77
6.2.4	Field Curvature	77
6.2.5	Distortion	79
6.3	Bending lenses to reduce aberrations	79
6.4	Wavefront Analysis	81

6.4.1	Zernike Polynomials	83
6.5	Calculations of aberrations introduced by a birefringent lens	84
6.6	Combined aberrations	87
6.7	Conclusions	89
7	Compensated shearing interferometry	95
7.1	Regular surface structure	95
7.2	Low Reflectivity	97
7.3	Spatially coherent light sources	98
7.4	Illumination Optics	98
7.5	Imaging optics	100
7.6	Experimental Results	101
7.7	Conclusions	102
8	Dove prisms and polarised light	104
8.1	Dove prism design	105
8.2	Jones matrix analysis of Dove prisms	106
8.3	Experimental results	108
8.4	Conclusions	110
	Bibliography	111
A	Publications	122
B	Mathematica code used for modelling μ_{xy}	124
C	Achromatic wave plates	132
D	Mathematica code used to model wave plates	133
E	Mathematica code for birefringent ray tracer	140

List of Tables

2.1	Comparison of AFM profiling to $ \mu_{xy} $ profiling	31
4.1	Sellmeier coefficients for various materials	53
4.2	Tungsten bulb source centered at $800nm$, predicted values of p_3 for various quarter wave plate designs	56
4.3	Femto-second laser source centered at $780nm$, predicted values of p_3 for various quarter wave plate designs	56
4.4	Filtered white light centered at $633nm$ with $1nm$ bandwidth, predicted values of p_3 for various quarter wave plate designs	56
4.5	Tungsten bulb source centered at $800nm$, predicted values of p_3 for various half wave plate designs	57
4.6	Femto-second laser source centered at $780nm$, predicted values of p_3 for various half wave plate designs	58
4.7	Filtered white light centered at $633nm$ with $1nm$ bandwidth, predicted values of p_3 for various half wave plate designs	58
6.1	Zernike Polynomials up to 4^{th} order and corresponding aberrations	83

List of Figures

1.1	A simple surface profiler using an cylindrical lens.	3
1.2	Examples of images on photodetector of profiler using a cylindrical lens	3
1.3	System using imaging properties to locate focus.	4
1.4	A transmission confocal microscope	4
1.5	A reflection confocal microscope	5
1.6	A micro-lens based confocal microscope which only requires scanning in the z -direction.	6
1.7	A diamond stylus profiling a wafer.	7
1.8	A Michelson Interferometer.	8
1.9	Two different Mirau configurations.	9
1.10	A Linnik interferometer.	10
1.11	A Wollaston prism splitting a beam.	11
1.12	A Wollaston prism with a lens to form a shearing interferometer.	11
1.13	A Wollaston prism being used to introduce a phase difference between orthogonal components.	12
1.14	Pictures of a micro-chip when viewed with an ordinary and Nomarski microscope objectives.	13
1.15	Images showing image with phase discontinuities and resulting image when phase discontinuities have been removed.	15
2.1	Electric field of two orthogonally polarised pulses overlapping and their resultant polarisation.	19
2.2	A Michelson interferometer	20
2.3	Layout of interferometer	26
2.4	Photograph of working interferometer	27
2.5	Graph showing relationship between $ \mu_{xy} $ and pulse overlap d for a Gaussian spectrum	29
2.6	Diagram showing steps to generate $ \mu_{xy} $. Note all six polarisation measurements are shown for simplicity, where only four are actually measured.	29
2.7	Figure showing white light image and $ \mu_{xy} $ data.	30

2.8	3D profile of wafer generated from $ \mu_{xy} $ data.	31
2.9	3D profile of wafer generated from $ \mu_{xy} $ data.	32
2.10	AFM scan of Silicon wafer	33
2.11	Profile of silicon wafer determined by $ \mu_{xy} $	33
3.1	Graph showing how p_1 varies with pulse overlap for a sample with $\rho = 0.6$	36
3.2	Graphs showing how p_2 and p_3 varies with pulse overlap . . .	36
3.3	Graphs showing how P and $ \mu_{xy} $ vary with pulse overlap . . .	37
3.4	$ \mu_{xy} $ vs. d curves with polariser mis-alignment	38
3.5	Poincaré Sphere	39
3.6	Various points on a Poincaré corresponding to use of different wave plates.	40
3.7	p_2/p_3 plane in Poincaré Sphere	40
3.8	Graph showing perturbations arising in the $ \mu_{xy} $ curve due to wave plate mis-match	41
3.9	Figure showing $ \mu_{xy} $ measured with a zero order chromatic wave plate for for two different source with different coherence lengths.	44
3.10	Graphs showing the ratio of $p_{3(chrom)}$ to p_3 for two different situations.	45
3.11	A sinc ² power spectrum and resultant $ \mu_{xy} $ curve.	47
3.12	A Hanbury-Brown and Twiss interferometer. (A Mirrors, B Amplifiers, C multiplier, M Integrator)	48
4.1	Phase imparted by a quartz zero-order quarter wave plate (black line) and by an achromatic quarter wave plate (wave plate 1 in the tables) (grey table) optimised for 780nm	54
5.1	A point being imaged to a point, showing the wavefronts in the system.	62
5.2	Huygen's construction for isotropic media	63
5.3	Wave velocity surface for isotropic media	64
5.4	Wave velocity surface for birefringent media	66
5.5	Graph showing how refractive index varies with input angle and input plane for Calcite	67
5.6	Huygen's construction for the e-ray in birefringent media . . .	68
5.7	Rays traveling in birefringent media.	69
5.8	Relevant vectors for determining the path of the o-ray in birefringent media.	69

5.9	Relevant vectors for determining the path of the e-ray in birefringent media.	69
6.1	A calcite birefringent lens showing its two focal lengths.	72
6.2	A birefringent telescope comprising two birefringent lenses with their optic axes perpendicular to each other.	74
6.3	Interferograms and modelled results for various lens separations in a telescope comprising two birefringent lenses with perpendicular optic axes.	75
6.4	Output from ray tracer showing longitudinal and transverse spherical aberration	76
6.5	Figure showing how coma arises	77
6.6	Astigmatism in a birefringent lens	78
6.7	A lens imaging a plane and its field curvature	78
6.8	Various kinds of distortion	79
6.9	A variety of lenses and their corresponding SFs.	80
6.10	Interferograms arising from interference of a plane wave and aberrated wavefront.	82
6.11	Graphs showing how spherical aberration of a birefringent lens varies with shape factor (SF) for the o-ray (solid line) and the e-ray(dashed line).	85
6.12	Graphs showing how coma varies in birefringent calcite and quartz lenses as a function of shape factor (SF). The solid line shows how coma varies for the o-ray. The two dashed lines show how coma varies for the e-ray when the incident ray bundle is parallel to the optic axis (short dashes) and perpendicular to the optic axis (long dashes).	86
6.13	Graphs showing how astigmatism varies with shape factor (SF) for the e-ray in a birefringent lens. The solid lines are for a lens of thickness 0.5cm and the dashed lines for a lens of thickness 0.4cm	88
6.14	The geometrical spot diagrams for Calcite lens with shape factor (SF) = -1 and focal lengths $f_o \approx 90mm$ and $f_e \approx 120mm$ at $f/8$. All spot diagrams are contained in squares of dimensions $100\mu m$ by $100\mu m$. Δz represents the distance away from the circle of least confusion.	90
6.15	The geometrical spot diagrams for Calcite lens with shape factor (SF) = -0.5 and focal lengths $f_o \approx 90mm$ and $f_e \approx 120mm$ at $f/8$. All spot diagrams are contained in squares of dimensions $100\mu m$ by $100\mu m$. Δz represents the distance away from the circle of least confusion.	91

6.16	The geometrical spot diagrams for Calcite lens with shape factor (SF) = 0 and focal lengths $f_o \approx 90mm$ and $f_e \approx 120mm$ at $f/8$. All spot diagrams are contained in squares of dimensions $100\mu m$ by $100\mu m$. Δz represents the distance away from the circle of least confusion.	92
6.17	The geometrical spot diagrams for Calcite lens with shape factor (SF) = 0.5 and focal lengths $f_o \approx 90mm$ and $f_e \approx 120mm$ at $f/8$. All spot diagrams are contained in squares of dimensions $100\mu m$ by $100\mu m$. Δz represents the distance away from the circle of least confusion.	93
6.18	The geometrical spot diagrams for Calcite lens with shape factor (SF) = 1 and focal lengths $f_o \approx 90mm$ and $f_e \approx 120mm$ at $f/8$. All spot diagrams are contained in squares of dimensions $100\mu m$ by $100\mu m$. Δz represents the distance away from the circle of least confusion.	94
7.1	Illustration of how shearing interferometry can be used to remove surface structure.	96
7.2	A shearing interferometer with its illumination and imaging arms separated	97
7.3	Illumination arm of interferometer	99
7.4	Field of view of a calcite Wollaston prism $5mm$ thick for $\lambda = 633nm$	100
7.5	Imaging arm of interferometer	101
7.6	Detailed layout of compensated shearing interferometer.	102
7.7	Experimental results showing the effect of using shearing interferometry to remove regular surface structure.	103
8.1	A Dove prism acting as an image inverter	104
8.2	Measured intensity of a He-Ne laser after transmission through a rotating Dove prism placed between crossed and parallel polarisers	106
8.3	Transmitted intensity through various designs of rotating Dove prism placed between parallel and crossed polarisers	109

Chapter 1

Profilometry Techniques

In this chapter some of the more common techniques used in profilometry are reviewed. In particular these include use of a mechanical stylus, measuring focus error and interferometry.

1.1 Profilometry methods

Whilst the main thrust of research in profilometry uses interferometric techniques there exist many other approaches to profilometry. This section looks at a whole series of different techniques and contrasts and compares them.

1.1.1 Time of flight

The simplest possible technique for profilometry is to send a pulse of light out and time how long it takes to return. If this is repeated for many points across a sample it is possible to determine the profile of the sample. Recently this technique has been expanded to use time-correlated single-photon counting[1]. This technique uses the statistical properties of single-photon counting to achieve accuracies of less than $30\mu m$ from distances of to $5m$

away from the sample. Chirped pulses have also been shown to have useful application in time of flight methods [2].

1.1.2 Focus Methods

There are a whole class of profilometry methods which use the imaging properties of light to determine the focus mis-match.

Astigmatic Lenses

A commonplace example is that of a CD reader. In this system an astigmatic or cylindrical lens is used. A simple setup is used as shown in figure 1.1. The cylindrical lens images a point to a point when focussed. However when the system is not correctly focussed elliptical beams are obtained as shown in figure 1.2. Figure 1.2 (a) shows the light on the photodetector for correctly focussed system, (b) and (c) show the ellipticity for being on either side of focus. A four element photo-diode is used to detect the signal and the error signal is given by the difference between $(a + c)$ and $(b + d)$ [3]. The lens is scanned until the error signal is zero. This technique is used to scan over the head of CDs to maintain the focus and hence determine the sequence of bits on the surface.

Mis-focus

Using the setup shown in figure 1.3 it is possible to measure focus mis-match. By judicious placing of the spatial filters in front of detectors $D1$ and $D2$ when the sample is shifted there will be a change in focal position and hence one detector will receive less power and one detector more. By comparing the two signals it is possible to detect which way the sample has shifted.

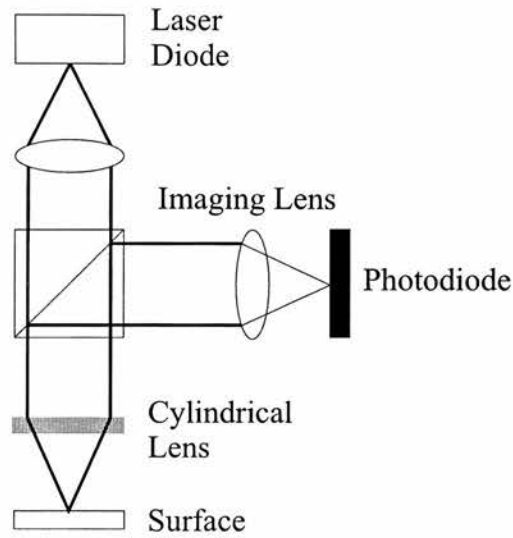


Figure 1.1: A simple surface profiler using an cylindrical lens.

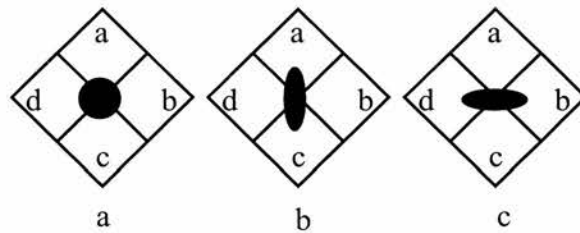


Figure 1.2: Examples of images on photodetector of profiler using a cylindrical lens

Confocal

A confocal microscope uses a pinhole in the back focal plane of the light collecting lens to increase the performance of the system. A simple transmission confocal microscope is shown in figure 1.4.

For surface profilometry a confocal microscope is normally used in a reflection setup [4] as shown in figure 1.5. When the object's surface passes through the focus a high intensity maximum is achieved. This can be used in conjunction with scanning to determine the height of the surface, just like

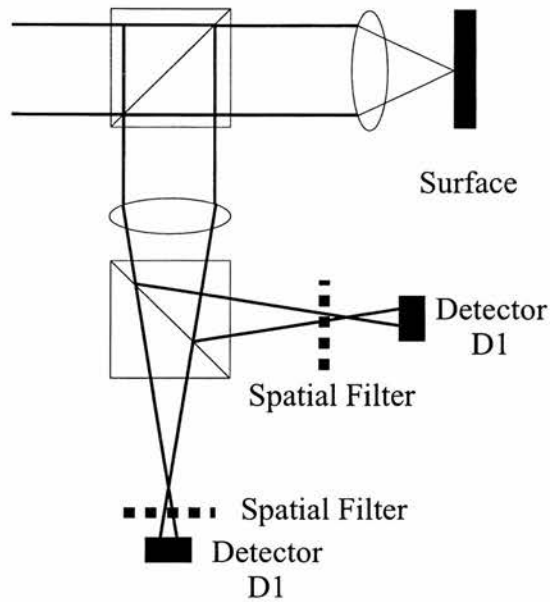


Figure 1.3: System using imaging properties to locate focus.

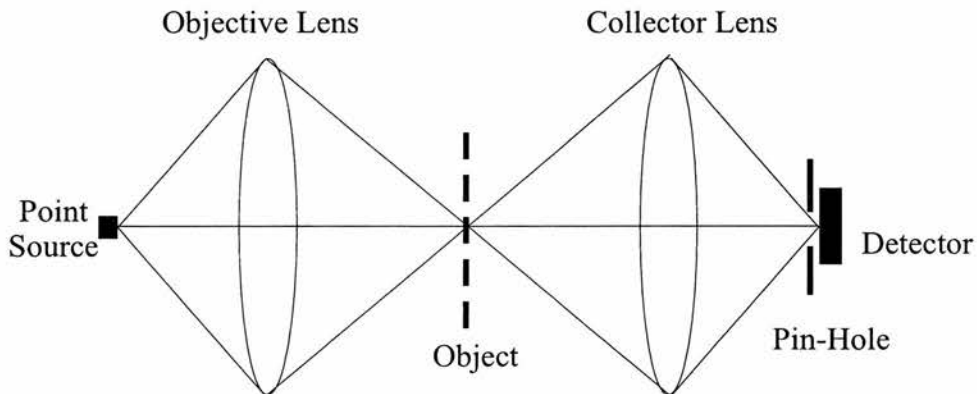


Figure 1.4: A transmission confocal microscope

peak coherence methods for white light interferometry. However confocal microscopy requires to be scanned in the $x - y$ plane as well as the z plane since only one point is imaged.

The intensity $I(u)$ of a point object placed on the optic axis is given by

$$I(u) = \left[\frac{\sin \frac{u}{2}}{\frac{u}{2}} \right]^2 \quad (1.1)$$

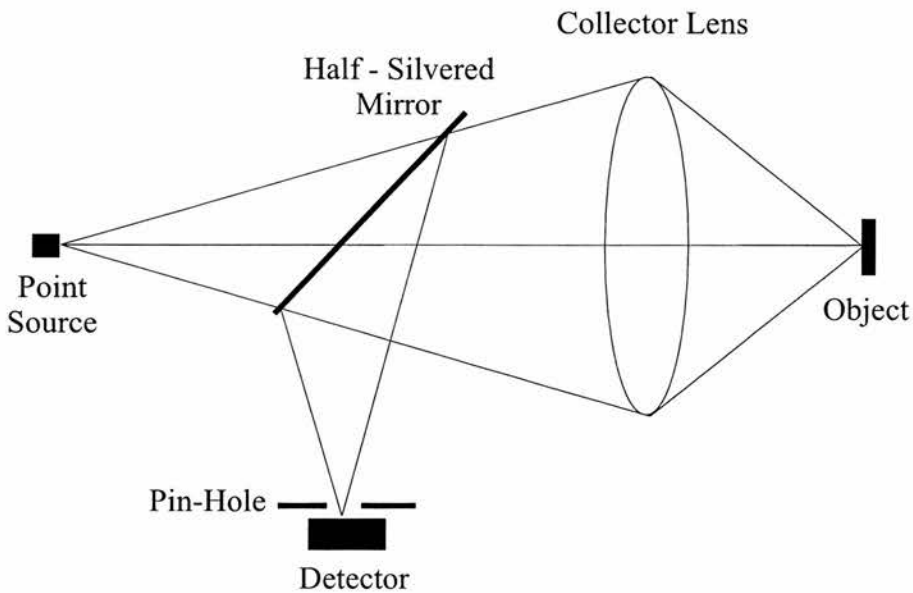


Figure 1.5: A reflection confocal microscope

where u is related to the axial distance z is given by

$$u = 2\pi/\lambda(NA)^2z \quad (1.2)$$

More recently the mechanical scanning techniques described above have been superseded by purely optical techniques[5]. The techniques use a micro-lens array to image the surface, as shown in figure 1.6. The micro-lens array effectively images many points simultaneously removing the need for scanning in the $x - y$ plane[6].

1.1.3 Stylus Methods

Stylus methods involve use of a small stylus which is mounted on an arm. The stylus is moved over the surface and the stylus is dragged along and it follows the surface in much the same way that a record player moves its arm across a record. Figure 1.7 shows a diamond stylus made by VITO. A major problem with stylus techniques is the time they take to scan a surface

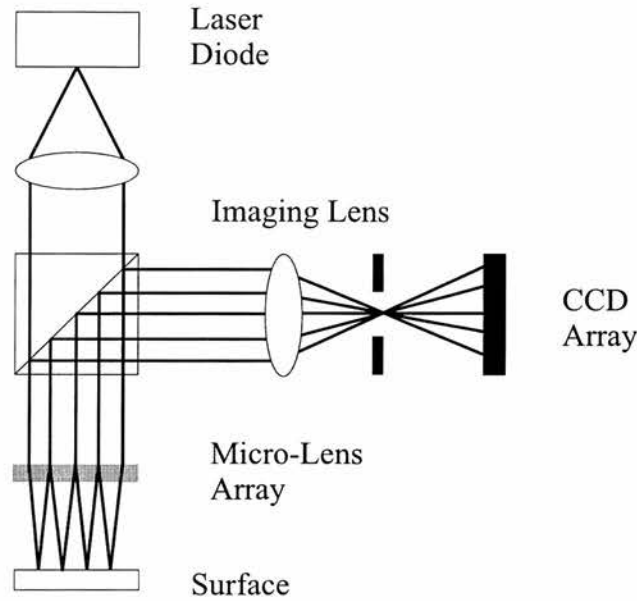


Figure 1.6: A micro-lens based confocal microscope which only requires scanning in the z -direction.

- each line across the sample must be done separately. Also the arm which the stylus is mounted on must be weighted properly - too little weight and the arm will 'bounce' along the surface giving erroneous results, too much weight and the stylus will dig into the sample destroying the sample and also giving erroneous results.

Despite their problems stylus profilers still find much use since they have a much better depth resolution than laser profilers. The DekTak series V system made by Veeco[7] has a depth resolution of $1nm$, whereas the best optical profiler sold by UBM has a depth resolution of $60nm$.

1.2 Interferometers

Interferometry is widely used for profilometry since it offers a non-contact, high-speed highly accurate method for determining the shape of a surface[8].

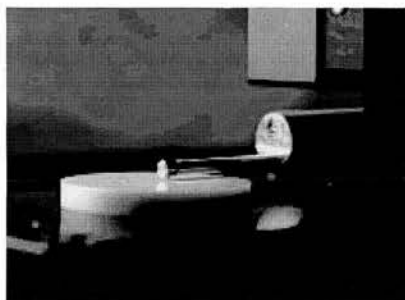


Figure 1.7: A diamond stylus profiling a wafer.

However there are two decision to make - what design of interferometer is to be used and what method is going to be used to determine the profile. The design of interferometer used depends on the situation in which the profilometer will be used - *i.e.* what level of accuracy is needed, how stable the interferometer must be and also cost.

This section examines three types of interferometer commonly used for profilometry. All of them are described in terms of microscope objectives, as most commercial interferometers use microscope objectives. The designs are compared and contrasted - showing that each is suitable for different situations.

1.2.1 Michelson Interferometer

The Michelson interferometer is the simplest of the three interferometers [8]. As shown in figure 1.8 the interferometer uses only one objective, However due to the beam splitter, the objective needs a relatively long working distance, which limits the magnification and numerical aperture, NA, of the system. Stability is also an issue, since both the references and sample surfaces are a distance from the objective.

Since the same lenses are used for illumination and imaging, spherical

aberration and chromatic aberrations are, to a large extent self correcting[9]. Phase errors are also introduced if the reference surface is not flat relative to the beam splitter [10].

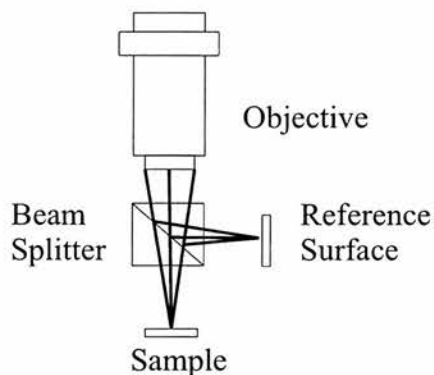


Figure 1.8: A Michelson Interferometer.

1.2.2 Mirau Interferometer

The Mirau interferometer incorporates a small mirror which acts as the reference surface. Two different designs of Mirau interferometer are shown in figure 1.9. Only a single objective is used, and again some optics are placed between the objective and the sample, reducing the working distance. Also the size of the reference surface must be chosen carefully so that at a given magnification it fills the field of view of the objective. This limits the Mirau to medium magnifications, such as 10-40 times [11], and also limits the NA of the system to approximately 0.6 [12]. Care must be taken if used with an objective with a wide field of view, as the beam splitter can be a large source of aberration[9].

However a major advantage of the Mirau is that it affords improved stability when compared to the Michelson. Mirau interferometers are very popular for profilometry and are commonly used, in application such as measuring

surface roughness [13] and surface topography [12].

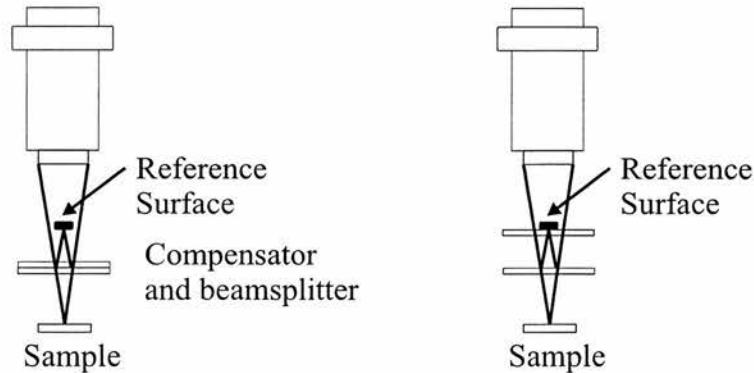


Figure 1.9: Two different Mirau configurations.

1.2.3 Linnik Interferometer

The Linnik interferometer uses two objectives after the beam splitter, as shown in figure 1.10. This means they can have a shorter working distance, and hence a higher NA. Thus Linnik interferometers can be used at much higher magnifications (100 - 200 times). Since the NA determines the overall lateral optical resolution of the system, Linnik interferometers perform much better than the Michelson and Mirau interferometers in this respect. However since two separate objectives are used the Linnik interferometer is much less stable than the Mirau, and has the added cost of two objectives, but with accurate calibration gives the most accurate results[14].

1.2.4 Common path interferometers

In the interferometers described above the beams from the reference and test surfaces follow widely separate paths, making the system sensitive to vibration, and unsuitable for use in industrial environments. However there exists

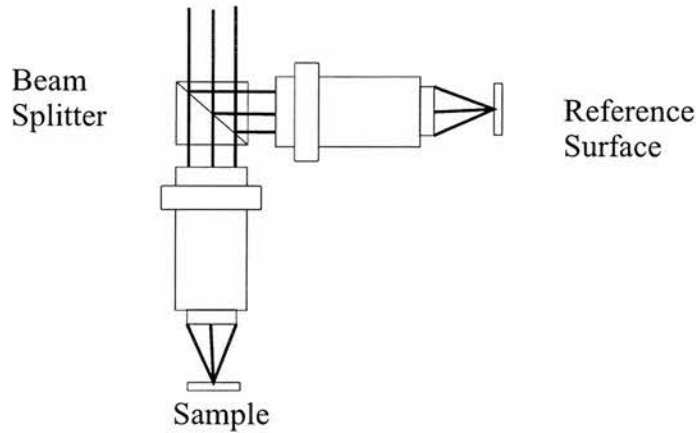


Figure 1.10: A Linnik interferometer.

a class of interferometers where the test and reference beams follow almost the same path, called common path interferometers [15]. These interferometers are inherently stable and find use in wide variety of situations[16].

Lateral Shearing Interferometer

Lateral shearing interferometry is the generation of a interferogram by interfering a beam with a sheared, *i.e.* shifted sideways, copy of itself. There are many different ways to produce sheared beams [17], but one of the most common method is to use a Wollaston prism, which is made out of a birefringent material[18].

A Wollaston prism is shown splitting a beam in figure 1.11. The optic axes of the birefringent material are parallel to the external faces and mutually perpendicular.

A Wollaston prism is a polarisation beam splitter and the two beams that emerge from the Wollaston prism are orthogonally polarised, separated by the angle α , which is given by

$$\alpha = 2(n_e - n_o)\tan(\theta) \tag{1.3}$$

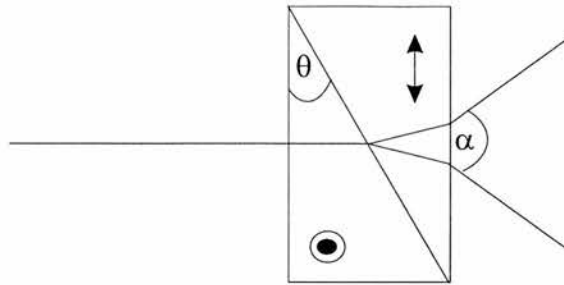


Figure 1.11: A Wollaston prism splitting a beam.

where n_e and n_o are the refractive indices of the material and θ is the angle in the prism. It must be noted that for small angles of incidence α is independent of the angle, but for large angles of incidence and more complete description is required to calculate α [17].

Shearing interferometry is used for surface profilometry since two different regions of the sample can be compared. When combined with a lens as shown in figure 1.12, the Wollaston prism and lens can be used in interferometry.

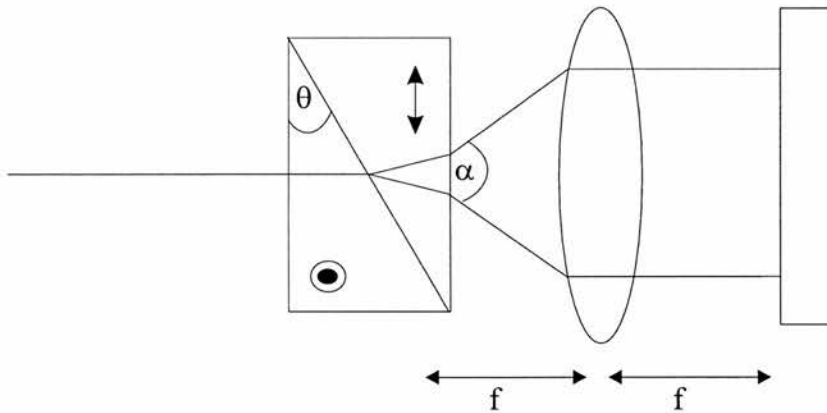


Figure 1.12: A Wollaston prism with a lens to form a shearing interferometer.

Another advantage of the Wollaston prism is that a path difference in between the two beams can be introduced by translating the Wollaston prism at 90° to optical axis of the system. It is possible to find a point on a

Wollaston prism (usually the center) which if a beam strikes, the resultant beams will emerge with identical phase, but if the beam strikes the Wollaston a distance x away from the center of the prism, as shown in figure 1.13. then a path difference is introduced. This path difference, δ , is given by

$$\delta = 2x(n_e - n_o)\tan(\theta) = \alpha.x \quad (1.4)$$

where n_e and n_o are the refractive indices of the material and x is the distance from the center of the Wollaston.

This can be useful to bias the interferometer and finds use in phase shifting interferometers (described below).

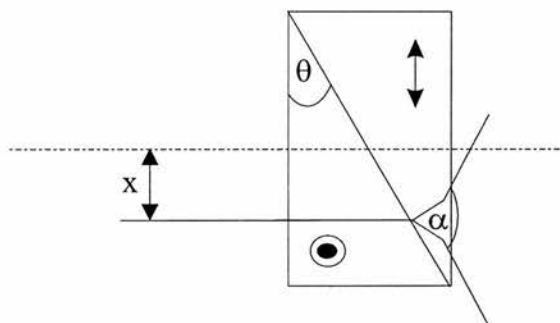


Figure 1.13: A Wollaston prism being used to introduce a phase difference between orthogonal components.

Nomarski Interferometer

When a very small shear distance is used the resulting interferograms gives a measure of slope of the sample, rather than an absolute measure of the height. Thus the resulting image shows the overall surface change. This can be useful to gain qualitative rather than quantitative information about a surface.

A Nomarski microscope objective creates a very small shear between two images. For example the left picture in figure 1.14 shows a white light image of a micro-chip mid-fabrication taken with a normal microscope objective, and the image on the right shows the same micro-chip viewed with a Nomarski objective. Clearly the image on the right shows the surface roughness, but gives no indication of whether the surface defects are pits or asperities. However since no image processing is needed to extract the information from the image, this is a very powerful tool to assess surface roughness.

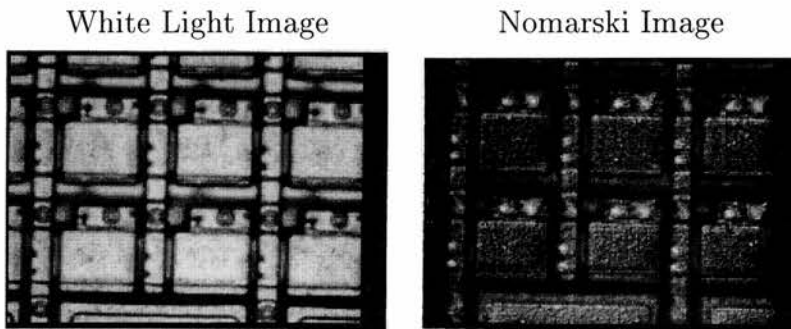


Figure 1.14: Pictures of a micro-chip when viewed with an ordinary and Nomarski microscope objectives.

Recently a system was built that allowed simple visual inspection as seen above, and also used the phase difference between the two different polarizations to obtain qualitative data about the test surface[19]. This system operates with picometric accuracy, but requires complicated electronics.

Analysis of sheared interferograms

Shearing interferometers are widely used in surface profilometry[16, 20] due to their inherent robustness and ease of use. However shearing interferometry is essentially a differential technique and the results can be ambiguous without a proper reference (*i.e.* flat) on the surface under examination.

The sheared interferogram represents the difference between two identical wavefronts, one shifted sideways relative to the other. It is possible to determine the shape of the original wavefront using a least squares algorithm [21, 22, 23]. However in order to do this it is necessary to perform two shears in orthogonal directions. The two resulting interferograms can then be analysed and the shape of the original wavefront recovered. This means that stable interferometers can be built and then the results analysed. However the calculations involved are relatively computationally intensive and require dedicated DSP to be done real-time.

Other methods using Fourier transforms [24] and Zernike polynomials [25] have been proposed since they offer better results than the least squares approach, but are corresponding more complex.

1.3 Interferometric Techniques

Once a specific design of interferometer has been chosen it is also necessary to select an algorithm to extract data from the interferogram. What follows is a brief synopsis of the main interferometric techniques used for surface profilometry.

1.3.1 Phase Stepping

Phase shifting interferometry is a widely used technique, finding use in testing of high optical quality systems[26] and profilometry[27, 28]. The basic idea behind phase shifting interferometry is to change the phase of the reference beam in a controlled way and hence change the interferogram that is generated. By taking several different interferograms with different phase changes for the reference beam it is possible to determine the wavefront of

the sample beam.

There are many different phase stepping techniques [29, 30, 31], but the most commonly used method is the *Four step method*. If the phase of the reference beam is shifted by $0, \frac{1}{2}\pi, \pi$ and $\frac{3}{4}\pi$ and the resultant interferograms called I_1, I_2, I_3 and I_4 , then for a given point the phase ϕ is given by [32]

$$\phi = \tan^{-1}\left(\frac{I_4 - I_2}{I_1 - I_3}\right) \quad (1.5)$$

However this method gives phase discontinuities every 2π , which must be smoothed out using appropriate algorithms. Figure 1.15 shows a wavefront determined this way with the phase discontinuities that arise and also the same wavefront with the discontinuities removed.

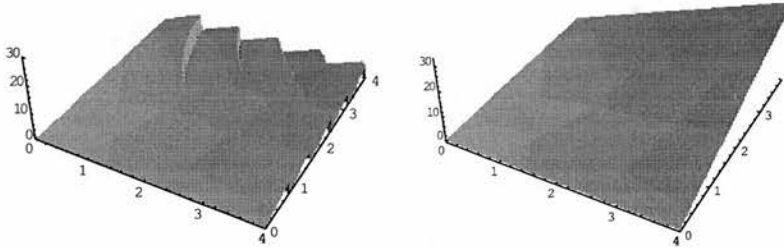


Figure 1.15: Images showing image with phase discontinuities and resulting image when phase discontinuities have been removed.

1.3.2 White Light

A white light, or a wide bandwidth source, is characterised as having a short coherence length. Due to the short coherence length of the source, fringes only occur near zero path difference between the sample and reference beams[33, 34]. To obtain a 3D-profile of a surface, the reference mirror in the interferometer is scanned and for each position of the mirror the points of

maximum fringe contrast map a particular height contour of the surface[35]. This technique has been extended such that the position of maximum fringe contrast can be inferred from eight independent intensity measurements [36]. In both cases the time needed to scan the reference mirror is a significant limitation when analysing moving surfaces.

White light interferometry can also be used in conjunction with spectroscopic techniques to determine the profile of the surface in real time[37]. The interferogram that arises from interference of white light can be thought of as a incoherent superposition of a range of colours. By analysing the resultant interferogram spectroscopically is it possible to determine the wavenumber, which varies linearly with path difference between the two orthogonally polarised beams[38]. However in order for this technique to work, the white light pulses must overlap and this limits this technique to surface with surface variation with less then the coherence length of white light, unless it is used in conjunction with scanning.

1.3.3 Multiple Wavelength

Another technique is to use multiple wavelengths to record a number of interferograms with different wavelengths to overcome any ambiguity[39]. The subsequent analysis to determine the profile is quite complex[40] but the technique is widely used to analyse aspheric surfaces[41].

1.3.4 Limitations of interferometric Techniques

Interferometric techniques are very powerful but they are not without problems. The complex refractive index of metals leads to a phase change which can be a significant source of error for sub-wavelength profilometry[42]. At $\lambda = 650nm$ the phase changes at normal incidence are 0.4° for silicon, 15° for

aluminium and 30° for gold, which corresponds to path length differences of 0.4, 14 and $27nm$. For a surface made of unknown metals this can give rise to incorrect surface profiles. Even when the metal type is known for evaporated metals the properties of the metal depend on evaporating conditions. However by use of optical micro-ellipsometer it is possible to measure both the optical phase change and material properties[43].

1.4 Summary

This chapter has reviewed common techniques used for profilometry and loosely divided them into two categories: non-interferometric and interferometric techniques. Typical non-interferometric techniques include using a stylus or time-of-flight methods to determine profiles. This chapter paid particular attention to interferometric techniques, such as phase stepping and white light interferometry. The next chapter describes a novel interferometric technique developed at St Andrews University which overcomes some of the problems associated with interferometric techniques, such as fringe ambiguity.

Chapter 2

Surface profilometry based on polarisation analysis

In this chapter a novel technique for analysing interferometric images is proposed and its viability within a shearing interferometer is demonstrated. A filtered white-light source with a coherence length comparable to the range in surface heights on the sample was used. Rather than scanning the reference mirror to determine the maximum fringe contrast, the reduction in fringe contrast is measured to determine the deviation from zero path difference. This work won the *NPL Award for World Class Metrology*.

The fringe contrast depends both on the relative height and reflectivity of the reference and sample surfaces. For profilometry, this dependence on reflectivity presents a significant challenge. We have identified that measuring the modulus of the complex degree of coherence, which is defined in terms of the Stokes polarisation parameters, gives a measure of the path difference independent of the reflectivity of the surfaces. As shown in figure 2.1 for two orthogonally polarised pulses the resultant polarisation depends on the

amount of overlap.

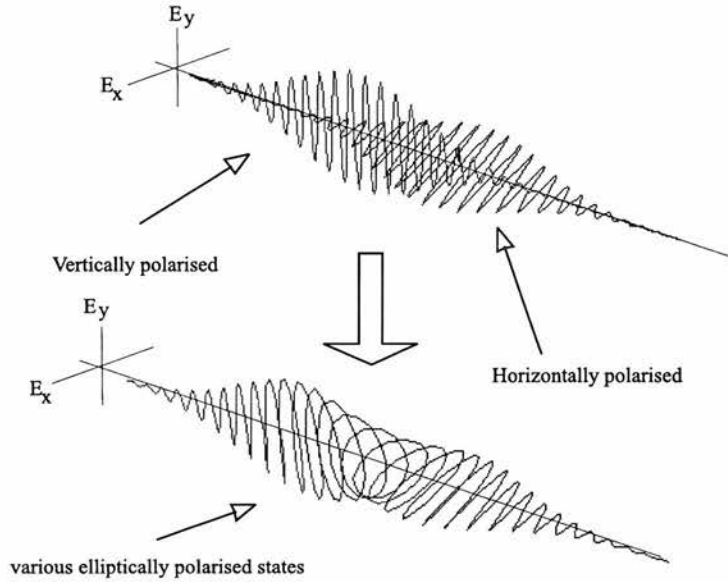


Figure 2.1: Electric field of two orthogonally polarised pulses overlapping and their resultant polarisation.

When using an interferometer for which the sample and reference beams are orthogonally polarised, the complex degree of coherence can be defined by four intensity measurements. We believe that both the use of reduced fringe contrast as a means of determining relative height and the measurement of polarisation state to eliminate the dependence on surface reflectivity, clearly distinguishes our approach from other phase stepping and white-light techniques. Our technique will allow an entire profile to be obtained using a single pulse of illumination and four detectors. This is essential for the analysis of moving surfaces with which traditional scanning techniques cannot cope. Beams with polarisation states which vary across their aperture have been discussed elsewhere[44] but not hitherto with respect to their use within interferometry.

2.1 Mathematical Analysis

Consider two pulses of quasi-monochromatic light propagating in a Michelson interferometer shown in figure 2.2.

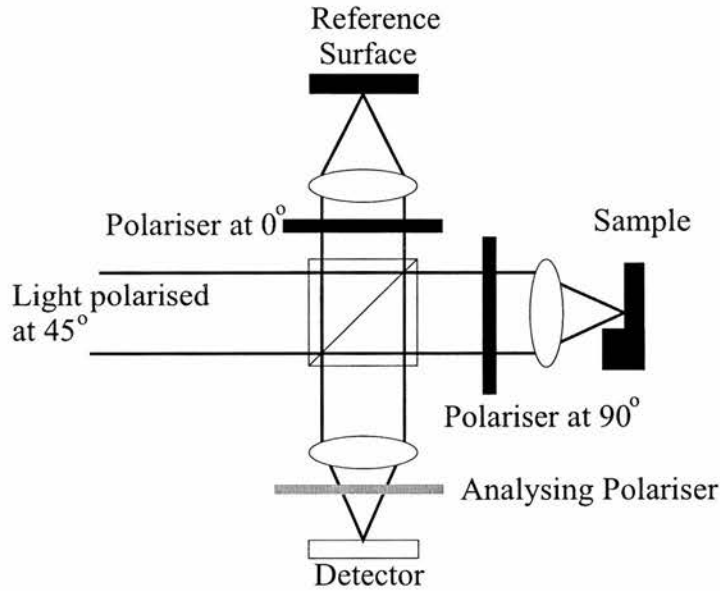


Figure 2.2: A Michelson interferometer

The two arms of the interferometer have a perfect mirror and a sample of varying reflectivity and height. The light is linearly polarized at 45° to the x -axis and is resolved into orthogonal components by the polarising beam-splitter. The orthogonal components travel down separate arms of the interferometer and are represented by

$$E_x(t) = A(t)e^{-i\omega t} \quad (2.1)$$

and

$$E_y(t) = \rho.A(t)e^{-i\omega t} \quad (2.2)$$

where $A(t)$ is the envelope function, and ω is the angular frequency. E_y

is delayed relative to E_x and also is reduced in amplitude by a factor of ρ where ρ is directly related to the reflectivity of the sample.

When the beams are co-linear after returning through the beam splitter the \mathbf{E} field is described by

$$\mathbf{E}_{\text{vector}}(t) = \mathbf{i}E_x(t) + \mathbf{j}E_y(t - \frac{2d}{c}) \quad (2.3)$$

where d is the path length difference between two two arms in the interferometer. Hence

$$\mathbf{E}_{\text{vector}}(t) = \mathbf{i}A(t)e^{-i\omega t} + \mathbf{j}\rho.A(t - \frac{2d}{c})e^{-i\omega t - i\omega\frac{2d}{c}} \quad (2.4)$$

After passage through a linear polarizer with its axis at an angle θ to the x-axis,

$$E(t) = \mathbf{E}_{\text{vector}}(t) \cdot \{\mathbf{i}\text{Cos}(\theta) + \mathbf{j}\text{Sin}(\theta)\} \quad (2.5)$$

and the short-time average transmitted intensity is given by

$$\begin{aligned} E(t)E^*(t) &= |A(t)|^2\text{Cos}^2(\theta) + \rho^2|A(t - \frac{2d}{c})|^2\text{Sin}^2(\theta) \\ &+ 2\rho A(t)A(t - \frac{2d}{c})\text{Cos}(\theta)\text{Sin}(\theta)\text{Sin}(\omega\frac{2d}{c}) \end{aligned} \quad (2.6)$$

The long-time averaged intensity detected at the CCD is given by the integral

$$I(\theta) = \int_{-\infty}^{\infty} E(t)E^*(t)dt \quad (2.7)$$

which on substitution of equation 2.6 yields the equation

$$\begin{aligned} I(\theta) &= I_a\text{Cos}^2(\theta) + \rho^2 I_a\text{Sin}^2(\theta) + \\ &2\rho I_{\otimes}(d)\text{Cos}(\theta)\text{Sin}(\theta)\text{Cos}(\omega\frac{2d}{c}) \end{aligned} \quad (2.8)$$

where

$$I_a = \int_{-\infty}^{\infty} |A(t)|^2 dt = \int_{-\infty}^{\infty} |A(t - \frac{2d}{c})|^2 dt \quad (2.9)$$

and

$$I_{\otimes}(d) = \int_{-\infty}^{\infty} A(t)A(t - \frac{2d}{c})dt \quad (2.10)$$

2.1.1 Stokes parameters

To describe the polarisation of the light normalised Stokes parameters are used[45]. Although Stokes parameters were first described in 1852 they are not well known, but have found use in such diverse situations as inspecting LCDs[46] and two photon decay of hydrogen[47]. Here normalised Stokes parameters are used, which are 3 dimensionless quantities that describe the polarisation, but not intensity or spectrum of the light[48]. Each of the parameters describes a time-averaged value rather than a instantaneous measurement, ranging between -1 and 1 . The three Stokes parameters p_1, p_2 and p_3 describe a vector that exists not in real space but in Poincaré space[48]. They can be derived via considerations of the electromagnetic field but they are easier to understand when defined operationally. They are expressed as,

$$p_1 = \frac{I_0 - I_{90}}{I_0 + I_{90}}, \quad (2.11)$$

$$p_2 = \frac{I_{45} - I_{-45}}{I_{45} + I_{-45}} \quad (2.12)$$

and

$$p_3 = \frac{I_{Right} - I_{Left}}{I_{Right} + I_{Left}} \quad (2.13)$$

where $I_0, I_{90}, I_{45}, I_{-45}, I_{Right}$ and I_{Left} are the measured intensities of the polarisation state.

Hence, in principle six measurements are required to deduce the three Stokes parameters. These parameters lend themselves to the definition of the degree of polarisation, which varies between 1 for fully polarised light and 0 for unpolarised light.

$$P = \sqrt{p_1^2 + p_2^2 + p_3^2} \quad (2.14)$$

In the case described above where there are two overlapping orthogonally-polarised beams interfering, it must be recognised that the degree of polarisation P depends on the relative intensity of the beams. However, we have identified another parameter, $|\mu_{xy}|$, which also ranges between 0 and 1 but is independent of the relative intensities of the beams. $|\mu_{xy}|$, the modulus of the complex degree of coherence[48] is given by

$$|\mu_{xy}| = \sqrt{\frac{p_2^2 + p_3^2}{1 - p_1^2}} \quad (2.15)$$

For the Michelson interferometer described above the linear polarisation Stokes parameters p_1 and p_2 are given by

$$p_1 = \frac{I_0 - I_{90}}{I_0 + I_{90}} = \frac{1 - \rho^2}{1 + \rho^2} \quad (2.16)$$

and

$$p_2 = \frac{I_{45} - I_{135}}{I_{45} + I_{135}} = \left(\frac{2\rho}{1 + \rho^2} \right) \left(\frac{I_{\otimes}(d)}{I_a} \right) \text{Cos}\left(\omega \frac{2d}{c}\right) \quad (2.17)$$

As can be seen p_1 depends only on ρ , and thus the reflectivity of the sample and does not vary with path length difference d . p_2 also depends on ρ but varies with d .

Determination of p_3

Circularly polarised light must be detected by use of a quarter wave plate and polariser. Right-handed circularly polarized light and left-handed circularly polarized light may be analysed by setting the angle θ of the linear polarizer at $+45^\circ$ and -45° relative to the principle axis after the quarter wave plate. On emerging from the quarter-wave plate,

$$\mathbf{E}_{\text{vector}}(t) = \mathbf{i}A(t)e^{-i\omega t} + \mathbf{j}\rho.A\left(t - \frac{2d}{c}\right)e^{-i\omega t - i\omega \frac{2d}{c} - \frac{\pi}{2}} \quad (2.18)$$

which after a similar argument for the determination of p_1 and p_2 it can be shown that p_3 is given by,

$$p_3 = \frac{I_{Left} - I_{Right}}{I_{Left} + I_{Right}} = - \left(\frac{2\rho}{1 + \rho^2} \right) \left(\frac{I_{\otimes}(d)}{I_a} \right) \text{Sin}\left(\omega \frac{2d}{c}\right) \quad (2.19)$$

p_3 also depends of ρ and is seen to vary sinusoidally with path length difference d , and in quadrature with p_2 .

2.1.2 The degree of polarisation

Hence in terms of the above integrals the degree of polarization P is given by

$$P = \sqrt{p_1^2 + p_2^2 + p_3^2} = \sqrt{\left(\frac{2\rho}{1 + \rho^2} \right) \left(\frac{I_{\otimes}(d)}{I_a} \right)^2 + \left(\frac{\rho^2 - 1}{\rho^2 + 1} \right)^2} \quad (2.20)$$

The degree of polarisation varies both with the path length difference d and also the reflectivity of the sample ρ . If the reflectivity of the sample is uniform and known then this can be accounted for. However for a sample with an unknown and non-uniform reflectivity measuring P will result in ambiguous results.

2.1.3 Degree of Coherence

The modulus of the complex degree of coherence $|\mu_{xy}|$ is given by,

$$|\mu_{xy}| = \sqrt{\frac{p_2^2 + p_3^2}{1 - p_1^2}} = \frac{I_{\otimes}(d)}{I_a} \quad (2.21)$$

$|\mu_{xy}|$ varies with path length difference d but is independent of ρ . Very significantly this means that it can be used to correctly determine the path length difference for a sample with a varying, non-uniform and unknown reflectivity.

We measure $|\mu_{xy}|$ for each pixel element in the image, thereby providing a practical means of determining the profile of the whole surface. Also since the sum of orthogonal components is equal, *i.e.* $I_0 + I_{90} = I_{45} + I_{-45} = I_{Right} + I_{Left}$, the requirement for six measurements per pixel is reduced to four. For example if I_0 , I_{90} , I_{45} and I_{Right} are measured then the remaining Stokes parameters are given by

$$I_{-45} = (I_0 + I_{90}) - I_{45} \quad (2.22)$$

and

$$I_{Left} = (I_0 + I_{90}) - I_{Right} \quad (2.23)$$

2.2 Experimental setup

To demonstrate the use of this algorithm we assembled a shearing interferometer based on a Wollaston prism. Similar designs of interferometer have been reported earlier for use in demanding environments[49] or applications where relative height differences are more important than absolute measurement[50]. The Wollaston prism acts as polarisation beam splitter introducing a deviation angle of a few degrees between the two orthogonal polarisations. Placing the prism in the back focal plane of the objective lens, which images the surface, produces two parallel beams which strike adjacent regions of the sample surface, separated by approximately $1mm$. This can be compared to a Nomarski microscope where the beam separation is typically only a few microns[19, 51]. After reflection from the sample the beams are recombined by the Wollaston prism and are analysed subsequently using the appropriately oriented polarisers and wave plate. If the surface gives rise to a change in polarisation of the beam this is not a problem because the Wollaston prism correctly repolarises the two beams and as discussed above,



Figure 2.4: Photograph of working interferometer

by the two sheared beams overlap. The profiles obtained correspond to the difference in the sample surface height between two points separated by the shear distance. For flat samples containing isolated features smaller than the shear distance then this differential measurement gives the absolute height of the feature above the surrounding background.

The height measurement range is controlled by changing the coherence length of the light source. For a laser system this requires a control of the pulse duration but for a white-light source a selection of interference filters with various bandwidths is sufficient. The $|\mu_{xy}|$ data can be used directly to

infer height or used within a standard fringe analysis software as a means of identifying the fringe number.

For the sake of simplicity, within our interferometer, the four images corresponding to I_0 , I_{90} , I_{45} and I_{Right} are acquired sequentially with the appropriate polariser and wave plate inserted prior to the detector array. The light source is a tungsten halogen bulb combined with $10nm$ wide interference filter centered at $633nm$. The corresponding coherence length of $38\mu m$, allowing for the doubling of path difference associated with the reflection from the object surface, gives an unambiguous measurement range of $19\mu m$ (approximately 30 optical wavelengths).

2.3 Results

The exact relationship between $|\mu_{xy}|$ and the height of the sample depends on the envelope of the wave packet which itself is the Fourier-transform of the spectral filter envelope. A mathematical relationship can be derived but in practice it is better to calibrate the observed values of $|\mu_{xy}|$ against a reference surface with a linear height variation. For a Gaussian spectrum the relationship between $|\mu_{xy}|$ and pulse overlap d is shown in figure 2.5.

The accuracy of the surface height measurement depends directly on the accuracy to which $|\mu_{xy}|$ is known. This in turn is limited by the precision to which the various intensity states are measured. For an imaging system based on CCD's, 8-bit digitisation of the recorded intensity levels is standard practice. A simple numerical model of the calculated value of $|\mu_{xy}|$ for given measured intensities shows that this limits the precision of inferred height measurements to approximately 1% of the coherence length.

A processed silicon wafer was analysed within the interferometer. The

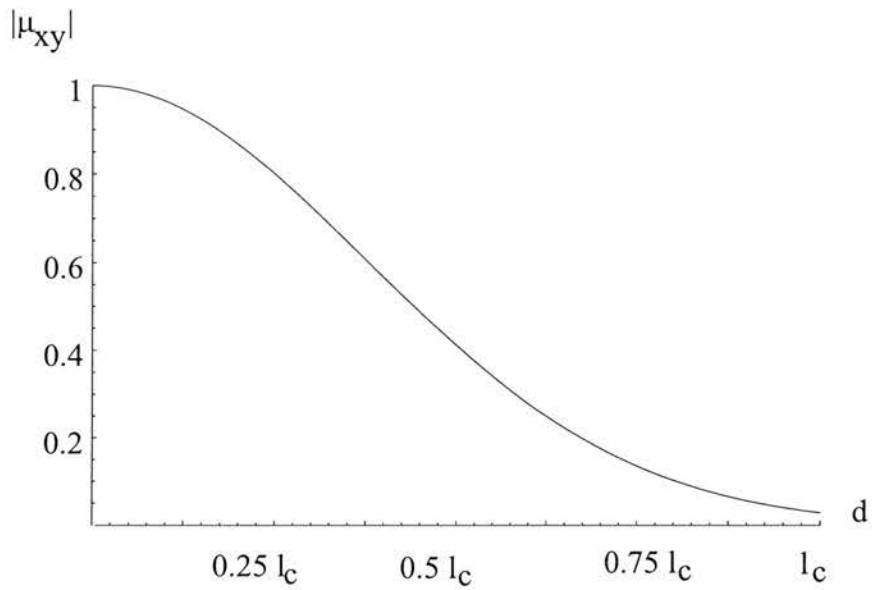


Figure 2.5: Graph showing relationship between $|\mu_{xy}|$ and pulse overlap d for a Gaussian spectrum

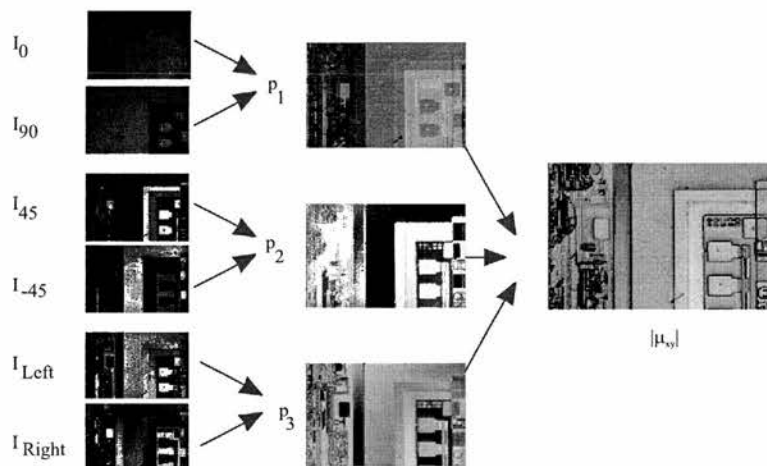


Figure 2.6: Diagram showing steps to generate $|\mu_{xy}|$. Note all six polarisation measurements are shown for simplicity, where only four are actually measured.

wafer represents a challenging object for traditional interferometers because

the various layers are separated by step changes in height of many optical wavelengths. The steps to generate the profile are shown in figure 2.6. Figure 2.7 shows a regions of the silicon wafer profiled using the shearing interferometer and polarisation algorithm. The region lies near the edge of the wafer thereby allowing comparison of a structure region with a flat reference area. 3D profiles of regions of the wafer are shown in figures 2.8 and 2.9. The results show that the algorithm works extremely well, giving unambiguous height information associated with each pixel in the image. The observed height measurement accuracy is approximately $200nm$. As discussed above, this figure could be improved by using standard fringe analysis software to give sub-wavelength precision, our algorithm can be used to identify the fringe number.

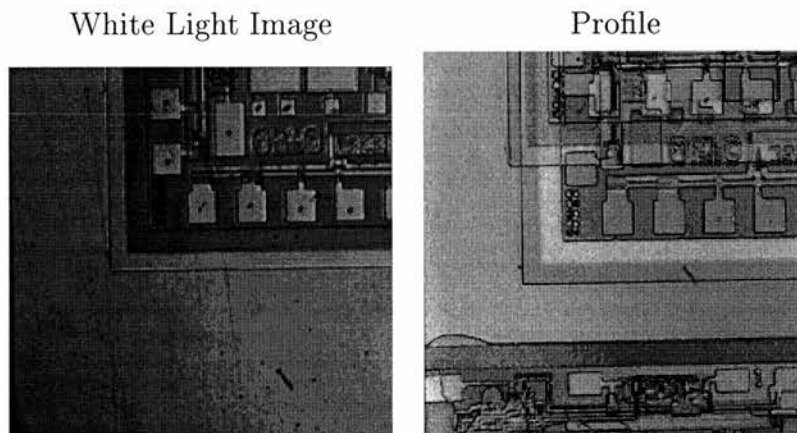


Figure 2.7: Figure showing white light image and $|\mu_{xy}|$ data.

2.4 Quantative results

In order to assess the accuracy of the technique the silicon wafer was scanned in an AFM and the AFM results were compared to those obtained by cal-

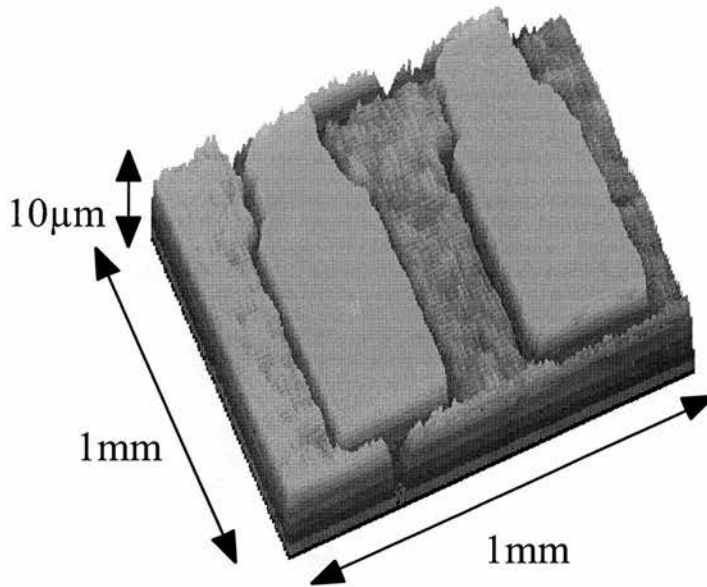


Figure 2.8: 3D profile of wafer generated from $|\mu_{xy}|$ data.

culating $|\mu_{xy}|$. Figure 2.10 shows a lateral scan across the wafer using the AFM, and figure 2.11 shows a profile of the same region of the silicon wafer using the $|\mu_{xy}|$ technique. The relative height differences obtained by AFM and calculating $|\mu_{xy}|$ are shown in table 2.1.

AFM result	$ \mu_{xy} $ Result
$2.7\mu\text{m}$	$2.55\mu\text{m}$
$1.85\mu\text{m}$	$2\mu\text{m}$

Table 2.1: Comparison of AFM profiling to $|\mu_{xy}|$ profiling

By comparing the results in the table it can be seen that the $|\mu_{xy}|$ method gives results which have sub-wavelength accuracy, being accurate to about 200nm . The accuracy of the system is limited by the accuracy with which the polarisation can be correctly determined. Also the system only needs to be accurate to a wavelength since standard interferometric analysis techniques can be used to determine the sub wavelength structure.

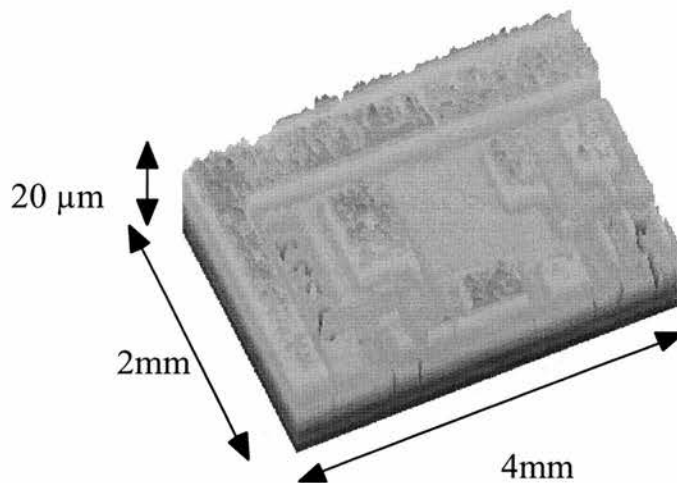


Figure 2.9: 3D profile of wafer generated from $|\mu_{xy}|$ data.

2.5 Conclusions

We emphasise that this polarisation measurement algorithm can be applied to any interferometric measurement system in which the two beams are orthogonally polarised and the light source has a finite coherence length. For example, a polarising Michelson interferometer configured using a reference flat would allow unambiguous surface profiles of any sample to be obtained. From four intensity measurements the algorithm eliminates any ambiguity associated with fringe counting and consequently offers a major advance over other phase stepping and white-light techniques. The measurement accuracy of our technique is sufficient for many applications but the algorithm could also be used to identify fringe number within a conventional phase stepping algorithm giving improved accuracy. The use of a single illumination pulse and four cameras would allow the technique to be applied to situations where the surface characteristics are changing dynamically. This chapter is based a paper published in *Optics Letters* by JP Lesso, AJ Duncan, W Sibbett and MJ Padgett, Vol. 23, No. 23, 1998.

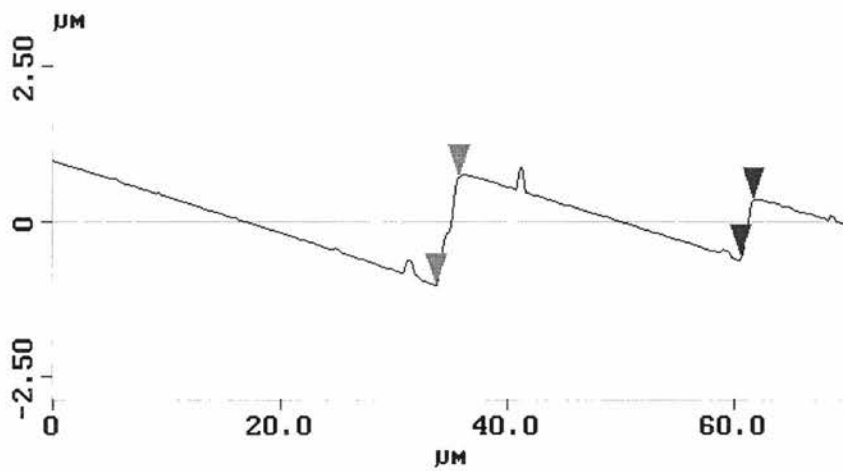


Figure 2.10: AFM scan of Silicon wafer

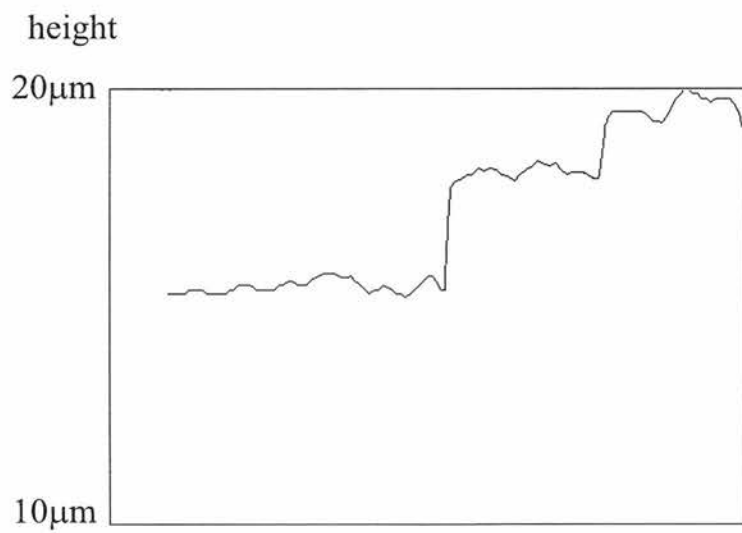


Figure 2.11: Profile of silicon wafer determined by $|\mu_{xy}|$.

Chapter 3

Further Analysis of $|\mu_{xy}|$

In order to better understand the previous experimental results and to allow us to make better predictions about the system described in the previous chapter, $|\mu_{xy}|$ was further analysed mathematically, both analytically and numerically.

3.1 Numerical modeling

A model was developed in *Mathematica 3.0* to examine the properties of the system. The code is attached in Appendix B. The program modelled two orthogonally polarised pulses propagating in a Michelson interferometer. Two pulses were propagated and the path length difference d was linearly varied over the coherence length of the light l_c . The modeling was based upon two orthogonally polarised Gaussian pulses with a variable overlap. Using the notation of the previous chapter the envelope function describing the electric field of the pulses is

$$A(t) = \exp\left(\frac{t - l_c/2}{l_c/4}\right)^2 \quad (3.1)$$

where l_c is the coherence length of the light.

The linear polarisation components can then be evaluated using equation 2.7. Simply by numerical integrating over the time interval from zero to the coherence length the intensity can be found. This allows the calculation of I_0 , I_{90} , I_{45} and I_{-45} . The circular polarisation states I_{Right} and I_{Left} were determined by delaying the phase of one of the pulses a by an additional $\lambda/4$.

3.1.1 Numerical modelling results

p_1

Since I_0 and I_{90} are the pulses that return from the reference and sample respectively, p_1 gives a measure of their amplitude difference. For the case when the mirror is perfectly reflecting p_1 is essentially a measure of reflectivity of the surface and as predicted by equation 2.16 p_1 does not vary with d . In the case when a perfect mirror is used for the reference, by comparing the difference in intensity of the reflected pulses via p_1 , the reflectivity of the sample can be found. Note for a perfectly reflecting sample it is not necessary to determine p_1 , since I_0 and I_{90} are equal.

In this example the pulses were of a different amplitude hence p_1 is non zero. Figure 3.1 shows how p_1 varies with d .

p_2

p_2 is a measure of the linearly polarised light at 45° to the reference axes present in the pulses. Figure 3.2 shows how the visibility of the fringes decreases as the path length difference changes from 0 to l_c . p_2 varies sinusoidally with d as predicted by equation 2.17.

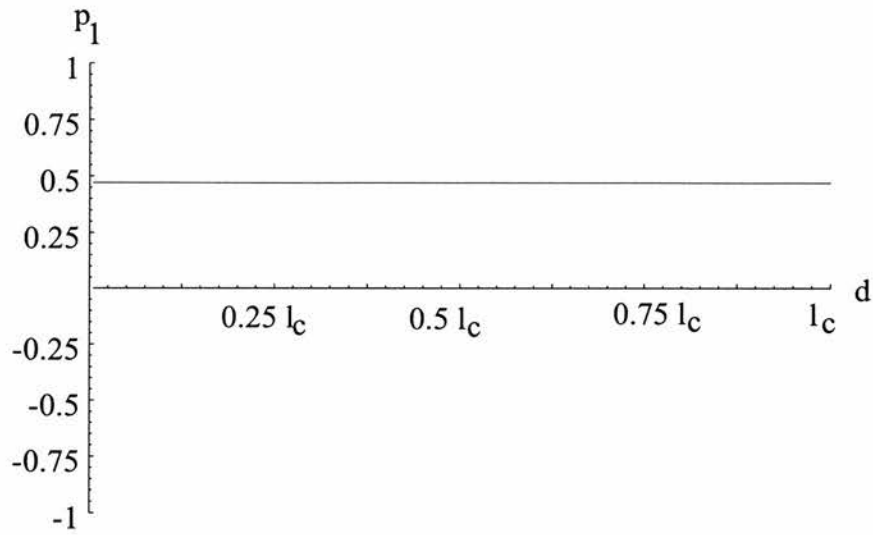


Figure 3.1: Graph showing how p_1 varies with pulse overlap for a sample with $\rho = 0.6$.

p_3

p_3 is a measure of the circularly polarised light in the pulse. It can be seen that p_2 and p_3 vary sinusoidally and in quadrature to each other as predicted by equations 2.17 and 2.19.

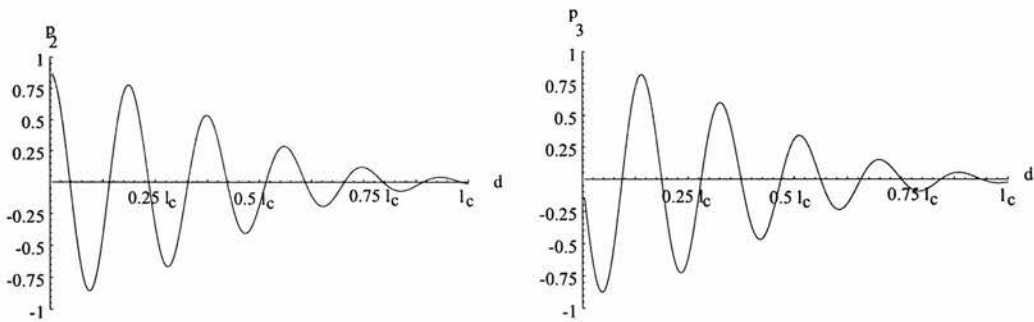


Figure 3.2: Graphs showing how p_2 and p_3 varies with pulse overlap

P and $|\mu_{xy}|$

Figure 3.3 shows how P and $|\mu_{xy}|$ vary with d . As can be seen due to the difference in the amplitudes of the two pulses P has a limited range of usefulness. However for all values of overlap $|\mu_{xy}|$ has a unique value. The minimum value P reaches is p_1 , which is to say the greater the difference in the amplitude of the orthogonally polarised pulses the smaller the range over which P gives the correct answer.

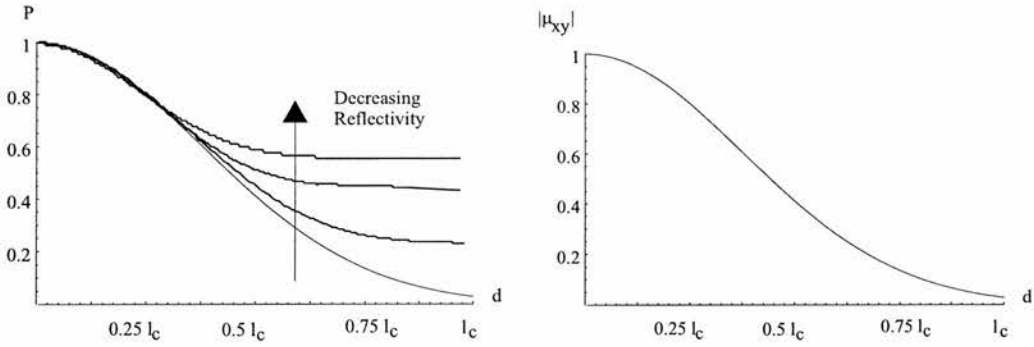


Figure 3.3: Graphs showing how P and $|\mu_{xy}|$ vary with pulse overlap

In the case that the mirror and sample have the same reflectivity p_1 is zero then $|\mu_{xy}|$ and P are equal

$$|\mu_{xy}| = P = \sqrt{p_2^2 + p_3^2} \quad (3.2)$$

Note also that it is always possible to find a set of axes in which $|\mu_{xy}|$ and P are equal.

3.2 Polariser mis-alignment

The above simulations were repeated with the analysing polariser consistently mis-aligned for each measurement. The mis-alignment results in perturbations in p_1 and also p_2 and p_3 do not vary about zero. Two $|\mu_{xy}|$ vs. d

curves for different polariser mis-alignments with a light source with $l_c = 8\lambda$ are shown in figure 3.4. As can be seen from the figure the polariser mis-alignment results in perturbations in the curve and also the shape of the curve is deformed. Increasing the polariser mis-alignment to 5° results in a severely deformed curve. Hence it is very important to accurately align the polariser for the polarisation measurements.

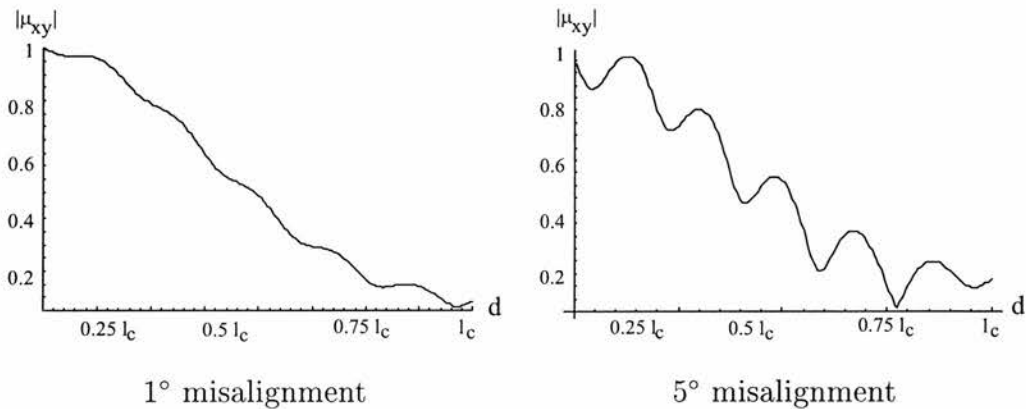


Figure 3.4: $|\mu_{xy}|$ vs. d curves with polariser mis-alignment

3.3 Wave plate errors

A common source of error due to using wave plates is to use a wave plate optimised for the wrong wavelength. In order to understand how to correct for such errors the concept of a Poincaré Sphere must be introduced.

3.3.1 Poincaré Sphere

The 3 Stokes parameters define a point in or on the Poincaré Sphere, as shown in figure 3.5. The 3 parameters are commonly referred to as the Stokes vector[52]. The Poincaré sphere gives a graphical interpretation for P . P is simply the distance from the centre of the sphere[45].

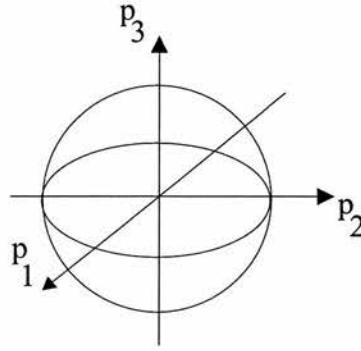


Figure 3.5: Poincaré Sphere

It is possible to determine the resultant Stokes vector for an arbitrary Stokes vector after passing through a wave plate which introduces a delay Δ with its fast axis at an angle γ [45]. The method involves defining two rotation matrices $A(\gamma)$ and $B(\Delta)$ which are defined as

$$A(\gamma) = \begin{pmatrix} \cos(2\gamma) & \sin(2\gamma) & 0 \\ -\sin(2\gamma) & \cos(2\gamma) & 0 \\ 0 & 0 & 1 \end{pmatrix} \quad (3.3)$$

and

$$B(\Delta) = \begin{pmatrix} 1 & 0 & 0 \\ 0 & \cos(-\Delta) & \sin(-\Delta) \\ 0 & -\sin(-\Delta) & \cos(-\Delta) \end{pmatrix} \quad (3.4)$$

Then for an arbitrary Stokes vector $\mathbf{S}_{\text{in}} = (p_1, p_2, p_3)$ passing through a wave plate which introduces a delay Δ with its fast axis at an angle γ the resultant Stokes vector \mathbf{S}_{out} is given by

$$\mathbf{S}_{\text{out}} = \mathbf{S}_{\text{in}} \cdot A(\gamma) \cdot B(\Delta) \cdot A(-\gamma) \quad (3.5)$$

The errors that arise due wave plates can be understood by looking at figure 3.6. If fully circularly polarised light $p_3 = 1$ passes through a correct wave plate $p_2 = 1$ should be obtained. A is the initial point and B is the

ideal final point. If a wave plate of incorrect thickness is used then some intermediate point is achieved, such as point C .

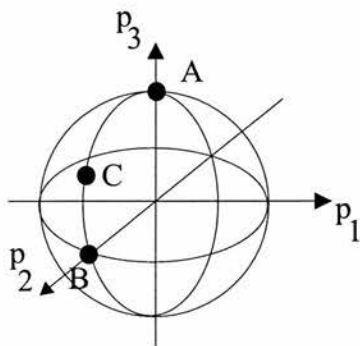


Figure 3.6: Various points on a Poincaré corresponding to use of different wave plates.

3.3.2 Mis-matched wave plate

Figure 3.8 shows a somewhat extreme case where a quarter-wave plate for $\lambda = 444nm$ has been used with a light source with $\lambda = 633nm$. However if the phase-mismatch is known then it is possible to correct for it.

By considering the p_2/p_3 plane from figure 3.6 the set of axes shown in figure 3.7 is obtained.

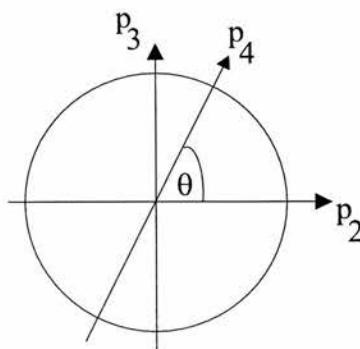


Figure 3.7: p_2/p_3 plane in Poincaré Sphere

If a wave plate with the incorrect phase mis-match is used then the component along axes p_4 is being measured. In terms of p_2 and p_3 this new component is given by

$$p_4 = p_2 \text{Cos}(\theta) + p_3 \text{Sin}(\theta) \quad (3.6)$$

where

$$\theta = \frac{\pi}{2} \cdot \frac{\lambda_{used}}{\lambda} \quad (3.7)$$

where λ_{used} is the wave length that the wave plate used is optimised for and the λ is wavelength of the source. Hence p_3 can be recovered

$$p_3 = \frac{p_4 - p_2 \text{Cos}(\theta)}{\text{Sin}(\theta)} \quad (3.8)$$

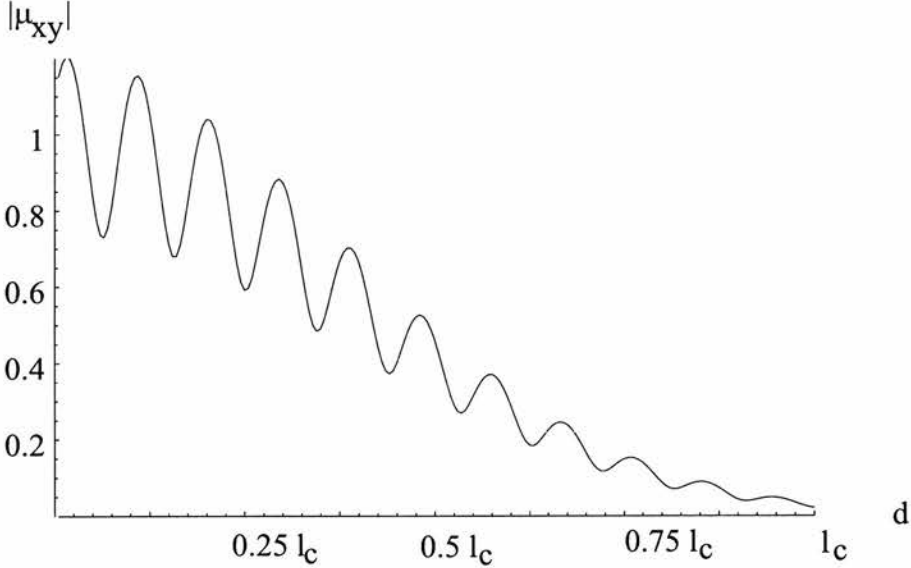


Figure 3.8: Graph showing perturbations arising in the $|\mu_{xy}|$ curve due to wave plate mis-match

By substituting 3.8 into the equation for $|\mu_{xy}|$, the following equation is obtained

$$|\mu_{xy}| = \sqrt{\frac{p_2^2 + p_4^2 + 2p_2p_4 \text{Cos}(\theta)}{(1 - p_1^2)(4\text{Cos}^2(\theta/2)\text{Sin}^2(\theta/2))}} \quad (3.9)$$

3.4 Chromatic and achromatic wave plates

Another problem that can arise from use of birefringent wave plates is to do with the difference between chromatic and achromatic wave plates. An achromatic wave plate is one in which the group velocity of the waves are equal[53]. If the group velocities are not equal then the two pulses emerging from the wave plate will have their envelopes as well as their phases shifted relative to each other. In a birefringent material for the o-ray the group velocity v_{go} is given by[54]

$$v_{go} = \frac{c}{n_e + \omega_0 \left(\frac{\partial n_o}{\partial \omega} \right)} \quad (3.10)$$

and it can be shown (see Appendix C) that for a wave plate of thickness D if

$$\frac{D(n_e - n_o)}{\lambda} = \text{constant} \quad (3.11)$$

then $v_{ge} = v_{go}$, *i.e.* the wave plate is achromatic. For a quarter-wave plate of thickness D , on emerging from the plate the electric field will take the form,

$$\mathbf{E}(t) = \mathbf{i}A\left(t - \frac{D}{v_{ge}}\right)e^{-i\omega t - i\omega \frac{n_e D}{c}} + \mathbf{j}A\left(t - \frac{2d}{c} - \frac{D}{v_{ge}}\right)e^{-i\omega t - i\omega \frac{2d}{c} - i\omega \frac{n_o D}{c}} \quad (3.12)$$

where n_o and n_e are the ordinary and extra-ordinary refractive indices, v_{go} and v_{ge} the ordinary and extra-ordinary group velocities. That is to say the phases of the pulses are shifted by an amount $D\left(\frac{n_o}{c} - \frac{n_e}{c}\right)$ and the envelope function $A(t)$ by an amount $D\left(\frac{1}{v_{ge}} - \frac{1}{v_{go}}\right)$. The relative shift in phase is wanted, but the relative shift in the envelopes is undesirable. For an achromatic wave plate since $v_{ge} = v_{go}$ the envelope functions of the pulses remain stationary relative to each other.

Following a similar analysis from the previous chapter the Stokes parameter for circularly polarised light measured with a chromatic wave plate

$p_{3(chrom)}$ is determined and compared to p_3 . After passage through the linear polarizer with its axis set at an angle θ to the x -axis,

$$E(t) = \mathbf{E}(t) \cdot (\mathbf{i} \text{Cos}(\theta) + \mathbf{j} \text{Sin}(\theta)) \quad (3.13)$$

and the short-time average is given by,

$$E(t)E^*(t) = |A(t - \frac{D}{v_{ge}})|^2 \text{Cos}^2(\theta) + \rho^2 |A(t - \frac{2d}{c} - \frac{D}{v_{go}})|^2 \text{Sin}^2(\theta) \\ + 2\rho A(t - \frac{D}{v_{ge}})A(t - \frac{2d}{c} - \frac{D}{v_{go}}) \text{Cos}(\omega \frac{2d}{c} + \frac{\bar{\omega}(n_e - n_o)D}{c}) \quad (3.14)$$

It can be noted that for a quarter wave plate

$$\frac{\bar{\omega}(n_e - n_o)D}{c} = (2n + 1) \frac{\pi}{2} \quad (3.15)$$

where n is the order of the plate.

Hence the long-term average intensity is given by

$$I(\theta) = \int_{-\infty}^{\infty} E(t)E^*(t)dt \quad (3.16)$$

$$= I_a \text{Cos}^2(\theta) + \rho^2 I_a \text{Sin}^2(\theta) - 2(-1)^n I'_{\otimes}(d) \text{Cos}(\theta) \text{Sin}(\theta) \text{Sin}(\omega \frac{2d}{c}) \quad (3.17)$$

where

$$I_a = \int_{-\infty}^{\infty} |A(t)|^2 dt \quad (3.18)$$

and

$$I'_{\otimes}(d) = \int_{-\infty}^{\infty} A(t - \frac{D}{v_{go}})A(t - \frac{2d}{c} - \frac{D}{v_{ge}})dt \quad (3.19)$$

It follows that

$$p_{3(chrom)} = \frac{I_{Right} - I_{Left}}{I_{Right} + I_{Left}} = (-1)^n \left(\frac{2\rho}{1 + \rho^2} \right) \left(\frac{I'_{\otimes}(d)}{I_a} \right) \text{Sin}(\omega \frac{2d}{c}) \quad (3.20)$$

Hence the result for detecting the amount of circularly polarised light depends on whether or not chromatic wave plates are used. For example figure 3.9 shows a $|\mu_{xy}|$ vs. d curve for a source with coherence length l_c of 8λ measured with a zero order chromatic wave plate. Perturbations are

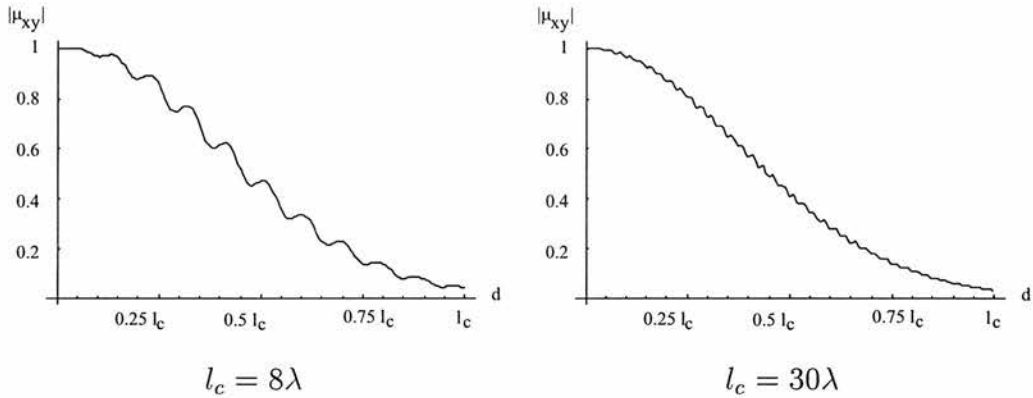


Figure 3.9: Figure showing $|\mu_{xy}|$ measured with a zero order chromatic wave plate for for two different source with different coherence lengths.

visible, but as the coherence length increases the fringing decreases. Also as the order of the wave plate increases, the perturbations in the curve decrease.

As the coherence length becomes longer these effects are much reduced and the difference between using a zero order chromatic and zero order achromatic becomes negligible.

The problem of determining the polarisation state of light with short coherence lengths after passing through birefringent elements is given a more general treatment in the following chapter.

3.4.1 $p_{3(chrom)}$ vs. p_3

It is interesting to note that the ratio of $p_{3(chrom)}$ to p_3 varies with d and is independent of ρ . Figure 3.10 show the ratio of $p_{3(chrom)}$ to p_3 for two different situations. Hence it would appear to be possible to correct for the errors introduced by a high order chromatic wave plate if its properties are known.

$$\frac{p_{3(chrom)}}{p_3} = \frac{I'_{\otimes}(d)}{I_{\otimes}(d)} = (-1)^n \int_{-\infty}^{\infty} \frac{A(t)A(t - \frac{2d}{c} + \frac{D}{v_{ge}} - \frac{D}{v_{go}})}{A(t)A(t - \frac{2d}{c})} dt \quad (3.21)$$

Also from the graphs it appears that it might be possible to determine the profile of a surface by measuring the circularly polarised light with a high order chromatic wave plate ($p_{3(chrom)}$) and an achromatic or zero order wave plate (p_3) and ratioing them. However the properties of the wave plates used would have to be exactly known.

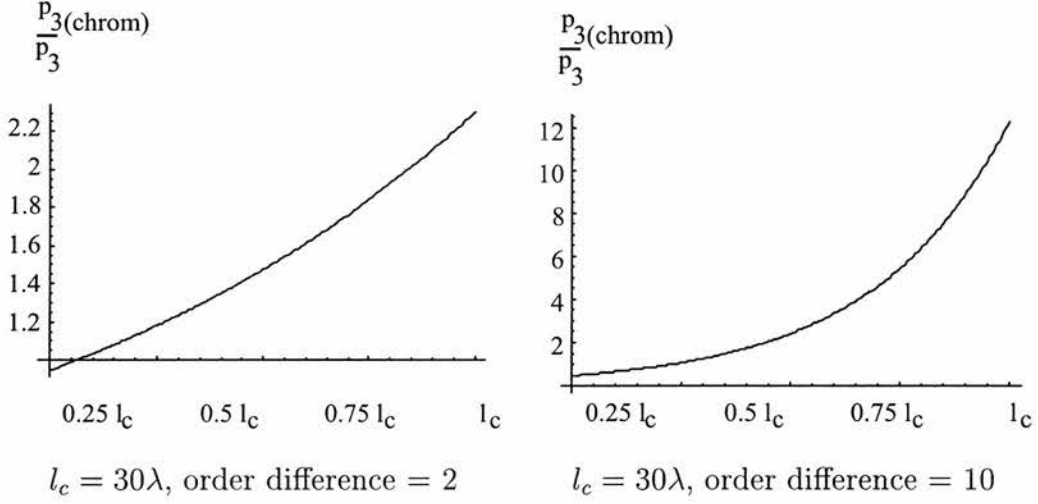


Figure 3.10: Graphs showing the ratio of $p_{3(chrom)}$ to p_3 for two different situations.

3.5 $|\mu_{xy}|$ and the Fourier transform

It can be shown that for a given spectrum p_2 and p_3 can be calculated via a Fourier transform. The full expression for $|\mu_{xy}|$ is given by

$$|\mu_{xy}| = \frac{I_{\otimes}}{I_a} = \int_{-\infty}^{\infty} \frac{A(t)A(t-t_d)}{[A(t)]^2} dt \quad (3.22)$$

which is the convolution of the two wave packets, which by the Weiner-Kinchine theorem[52] is equal to the Fourier transform of the power spectrum,

$$|\mu_{xy}| = \int |S(\omega)|^2 e^{-i\omega t} d\omega \quad (3.23)$$

And by considering the Fourier transform of the spectrum,

$$\mathcal{F}\{S(\omega)\} = \int S(\omega)e^{-i\omega t}d\omega = \int S(\omega)\text{Cos}(\omega t) + i \int S(\omega)\text{Sin}(\omega t) \quad (3.24)$$

and the last two terms on the right can be shown to be equal to p_2 and p_3 . Hence

$$\mathcal{F}\{S(\omega)\} = p_2 + i p_3 \quad (3.25)$$

Thus the real and imaginary components of the Fourier transform of the spectrum give p_2 and p_3 . Hence in the case where $p_1 = 0$, the above relationships can be used to create lookup tables of p_2 and p_3 as a function of t and $|\mu_{xy}|$ so the surface can be calculated very quickly.

3.5.1 Sinc spectrum

Since $|\mu_{xy}|$ and the power spectrum form a Fourier pair, the $|\mu_{xy}|$ curve can be tailored by choice of an appropriate power spectrum. If a linear relationship between $|\mu_{xy}|$ and pulse overlap is required then a sinc^2 power spectrum should be used, where the sinc function is defined as

$$\text{sinc}(x) = \frac{\text{Sin}(x)}{x} \quad (3.26)$$

and it can be shown by L'Hopital's rule[55] that $\text{sinc}(0) = 1$. A sinc^2 power spectrum can be achieved through use of a Solc filter[56]. A Solc filter is a filter made of birefringent elements[57] interspersed with polarisers in such a way that one wavelength is correctly rotated to pass through the system, all other wavelengths being reduced by the polarisers[58]. Use of a sinc^2 power spectrum results in square wave packets which in turn gives a linear relationship between $|\mu_{xy}|$ and d removing the need for image processing to determine the true profile of the surface.

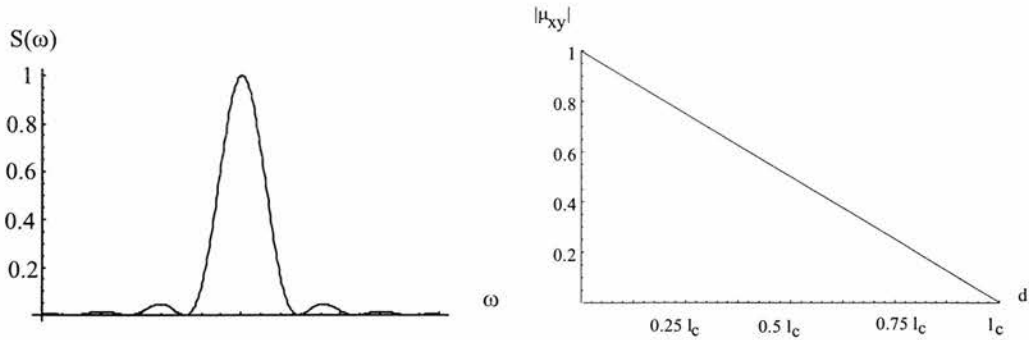


Figure 3.11: A sinc^2 power spectrum and resultant $|\mu_{xy}|$ curve.

3.6 Hanbury-Brown and Twiss interferometer

A Hanbury-Brown Twiss interferometer is an interferometer used to determine stellar diameter. Figure 3.12 shows a simple Hanbury-Brown Twiss interferometer[52]. The delay line τ is used so that the signals from the mirrors arrive at the multiplier C at the same time. The photo-current detected is proportional to the time-integrated optical intensity. The correlation of the photo-currents is proportional to the correlation of the optical intensities. The mirror separation is varied and the correlation is measured as a function of mirror separation[52]. It is interesting to note that the correlation measured is actually $|\mu_{xy}|$ [59] and a possible alternative use of the polarisation algorithm described in this work would be in a Hanbury-Brown Twiss interferometer. Use of this polarisation algorithm would avoid the need for expensive correlation electronics and would simplify the system dramatically through allowing the use of simple detectors.

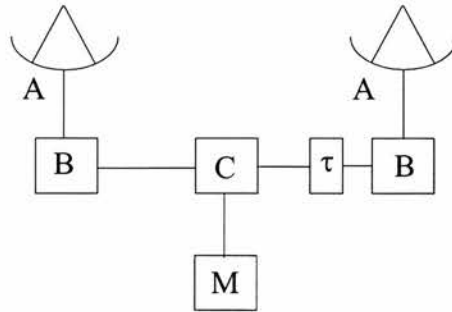


Figure 3.12: A Hanbury-Brown and Twiss interferometer. (A Mirrors, B Amplifiers, C multiplier, M Integrator)

3.7 Conclusions

The mathematical analysis and modelling agrees with the experimental results and have allowed us further to understand how the $|\mu_{xy}|$ method works. The necessity for accurately aligned polarisers and well chosen wave plates was also noted. By use of a Poincaré sphere it was also shown how to correct for use of incorrect wave plates. Significantly it was noted that it is possible to tailer the $|\mu_{xy}|$ vs. d curve by choice of the appropriate spectrum.

Chapter 4

Modelling the performance of birefringent wave plates

4.1 Polarisation state of light

Measuring the polarisation state of light after reflection from or transmission through a medium is commonly used in such areas as ellipsometry [60], photoelasticity [61] and polarisation studies of biomolecular structures [62]. The polarisation state of light can be described in terms of three Stokes parameters p_1 , p_2 and p_3 , as defined previously.

Measuring p_1 and p_2 is straightforward since linear polarisers are available with extinction ratios in excess of 10^6 and bandwidths over one octave, centered at any wavelength throughout the optical and near optical regions of the spectrum. However, measurement of p_3 is more problematic since the intensity of circular polarisation cannot be measured directly. The degree of circular polarisation is inferred by measuring the degree of linear polarisation after passing the light through a quarter-wave plate.

Various design limitations of birefringent wave plates such as field of

view[63] and frequency mis-match[64] have been considered previously. This chapter considers the effects of using light sources of different bandwidths with various designs of wave plate and shows that the errors arising due to problems associated with coherence lengths are substantially larger than the thickness and field of view effects described by West and Smith[63]. In what follows the phase shift for each spectral component within the source is evaluated and the Stokes parameters of the transmitted light calculated.

4.2 Modelling the performance of various wave plate designs

A light source can be described either in terms of its amplitude spectrum $S(\omega)$ or the temporal form of the photon wave function, $f(t)$. These two are related by the Fourier transform relationship such that

$$f(t) = \int_{-\infty}^{\infty} S(\omega)e^{-i\omega t}d\omega. \quad (4.1)$$

The amplitude spectrum can be expressed as a power spectrum by multiplication with its complex conjugate. In the case of a bandwidth limited source this wave function is identical to the temporal form of the electric field.

The two orthogonal polarisations are referred to as the ordinary and extraordinary components. After passing through a wave plate of thickness D the phase shift ϕ is given by

$$\phi_o(\omega) = \frac{\omega n_o(\omega)D}{c} \quad (4.2)$$

$$\phi_e(\omega) = \frac{\omega n_e(\omega) D}{c} \quad (4.3)$$

where $n_o(\omega)$ and $n_e(\omega)$ are the refractive indices for the ordinary and extra-ordinary polarisations respectively as a function of ω . For the modelling, the wavelength dependent refractive indices of the various material were calculated using the Sellmeier equations[65].

In the temporal domain the photon wave functions are given by the following Fourier transforms

$$f_e = \int_{-\infty}^{\infty} S_e(w) e^{i[\omega t + \phi_e(\omega)]} d\omega \quad (4.4)$$

$$f_o = \int_{-\infty}^{\infty} S_o(w) e^{i[\omega t + \phi_o(\omega)]} d\omega. \quad (4.5)$$

The corresponding light intensity is given by multiplying by the appropriate complex conjugate.

By defining the measurement axes such that the e-ray and o-ray polarisation correspond to measurement at 0° and 90° respectively, the transmitted intensities are given by

$$I_0 = \int_{-\infty}^{\infty} f_e f_e^* dt \quad (4.6)$$

$$I_{90} = \int_{-\infty}^{\infty} f_o f_o^* dt \quad (4.7)$$

$$I_{45} = \int_{-\infty}^{\infty} (f_e + f_o)(f_e^* + f_o^*) dt \quad (4.8)$$

$$I_{135} = \int_{-\infty}^{\infty} (f_e - f_o)(f_e^* - f_o^*) dt. \quad (4.9)$$

As discussed previously I_{Right} and I_{Left} cannot be measured directly. The intensity of circularly polarised light can be inferred by measuring the degree of linear polarisation after passage through a quarter wave plate. This is achieved by multiplying by $S_e(\omega)$ by $e^{i\pi/2}$ and performing an inverse Fourier transform to produce f_c , *i.e.*

$$f_c = \int_{-\infty}^{\infty} S_e(\omega) e^{i[\omega t + \phi_e(\omega) + \pi/2]} d\omega. \quad (4.10)$$

The circular polarisation intensities I_{Right} and I_{Left} are then evaluated as

$$I_{Right} = \int_{-\infty}^{\infty} (f_c + f_o)(f_c^* + f_o^*) dt \quad (4.11)$$

$$I_{Left} = \int_{-\infty}^{\infty} (f_c - f_o)(f_c^* - f_o^*) dt. \quad (4.12)$$

Given these intensity measurements each of the Stokes parameters can be calculated for arbitrary spectral distributions and wave plate designs.

4.2.1 Sellmeier Data

To determine the refractive index as a function of λ rather than using discrete points Sellmeier data was used. Sellmeier data takes the form of the equation[66]

$$n(\lambda) = \sqrt{\alpha + \frac{\beta}{1 - \frac{\gamma}{\lambda^2}} - \delta\lambda^2} \quad (4.13)$$

where the coefficients α, β, γ and δ are material specific. λ is given in microns. Table 4.1 shows the Sellmeier coefficients for the materials used in this chapter.

Material	index	α	β	γ	δ
ADP	o	1.564	.07369	0.0154	0.0373
ADP	e	1.489	0.6731	0.0141	0.01454
MgF	o	1.882	0.0113	0.1305	0.00866
MgF	e	1.354	0.5637	0.00831	0.0044
Quartz	o	1.5916	0.7656	0.0136	0.01157
Quartz	e	1.6055	0.7789	0.0139	0.0121

Table 4.1: Sellmeier coefficients for various materials

4.3 Design of birefringent wave plates

For a specific frequency the optimum thickness of birefringent wave plate is given by

$$D = \frac{2\pi}{\omega} (n + \Gamma) \frac{1}{|n_e(\omega) - n_o(\omega)|} \quad (4.14)$$

where n is an integer and called the order of the wave plate, and Γ is either $\frac{1}{2}$ or $\frac{1}{4}$ for a half or quarter wave plate respectively. The lower the order greater the acceptance angle and bandwidth of the wave plate. However, for most birefringent materials the calculated thickness for a zero order wave plate is only a few microns. For apertures larger than a few millimeters this manufacturing requirement is too demanding and in practice a zero order wave plate is manufactured from two wave plates with orthogonal axes with orders that differ by one. Higher order wave plates are easier to manufacture since the material is polished until the required retardation is obtained without reference to the overall thickness of the wave plate.

Whatever the order of the wave plate, clearly it only produces the required retardation at one specific design wavelength which is often specified to an accuracy of 0.5%. Broadband wave plates can be manufactured using either Fresnel rhombs or combinations of materials with opposite signs of birefringence. Fresnel Rhombs are bulky and quarter-wave Rhombs re-

sult in a displacement of the transmitted beam. Broadband birefringent wave plates are formed from two or three different materials of specific thicknesses. Recognised designs exist[67] such that the total dispersion of the material combination approximately maintains a constant phase thickness across spectral range of interest. Although the phase flatness of these achromatic wave plate is much improved over that of a zero order plate (see figure 4.1) it is important to realise that they are not truly achromatic.

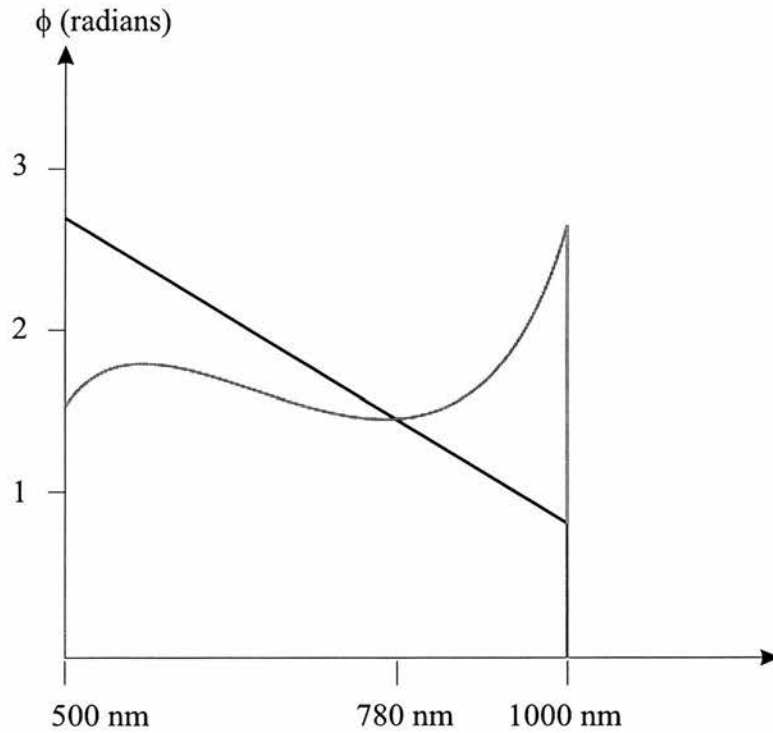


Figure 4.1: Phase imparted by a quartz zero-order quarter wave plate (black line) and by an achromatic quarter wave plate (wave plate 1 in the tables) (grey table) optimised for 780nm

4.4 Numerical investigation of various design of wave plate

Here *Mathematica 3.0* is used to numerically model the performance of zero order, multiple order and achromatic birefringent wave plates[67, 68] with light sources of various bandwidths. Any truly monochromatic source when used with any of these wave plate designs gives perfectly polarised light. The situation becomes more interesting when the bandwidth of the source is made finite. The light sources modelled in this work are a Ti:Sapphire femto-second pulsed laser centered at $780nm$ with a transform limited bandwidth of $20nm$, a tungsten bulb centered at $800nm$ with a bandwidth of $120nm$ and a tungsten bulb by an interference filter centered at $633nm$ and a bandwidth of $1nm$. In each of the cases the wave plates were optimised for the wavelength in question. Also it was assumed in all cases that the light could be modelled with a Gaussian spectrum. The results are, in general, insensitive to the form of the spectrum chosen but any spectra with strong lines over the range of interest could have a small, but significant, effect.

Ideally a quarter-wave plate transforms linearly polarised light into circularly polarised light or vice versa. Given a linearly polarised input beam, ($p_1 = 0$, $p_2 = 1$ and $p_3 = 0$), the performance of the various combinations of light source and wave plate design is assessed by calculating the degree of circular polarisation of the transmitted light, *i.e.* p_3 . Tables 4.2, 4.3 and 4.4 detail the various design of birefringent quarter-wave plates investigated and their performance with the different light sources. As discussed in section 3, true zero-order wave plates are often too thin to manufacture. Also a pseudo zero-order wave plate, which is formed by two thicker pieces of birefringent material, is modelled.

Order	Material & Thickness	p_3
0	22.48 μm of Quartz	0.984
1	112.43 μm of Quartz	0.672
5	472.22 μm of Quartz	0.001
Pseudo 0	472.22 μm and 494.70 μm of Quartz	0.983
Pseudo 0 optimised for 633nm	384.7 μm and 419.7 μm of Quartz	0.897
Achromatic Wave Plate 1	97.72 μm of MgF ₂ and 22.29 μm of ADP	0.988
Achromatic Wave Plate 2	167.56 μm of Quartz and 143.09 μm of MgF ₂	0.910

Table 4.2: Tungsten bulb source centered at 800nm, predicted values of p_3 for various quarter wave plate designs

Order	Material & Thickness	p_3
0	21.9 μm of Quartz	0.999
1	109.5 μm of Quartz	0.988
5	459.9 μm of Quartz	0.819
Pseudo 0	459.9 μm and 481.8 μm of Quartz	0.999
Pseudo 0 optimised for 633nm	384.7 μm and 419.7 μm of Quartz	0.950
Achromatic Wave Plate 1	97.72 μm of MgF ₂ and 22.29 μm of ADP	0.984
Achromatic Wave Plate 2	167.56 μm of Quartz and 143.09 μm of MgF ₂	0.951

Table 4.3: Femto-second laser source centered at 780nm, predicted values of p_3 for various quarter wave plate designs

Order	Material & Thickness	p_3
0	17.4 μm of Quartz	0.999
1	87.4 μm of Quartz	0.999
5	376.3 μm of Quartz	0.996
Pseudo 0	376.3 μm and 384.7 μm of Quartz	0.999
Achromatic Wave Plate 1	97.72 μm of MgF ₂ and 22.29 μm of ADP	0.997
Achromatic Wave Plate 2	167.56 μm of Quartz and 143.09 μm of MgF ₂	0.995

Table 4.4: Filtered white light centered at 633nm with 1nm bandwidth, predicted values of p_3 for various quarter wave plate designs

For an ideal wave plate the value of p_3 in each of these cases should be unity. However, even for a monochromatic source with a precisely specified wavelength, errors in p_3 will arise due to manufacturing tolerance. Wave plates are typically manufactured with a retardation accuracy of 0.5%, which for a monochromatic light source would result in a circularly polarised light beam with a value of p_3 between 0.9994 and unity. In practice the performance of a wave plate is often limited further by factors such as misalignment of its fast axis or finite field-of-view such that p_3 does not exceed 0.99[63]. It is useful to bear this figure in mind when assessing the suitability of wave plates discussed in this paper.

A half-wave plate rotates the plane of linear polarisation by twice the angle between the input polarisation and the axes of the wave plate. Similarly, upon transmission, it reverses the sense of circular polarisation, *i.e.* $p_3 = -1$ changes to $p_3 = 1$. To investigate the performance of various half wave plate designs, we considered fully circularly polarised light ($p_3 = -1$) incident upon a half wave plate and calculated the Stokes parameters of the transmitted light. A perfect half wave plate should change $p_3 = -1$ into $p_3 = 1$. Tables 4.5, 4.6 and 4.7 detail the various design of birefringent half-wave plates and their performance with the different light sources.

Order	Material & Thickness	p_3
0	44.9 μm of Quartz	0.938
1	134.9 μm of Quartz	0.567
5	494.7 μm of Quartz	0.001
Pseudo 0	494.7 μm and 539.6 μm of Quartz	0.936
Pseudo 0 optimised for 633nm	384.7 μm and 419.7 μm of Quartz	0.713
Achromatic Wave Plate 1	195.44 μm of MgF ₂ and 44.58 μm of ADP	0.952
Achromatic Wave Plate 2	335.12 μm of Quartz and 286.18 μm of MgF ₂	0.978

Table 4.5: Tungsten bulb source centered at 800nm, predicted values of p_3 for various half wave plate designs

Order	Material & Thickness	p_3
0	43.8 μm of Quartz	0.998
1	131.4 μm of Quartz	0.984
5	481.8 μm of Quartz	0.793
Pseudo 0	481.8 μm and 525.6 μm of Quartz	0.998
Pseudo 0 optimised for 633nm	384.7 μm and 419.7 μm of Quartz	0.806
Achromatic Wave Plate 1	195.44 μm of MgF ₂ and 44.58 μm of ADP	0.937
Achromatic Wave Plate 2	335.12 μm of Quartz and 286.18 μm of MgF ₂	0.814

Table 4.6: Femto-second laser source centered at 780nm, predicted values of p_3 for various half wave plate designs

Order	Material & Thickness	p_3
0	34.9 μm of Quartz	0.999
1	104.9 μm of Quartz	0.999
5	384.7 μm of Quartz	0.999
Pseudo 0	384.7 μm and 419.7 μm of Quartz	0.999
Achromatic Wave Plate 1	195.44 μm of MgF ₂ and 44.58 μm of ADP	0.989
Achromatic Wave Plate 2	335.12 μm of Quartz and 286.18 μm of MgF ₂	0.981

Table 4.7: Filtered white light centered at 633nm with 1nm bandwidth, predicted values of p_3 for various half wave plate designs

In general a decrease in p_3 is accompanied by an overall decrease in P . Although this corresponds to an overall decrease in polarisation the process is reversible by passing the light through an idealised compensation plate with the opposite birefringence, or an identical wave plate rotated by 90° . The reversibility of this process means that the apparent reduction in P can be considered to correspond to a pseudo-depolarisation [69].

4.5 Conclusions

A method for precisely modelling the performance of specific wave plate designs when used with light sources of arbitrary bandwidths has been presented. The method calculates numerically the phase delay introduced to each spectral component of the light source. A Fourier transform of the transmitted amplitude spectrum gives the photon wave function which can be used to calculate the corresponding intensity and related Stokes polarisation parameters. As anticipated for sources with large bandwidths care needs to be taken in selecting an appropriate wave plate design. As expected increasing the order of the wave plate and its corresponding thickness reduces its performance for broad bandwidth light sources in particular. Note, for the white light source even the zero order wave plate shows reduced performance. This is particularly true for the half wave plate where its inherently larger thickness reduces its performance compared with the quarter wave plate.

It is also interesting to note that the performance of nominally achromatic wave plates varies significantly between different recognised designs. Care should be taken to ensure that the detailed design selected is optimised for the specific application. For example, if the application uses a monochromatic or quasi-monochromatic source it is better to select a low order wave plate

optimised for the source wavelength rather than use an achromatic design.

Even under ideal conditions real wave plates are unlikely to produce polarised light beams with Stokes parameters in excess of 0.99. This can be considered to be an upper limit to the performance achievable with a wave plate fabricated from birefringent materials and optimising the design beyond this is unlikely to yield observable improvement. This chapter is based upon a paper published in *Optical and Quantum electronics* by Lesso *et al.*, "A Technique for modelling the performance of birefringent wave plates", Vol 32, pages 645-653, 1999.

Chapter 5

Ray Tracing in Birefringent Media

In order to understand the optical properties of birefringent elements it was decided a birefringent ray tracing should be written. The object of this was to enable the design of interferometers for profilometry based around birefringent components.

Ray tracing is used to determine the path that light takes through an optical system. To a good approximation rays can be regarded as the paths along which radiation travels[70]. The approximation breaks down near foci and edge of shadows due to diffraction effects but in geometrical optics these effects are ignored[71]. Figure 5.1 shows a point source A and some rays leaving the source and traveling through the optical system. To travel from point A to B takes a time

$$t_{AB} = \frac{1}{c} \int_A^B n \, ds \quad (5.1)$$

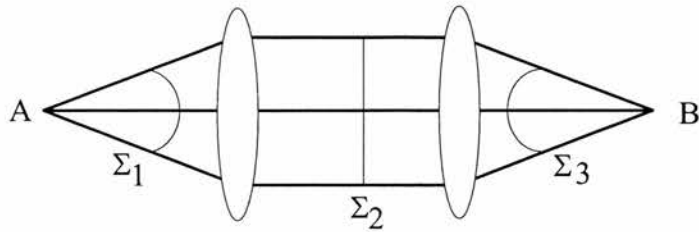


Figure 5.1: A point being imaged to a point, showing the wavefronts in the system.

or more generally the optical path length, OPL , is given by

$$OPL = \int n \, ds \quad (5.2)$$

It also necessary to introduce the concept of a wavefront. In figure 5.1 the surfaces Σ_1 , Σ_2 and Σ_3 are all wavefronts – *i.e.* they represent surfaces of constant phase. In the study of aberrations in an optical system the wavefront is a very important concept.

5.1 Fermat's principle

A very simple and elegant method to determine that path of rays was proposed by Fermat in 1667. Simply stated Fermat's principle is that the path a ray takes between two points rays takes is not necessarily a minimum but is stationary. Fermat's principle can be expressed as

$$\frac{\partial OPL}{\partial x_i} = \frac{\partial OPL}{\partial y_i} = 0 \quad (5.3)$$

where x_i and y_i are the points of intersection at successive surfaces. The fact that light travels in straight lines can be proved using Fermat's principle, as can the law of refraction which is better known as Snell's Law[48].

5.2 Huygen's Construction

Huygen's construction[72] can be used to derive the laws of reflection and refraction. Huygens construction is a simple continuation of Huygens principle which states that the effects of propagation upon a wavefront can be determined by generating secondary wavelets at every point along the wavefront. The superposition of these secondary wavefronts can then be used to determine the ultimate shape of the wavefront.

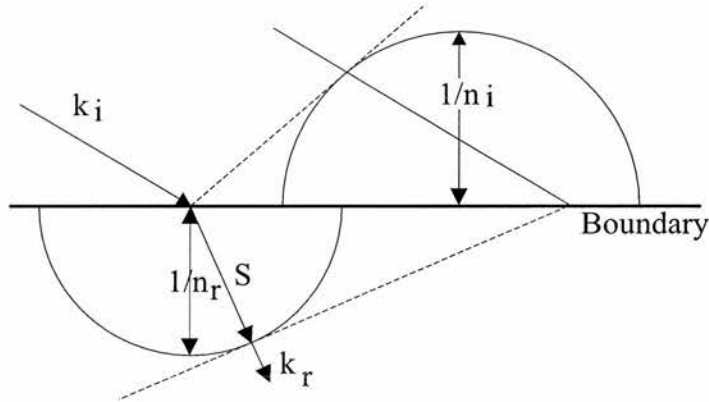


Figure 5.2: Huygen's construction for isotropic media

Figure 5.2 shows a simple Huygen's construction used to determine the path taken by a refracted ray. Huygen's construction involves plotting a wave velocity surface (WVS) and plotting the tangents to the WVS to determine the ultimate ray direction. The WVS is a surface representing the wavefront emerging from a point source, as shown in figure 5.3. For isotropic media the WVS is a sphere of radius $1/n_o$ where n_o is the refractive index of the medium.

The path taken by the rays (*i.e.* the photons) is given by the Poynting vector, \mathbf{S} . As can be seen from figure 5.2 for isotropic media the normal to the wavefront \mathbf{k}_r and the Poynting vector \mathbf{S} are co-linear. Hence the calculation

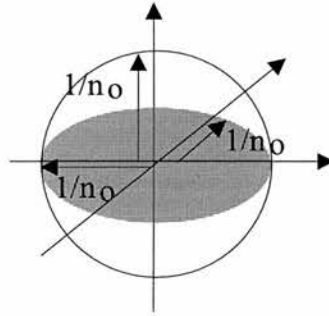


Figure 5.3: Wave velocity surface for isotropic media

of either \mathbf{k}_r or \mathbf{S} determines the path of the ray.

5.3 Snell's Law

The path taken by a refracted ray can be calculated using the law of refraction, Snell's law. It can be expressed in vectorial form as[73]

$$n_i \{\mathbf{k}_i \times \mathbf{n}\} = n_r \{\mathbf{k}_r \times \mathbf{n}\} \quad (5.4)$$

where n_i and n_r are the refractive indices, \mathbf{n} is the unit normal to the surface and \mathbf{k}_i and \mathbf{k}_r are the wave vectors of the incident and refracted waves. Most commercially available ray-tracers use this equation at successive surfaces to determine the path of rays through isotropic media. Snell's Law can also be used for reflection simply by changing n_r for $-n_i$.

5.3.1 Vectorial form of Snell's Law

Snell's Law in the form of equation 5.4 is not in a practical form. To change it into a more usable form first let $\mu = n_i/n_r$, then

$$\mathbf{k}_r \times \mathbf{n} = \mu(\mathbf{k}_i \times \mathbf{n}) \quad (5.5)$$

hence

$$(\mathbf{k}_r - \mu\mathbf{k}_i) \times \gamma\mathbf{n} = 0 \quad (5.6)$$

thus $\mathbf{k}_r - \mu\mathbf{k}_i$ and \mathbf{n} are parallel. To determine γ , square equation 5.6 to obtain

$$1 = \mu^2 + \gamma^2 + 2 * \gamma * \mu(\mathbf{k}_i \cdot \mathbf{n}) \quad (5.7)$$

hence solving for γ ,

$$\gamma = -\mu(\mathbf{k}_i \cdot \mathbf{n}) + \sqrt{(1 - \mu^2(1 - ((\mathbf{k}_i \cdot \mathbf{n}))^2))} \quad (5.8)$$

thus

$$\mathbf{k}_r = \mu\mathbf{k}_i + \gamma\mathbf{n} \quad (5.9)$$

5.4 Ray tracing in birefringent media

Birefringent crystals are anisotropic due to their crystal structure. In this work only uniaxial, *i.e.* with one optical axis, birefringent crystals are considered. If a ray has its \mathbf{E} vector polarised perpendicularly to the optic axis, the ray is called an ordinary ray (o-ray) and the refractive index is equal to n_o and Snell's law can be used to determine the path through the crystal.

However if a ray is polarised so that \mathbf{E} has a component parallel to the optic axis then the ray is called the extra-ordinary ray (e-ray), and experiences a refractive index between n_e and n_o . Snell's law cannot be used to determine the path the e-ray takes.

5.4.1 Variable refractive index

The WVS for a negatively birefringent material (*i.e.* $n_e < n_o$) is shown in figure 5.4. Since the WVS is essentially a measure of refractive index and the WVS is elliptical in birefringent media the refractive index n_{eff} varies

between n_o and n_e , depending on the direction of the wave vector \mathbf{k}_r relative to the optic axis, denoted by the vector \mathbf{z}_3 .

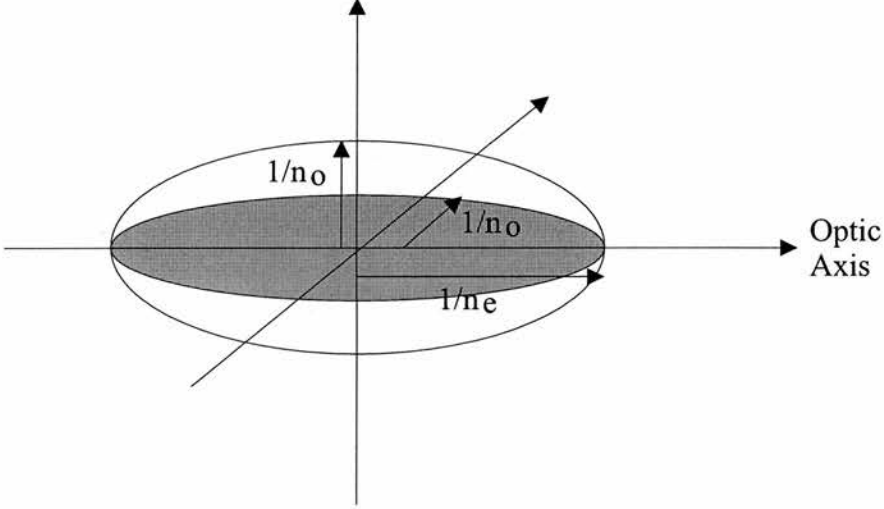


Figure 5.4: Wave velocity surface for birefringent media

By considering the geometry of the WVS for a birefringent media the refractive index can be shown[18] to be equal to

$$n_{eff}(\mathbf{k}_r, \mathbf{z}_3) = \frac{n_e n_o}{\sqrt{n_e^2(1 - (\mathbf{k}_r \cdot \mathbf{z}_3)^2) + n_o^2(\mathbf{k}_r \cdot \mathbf{z}_3)^2}}. \quad (5.10)$$

Hence in birefringent media, the refraction law can be expressed as

$$n_i \{\mathbf{k}_i \times \mathbf{n}\} = \frac{n_e n_o \{\mathbf{k}_r \times \mathbf{n}\}}{\sqrt{n_e^2(1 - (\mathbf{k}_r \cdot \mathbf{z}_3)^2) + n_o^2(\mathbf{k}_r \cdot \mathbf{z}_3)^2}}. \quad (5.11)$$

This equation is non-trivial to solve for \mathbf{k}_r . Various techniques [74, 75, 76, 77] have been proposed to overcome this problem and the algorithm used in this paper is derived from the technique developed by Simon and Echarri[78]. We have incorporated their algorithm into a ray-tracing package that we have developed based on the *Mathematica* application.

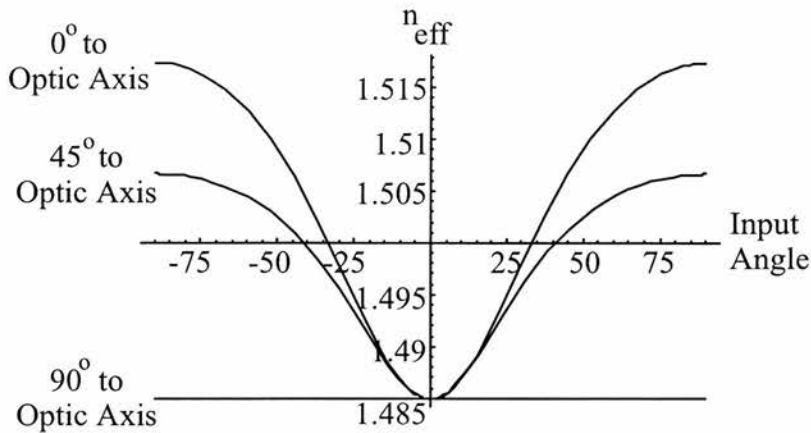


Figure 5.5: Graph showing how refractive index varies with input angle and input plane for Calcite

Figure 5.5 shows how refractive index varies with input angle for a variety of input planes for Calcite. It is interesting to note that for the plane 90° to the optic axis n_{eff} is constant for all input angles. Also if the input angle relative to the normal is 0° then for all planes n_{eff} is constant. In these two cases Snell's law *can* be used to determine the \mathbf{k} vector for the e-ray[79].

5.4.2 Poynting Vector *vs.* the wave vector

Another problem is that the \mathbf{k} vector and \mathbf{S} vector are not parallel for birefringent media[18]. Figure 5.6 shows a Huygen's construction for birefringent media. As can be seen due to the elliptical WVS for the e-ray the Poynting vector and wave vector are not parallel.

Once \mathbf{k}_e has been determined the propagation direction, \mathbf{S} , is given by[80]

$$\mathbf{S} = \mathbf{k}_e \left(\frac{n_o}{c}\right)^2 + \left(\left(\frac{n_o}{c}\right)^2 - \left(\frac{n_e}{c}\right)^2\right) (\mathbf{k}_e \cdot \mathbf{z}_3) \mathbf{z}_3 \quad (5.12)$$

Our package can perform simple ray-tracing operations on single or multi-element optical systems incorporating birefringent materials. Optical path

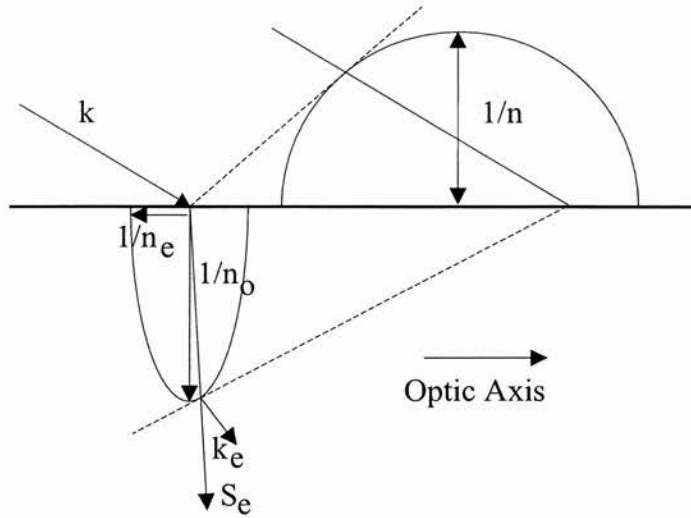


Figure 5.6: Huygen's construction for the e-ray in birefringent media

length is also calculated, which allows the package to be used for modelling interferometers incorporating birefringent elements.

5.5 Ray Tracing algorithm

To demonstrate how to ray trace in birefringent media a ray intersecting a slab of birefringent material as shown in figure 5.7 is now considered. The ray is traveling from a medium of refractive index n to a birefringent medium of refractive indices n_e and n_o , and then finally entering an isotropic medium of refractive index n . The path of e and e-rays are considered separately below.

5.5.1 o-ray

The o-ray case is the simplest where Snell's law is used to determine the direction of the ray in birefringent media with a constant refractive index of n_o . On entering the media Snell's law is sufficient to determine ray direction

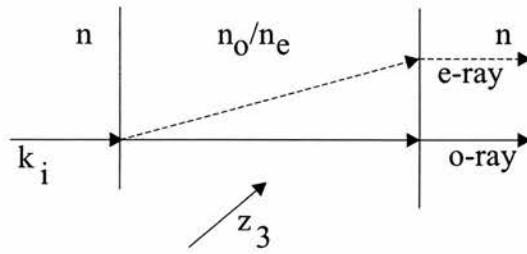


Figure 5.7: Rays traveling in birefringent media.

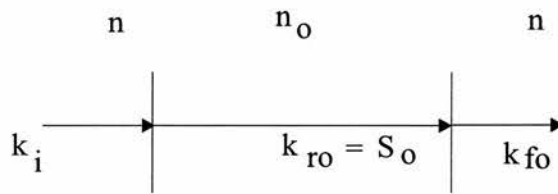


Figure 5.8: Relevant vectors for determining the path of the o-ray in birefringent media.

since $\mathbf{k}_{ro} = \mathbf{S}_o$. The final refracted vector \mathbf{k}_{fo} is found by putting \mathbf{k}_{ro} in to Snell's law.

5.5.2 e-ray

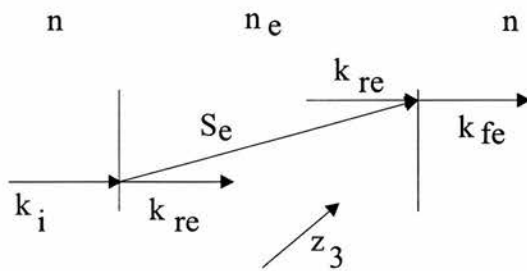


Figure 5.9: Relevant vectors for determining the path of the e-ray in birefringent media.

The e-ray case is more complex. To solve equation 5.11 the method of Simon and Echarri[78] was used. They use a geometrical argument to

determine the effective refractive index of the material hence allowing Snell's Law to be used to determine \mathbf{k}_r . Here the mechanics of their approach is given.

First let

$$b = \frac{u_o^2 - u_e^2}{u^2} \quad (5.13)$$

where $u_o = \frac{n_o}{c}$ and $u_e = \frac{n_e}{c}$ and $u = \frac{n}{c}$, n being the refractive index on the other side of the discontinuity. Then let

$$\alpha = (1 + b * (1 - (\mathbf{k}_i \cdot \mathbf{n})^2 - (\mathbf{k}_i \cdot (\mathbf{n} \times \mathbf{z}_3))^2))^2 - 4 * b * ((1 - (\mathbf{k}_i \cdot \mathbf{n})^2 * (1 - (\mathbf{z}_3 \cdot \mathbf{n})^2) - (\mathbf{k}_i \cdot (\mathbf{n} \times \mathbf{z}_3))^2) \quad (5.14)$$

and also

$$\beta = 2 * (1 + b * (1 - (\mathbf{k}_i \cdot \mathbf{n})^2 - (\mathbf{k}_i \cdot (\mathbf{n} \times \mathbf{z}_3))^2)) * (b * (\mathbf{n} \cdot \mathbf{z}_3)^2 + (\frac{u_e}{u})^2) - 4 * b * (\frac{u_e}{u})^2 * ((1 - (\mathbf{k}_i \cdot \mathbf{n})^2) * (1 - (\mathbf{z}_3 \cdot \mathbf{n})^2) - (\mathbf{k}_i \cdot (\mathbf{n} \times \mathbf{z}_3))^2) \quad (5.15)$$

and

$$\gamma = (b * (\mathbf{z}_3 \cdot \mathbf{n})^2 + (\frac{u_e}{u})^2) \quad (5.16)$$

Then if $\mathbf{n} \times \mathbf{z}_3 = 0$

$$W = \sqrt{\frac{\beta}{2\alpha}} \quad (5.17)$$

otherwise let

$$\xi = \mathbf{n} \times (\mathbf{n} \times \mathbf{z}_3) \quad (5.18)$$

$$W = \sqrt{\frac{\beta + \text{Sign}[(u_o - u_e) * (\xi \cdot \mathbf{z}_3) * (\mathbf{k}_i \cdot \xi)] * \sqrt{\beta^2 - 4 * \alpha * \gamma}}{2\alpha}} \quad (5.19)$$

where $\text{Sign}[x] = +1$ if x is 0 or positive and $\text{Sign}[x] = -1$ if x is negative. Once W has been determined the effective refractive index of the medium is

given by

$$n_{eff} = \frac{n}{W} \quad (5.20)$$

Then Snell's Law can be used to determine \mathbf{k}_{re} . Then using equation 5.12 \mathbf{S}_e , *i.e.* the direction the ray takes can be determined. Using this method the optical path length is given by

$$OPL = n_{eff} * l_S \quad (5.21)$$

where l_S is the distance from one interface to the other taken by the \mathbf{S}_e vector. The \mathbf{S}_e vector is used to determine the point of contact with the next surface, but since the next material is isotropic the \mathbf{k}_{ro} vector, not \mathbf{S}_e , is used with Snell's law to determine \mathbf{k}_{ef} .

5.6 Conclusions

This chapter has shown that ray tracing in birefringent media is considerably more complex than ray tracing in isotropic media and a method for ray tracing in birefringent media was presented. In the next chapter the ray tracer that was written based around this method of ray tracing is used and its accuracy verified.

Chapter 6

Aberrations and birefringent lenses

Birefringent lenses are made from a birefringent material with its optic axis perpendicular to the optical axis of the system. Such lenses have two different focal lengths, f_o and f_e , associated with the o-ray and e-ray polarisation respectively. Figure 6.1 shows a birefringent lens and the two focal lengths.

If the e-ray experienced a refractive index that did not depend on propagation direction then ray-tracing optical systems incorporating lenses fabricated from birefringent material would be a simple matter. Existing software could

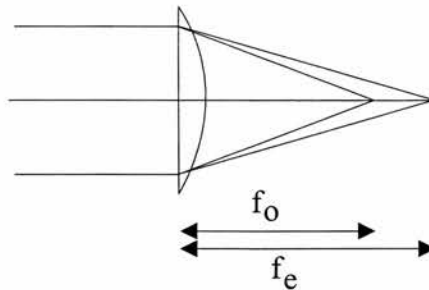


Figure 6.1: A calcite birefringent lens showing its two focal lengths.

be used with the refractive index data entered separately for both polarisations. However, the dependence of the refractive index upon propagation direction means that Snell's law is not valid for the e-ray polarisation and commercially available ray-tracing packages are not accurate for birefringent materials. The breakdown of Snell's law also means that the usual relationship between lens shape factor and aberrations is not valid for the e-ray polarisation.

Lenses made from birefringent materials have found a wide variety of uses ranging from common path profilometry systems [81, 82] compact disc readers[83], image processing[84] and even intra-ocular elements [85] and contact lenses[86].

In this chapter the dependence of the imaging aberrations and the corresponding point-spread-function on the shape factor of a birefringent lens is determined for the e-ray polarisation and it is shown that this differs from that of the o-ray.

6.1 Assessment of the accuracy of the ray-tracing package

To assess the performance of our ray-tracing software a simple two-lens telescope system was assembled. The identical plano-convex lenses were fabricated from calcite with focal lengths $f_o \approx 90mm$ and $f_e \approx 120mm$. The lenses were separated by approximately $f_o + f_e$ with their optic axes aligned perpendicularly to each other, thus forming an afocal telescope with approximate magnifications of f_o/f_e and f_e/f_o for horizontally and vertically polarised light respectively. A collimated laser beam, polarised at 45° to the vertical, is divided by the telescope into two, overlapping, orthogonally

polarised beams. By placing a polariser aligned at 45° at the exit aperture of the telescope the two beams interfere. The form of the fringes within the interferogram is a precise measure of the wavefronts associated with the two polarisations. The separation between the lenses was varied, and the resultant interferograms were recorded by a CCD array and compared with those predicted by our ray-tracing software.

Figure 6.2 shows a schematic of the telescope and figure 6.3 shows the calculated and the observed interferograms. The almost perfect agreement between experimental results and calculated interferograms demonstrates that our ray-tracing software is extremely accurate.

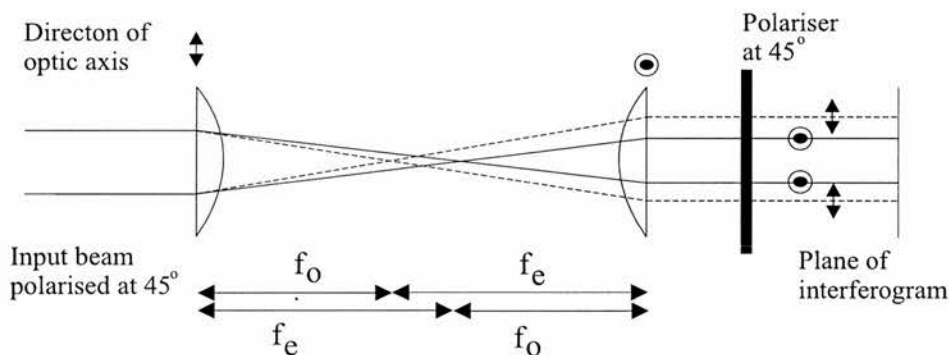


Figure 6.2: A birefringent telescope comprising two birefringent lenses with their optic axes perpendicular to each other.

6.2 Aberrations

Imperfections in the performance of a lens are usefully characterised in terms of the five Seidel aberrations; spherical aberration, coma, astigmatism, field flatness and distortion. These aberrations are frequently calculated geometrically from the distance between rays focused by different parts of the lens. A more general approach is to consider the shape of the wavefront after fo-

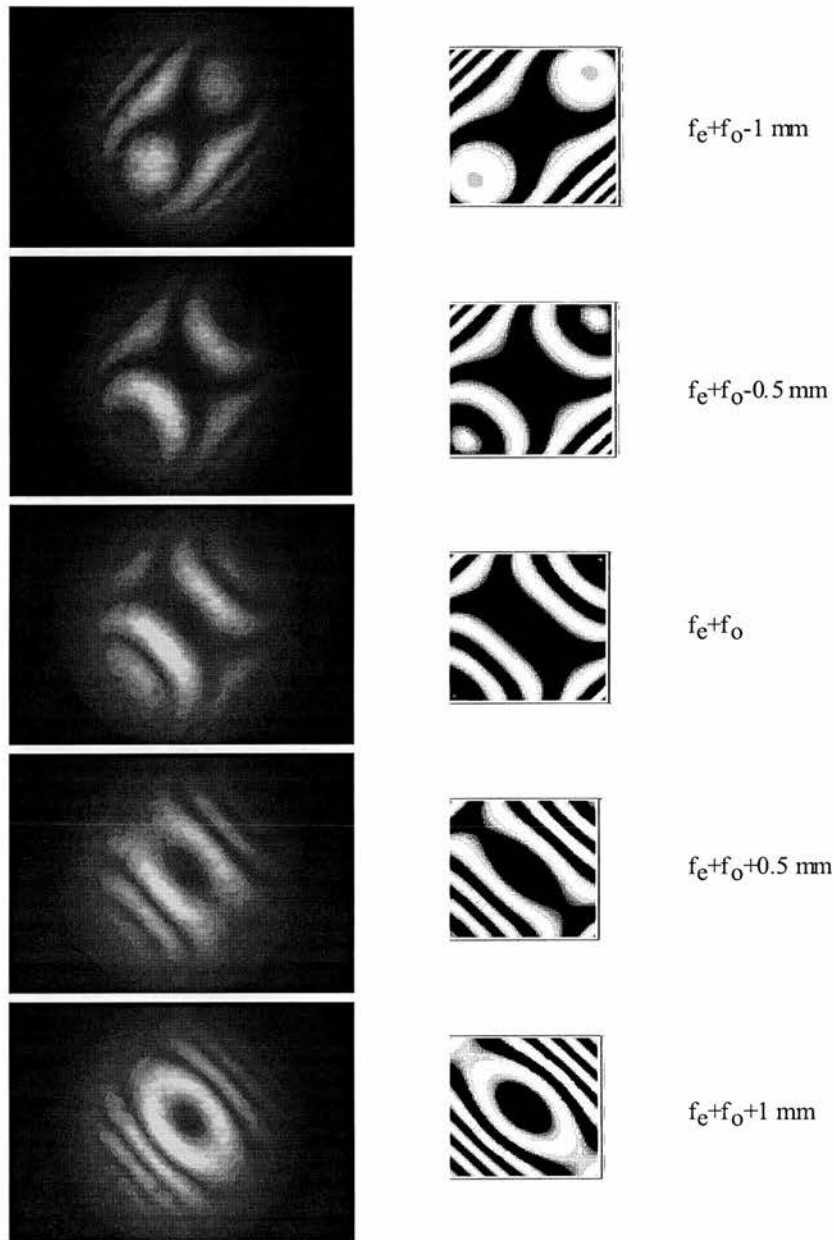


Figure 6.3: Interferograms and modelled results for various lens separations in a telescope comprising two birefringent lenses with perpendicular optic axes.

cusing by the lens. Any deviation away from a spherical surface represents an aberration.

6.2.1 Spherical Aberration

There are two types of spherical aberration - longitudinal and transverse. Longitudinal spherical aberration (LSA) is the distance between where the most extreme rays converge and the paraxial rays converge. Transverse spherical aberration (TSA) is defined as the distance between the points where the most extreme rays and the paraxial rays converge. Both LSA and TSA are illustrated in figure 6.4. Each is significant for different reasons. In imaging applications, it is important to minimise TSA, however for a tight focus along the beam LSA must be reduced. Since this work is primarily concerned with imaging, only TSA is of interest and hereafter TSA is simply referred to as spherical aberration.

The main way to reduce spherical aberration is to reduce the aperture, since spherical aberration varies with the square of the radius. However this limits the usable amount of light in the system.

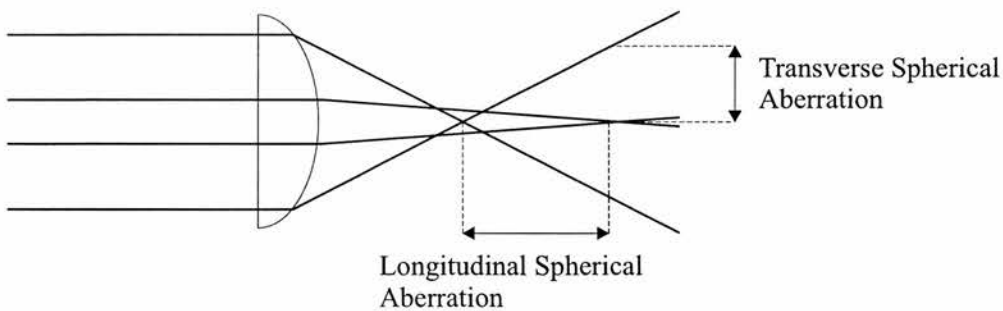


Figure 6.4: Output from ray tracer showing longitudinal and transverse spherical aberration

6.2.2 Coma

Coma is an aberration associated with off axis rays. Figure 6.5 shows a collimated bundle of axis rays being focussed by a lens. In the figure, h_c is the distance from the axis of the system to where a ray passing through the lens meets the focal plane, and h_e is the distance from the axis to where the extreme rays meet. A simple way to quantify coma is $h_c - h_e$ [70].

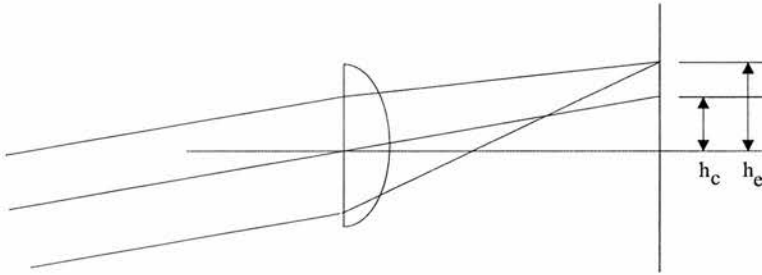


Figure 6.5: Figure showing how coma arises

6.2.3 Astigmatism

Astigmatism is an aberration that manifests itself as different focal lengths in the horizontal and vertical planes[87]. Astigmatism is an aberration not normally associated with an isotropic spherical lens because of the rotational symmetry of such a lens. However, the optic axis of a birefringent lens breaks this rotational symmetry and the e-ray polarisation is subject to astigmatism. Figure 6.6 shows how astigmatism arises in a birefringent lens.

6.2.4 Field Curvature

If a plane is being imaged by a lens as shown in figure 6.7 then the resultant image may not be flat. The actual image plane is a surface of the circles of least confusion and is known as the *Petzval surface*.

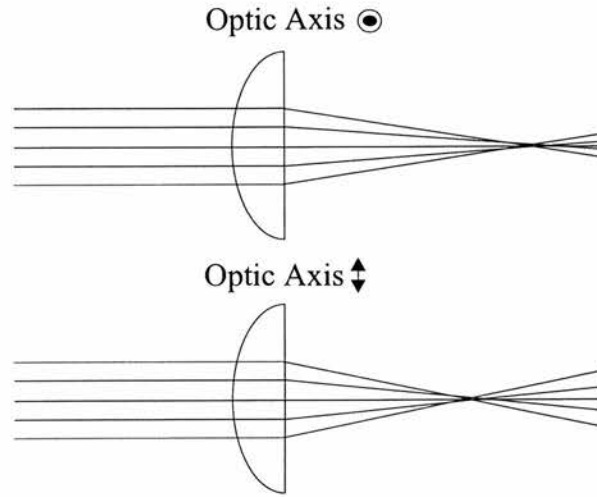


Figure 6.6: Astigmatism in a birefringent lens

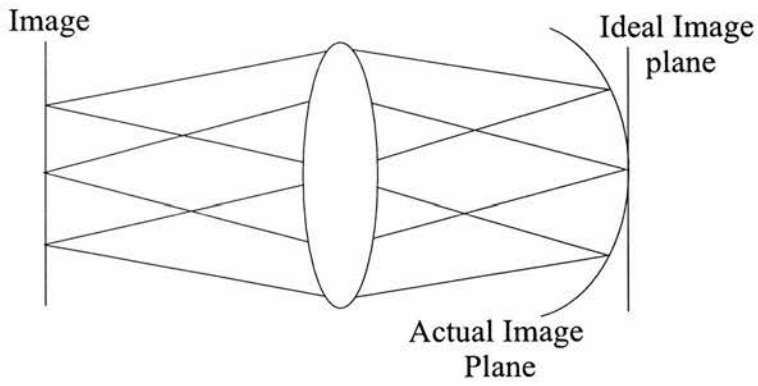


Figure 6.7: A lens imaging a plane and its field curvature

For a series of lenses field flatness can be calculated by

$$\sum \frac{1}{n_i f_i} = \frac{1}{R} \quad (6.1)$$

where n is the refractive index of the lens, f is the focal length and R is the radius of curvature of the resulting Petzval surface. Hence two lenses can ensure field flatness by satisfying the equation

$$n_1 \cdot f_1 + n_2 \cdot f_2 = 0 \quad (6.2)$$

where n_1 and n_2 are the refractive indices of the lenses and f_1 and f_2 are the focal lengths of the two lenses respectively.

6.2.5 Distortion

Distortion is an imaging aberration that arises due to a variation in the lateral magnification for object points at different distance points from the optical axis[88]. There are two types of distortion - pin cushion (when the magnification increases with distance from the axis) and barrel (when the magnification decreases with distance from the optical axis). Figure 6.8 shows the different kinds of distortion.

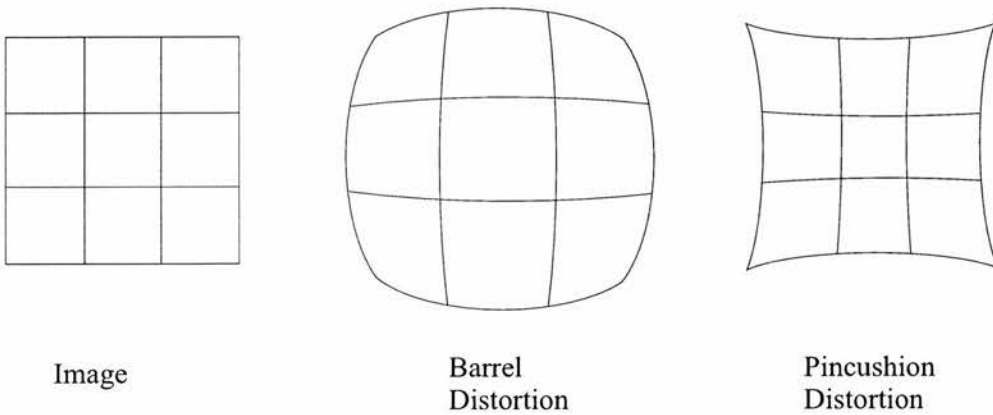


Figure 6.8: Various kinds of distortion

6.3 Bending lenses to reduce aberrations

The relative magnitude of the various aberrations depends critically upon the shape of the lens and the object and image positions described conveniently by the conjugate ratio. The shape of a lens is described by the shape

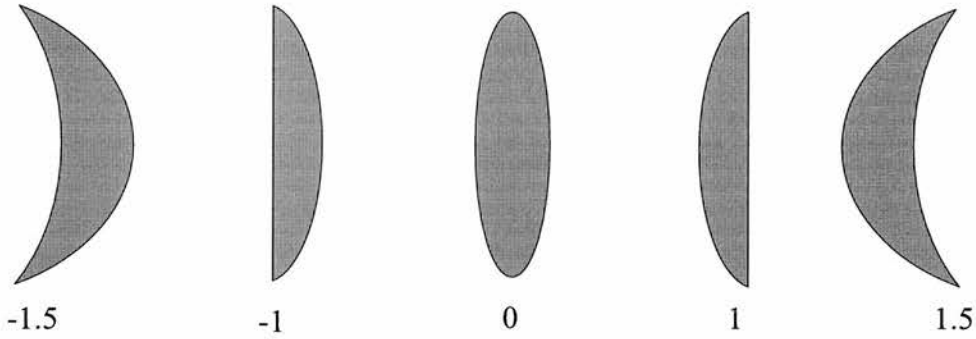


Figure 6.9: A variety of lenses and their corresponding SFs.

factor, SF ,

$$SF = \frac{r_f + r_b}{r_f - r_b} \quad (6.3)$$

where r_f and r_b are the radii of curvature of the front and back faces of the lens respectively. Figure 6.9 shows a variety lenses and their corresponding SF.

The conjugate ratio, C , is defined as

$$C = \frac{i - o}{i + o} \quad (6.4)$$

where i and o are the image and object distances respectively. If $C = 0$ then the image and object distances are equal, if $C = -1$ then the object is at infinity and if $C = 1$ then the object is at the principal focus of the lens.

For lenses fabricated from isotropic materials, where Snell's law is valid, the dependence of the various aberrations upon the shape factor of the lens is well known [89, 70]. For lenses made from birefringent materials the o-rays obey the same relationship but the e-rays behave differently. Hence the shape factor that gives the minimum aberration for the o-ray polarisation does not necessarily give the minimum aberration for the e-ray polarisation

6.4 Wavefront Analysis

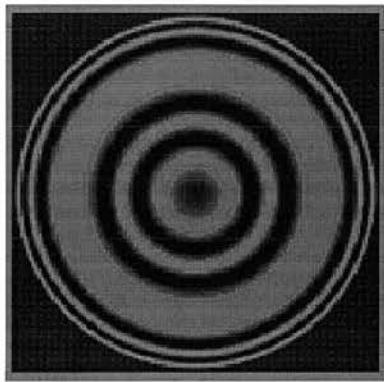
After focusing by the lens the shape of the wavefront should ideally be spherical and the deviation from a spherical wavefront can be represented by the wave-front aberration function[89]

$$\Delta W = A(x^2 + y^2)^2 + By(x^2 + y^2) + C(x^2 + 3y^2) + D(x^2 + y^2) + Ey + Fx \quad (6.5)$$

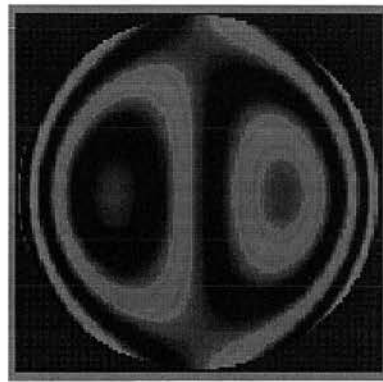
where the coefficient A represents the amount of spherical aberration, B the coma, C the astigmatism, D the amount of de-focus, E and F represent tilts about the y and x -axes respectively. Consequently this equation contains three of the five Seidel aberrations. The other two aberrations, namely field flatness and distortion only apply when a lens is used as part of a larger imaging system and refer to curvature of the best image plane and variation in lateral magnification respectively. Optical systems for which field flatness and distortion are relevant usually comprise multiple optical components. Although our ray tracing software can model any system of lenses in this work we restrict ourselves to the consideration of single lenses and therefore do not deal with either of these aberrations in any detail.

To illustrate the various wavefront shapes corresponding to the terms of equation 6.5 figure 6.10 shows the interferograms resulting from the various aberrations.

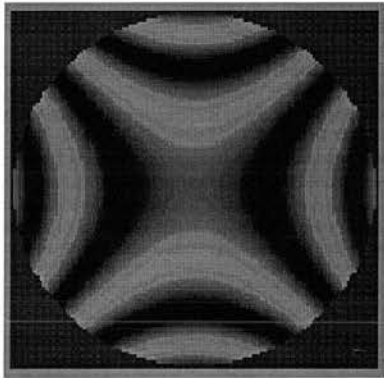
We use the birefringent ray tracing software described in this work to calculate the spherical aberration, coma and astigmatism associated with various designs of birefringent lenses, *i.e* the co-efficients A , B and C in equation 6.5.



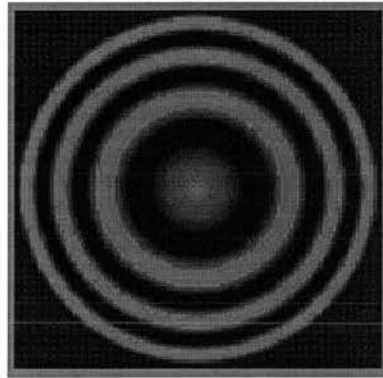
Spherical aberration (A)



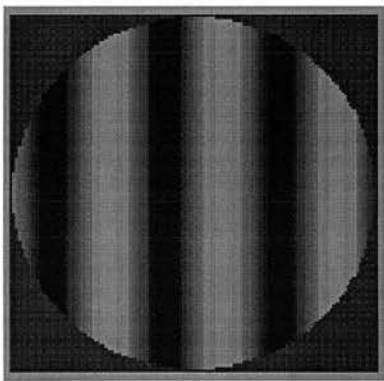
Coma (B)



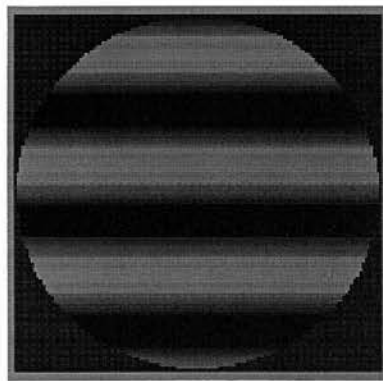
Astigmatism (C)



Defocus (D)



x-tilt (E)



y-tilt (F)

Figure 6.10: Interferograms arising from interference of a plane wave and aberrated wavefront.

n	l	Z_n^l	Aberration
1	1	$r.Sin(\theta)$	y-Tilt
1	-1	$r.Cos(\theta)$	x-tilt
2	2	$r^2.Sin(2\theta)$	Astigmatism at 45°
2	0	$2r^2 - 1$	Defocus
2	-2	$r^2.Cos(2\theta)$	Astigmatism at 45°
3	3	$r^3.Sin(3\theta)$	Trifoil at 30°
3	1	$(3r^3 - 2r).Sin(\theta)$	Coma along y axis
3	-1	$(3r^3 - 2r).Cos(\theta)$	Coma along x axis
3	-3	$r^3.Cos(3\theta)$	Trifoil 0°
4	4	$r^4.Sin(4\theta)$	Tetra-foil at 22.5°
4	2	$(4r^3 - 3r^2).Sin(2\theta)$	2nd order Astigmatism at 45°
4	0	$6r^4 - 2r^2 - 1$	Spherical aberration
4	-2	$(4r^4 - 3r^2).Cos(2\theta)$	2nd order Astigmatism at 0°
4	-4	$r^4.Cos(4\theta)$	Tetra-foil at 0°

Table 6.1: Zernike Polynomials up to 4th order and corresponding aberrations

6.4.1 Zernike Polynomials

Another equivalent form of wavefront decomposition is based around a class of polynomials called *Zernike polynomials*. Zernike polynomials [15] describe a complete basis set for decomposing shapes on a unit circle. Zernike polynomials are defined by the equation

$$Z_n^l(r, \theta) = e^{il\theta} \sum_{s=0}^{\frac{n-l}{2}} (-1)^s \frac{(n-s)!}{s!(\frac{n+l}{2}-s)!(\frac{n-l}{2}-s)!} r^{n-2s} \quad (6.6)$$

The Zernike polynomials up to fourth order and their respective aberrations are shown in table 6.1.

6.5 Calculations of aberrations introduced by a birefringent lens

Spherical aberration, coma and astigmatism can all be usefully calculated for a single lens working at infinite conjugates. Spherical aberration arises from the approximation of the ideal lens surface to a sphere and results in the off-axis rays experiencing a different focal power. From third order aberration theory it can be shown that spherical aberration in an isotropic lens, and hence for the o-ray in a birefringent lens is minimised by setting the shape factor [88] to

$$SF = -\frac{2(n_o^2 - 1)}{n_o + 2}C. \quad (6.7)$$

Our ray tracer was used to calculate the shape of the wavefronts for both polarisations after focusing by a birefringent lens. These wavefronts were then fitted to the wavefront aberration function to determine the best fit coefficients and the corresponding aberrations. All calculation were done at $f_o/8$ for a lens with $f_o \approx 90mm$ and $f_e \approx 120mm$.

Figure 6.11 shows the modelled spherical aberration for both the o-ray and e-ray polarisations in a birefringent lens as a function of shape factor. Note that the optimum shape factor to minimise the spherical aberration for the e-ray polarisation differs slightly from that of the o-ray polarisation.

Coma is an image degrading aberration that results from different zones of a lens having different lateral magnification. In an isotropic lens coma may be completely eliminated by setting the shape factor

$$SF = -\frac{2n_o^2 - n_o - 1}{n_o + 1}C. \quad (6.8)$$

Figure 6.12 shows the modelled coma for both the o-ray and e-ray polar-

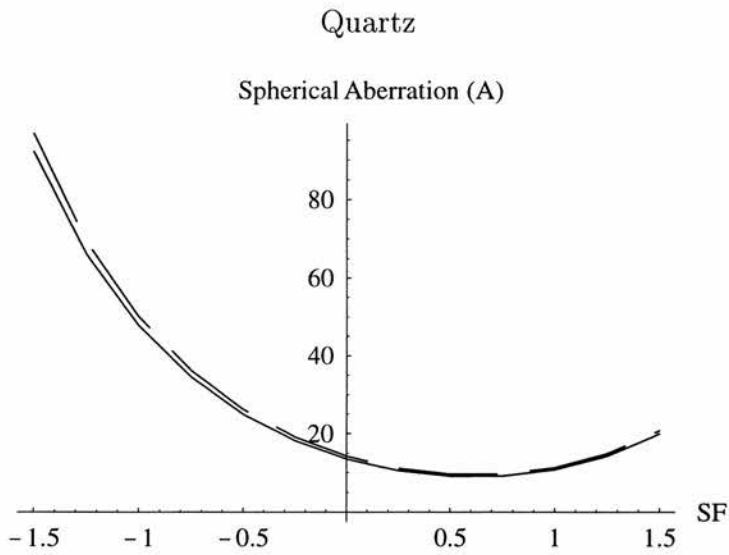
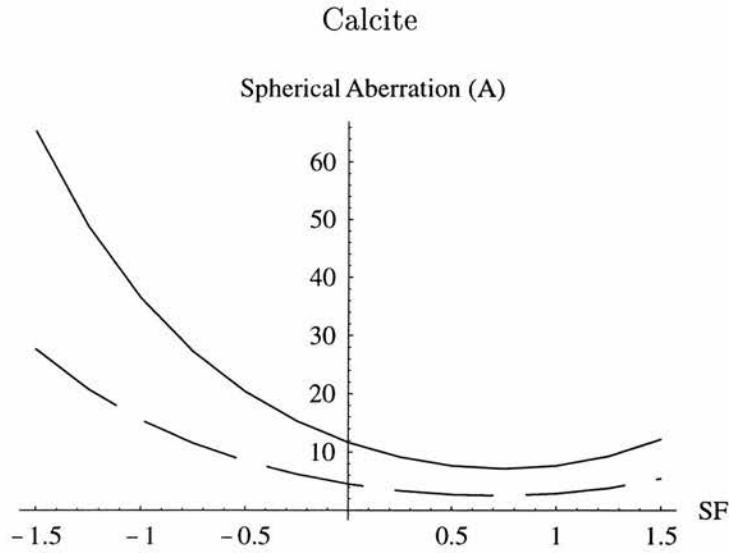


Figure 6.11: Graphs showing how spherical aberration of a birefringent lens varies with shape factor (SF) for the o-ray (solid line) and the e-ray (dashed line).

isations in a birefringent lens as a function of shape factor. Again it is seen that the optimum shape factor for the o-ray and e-ray is slightly different.

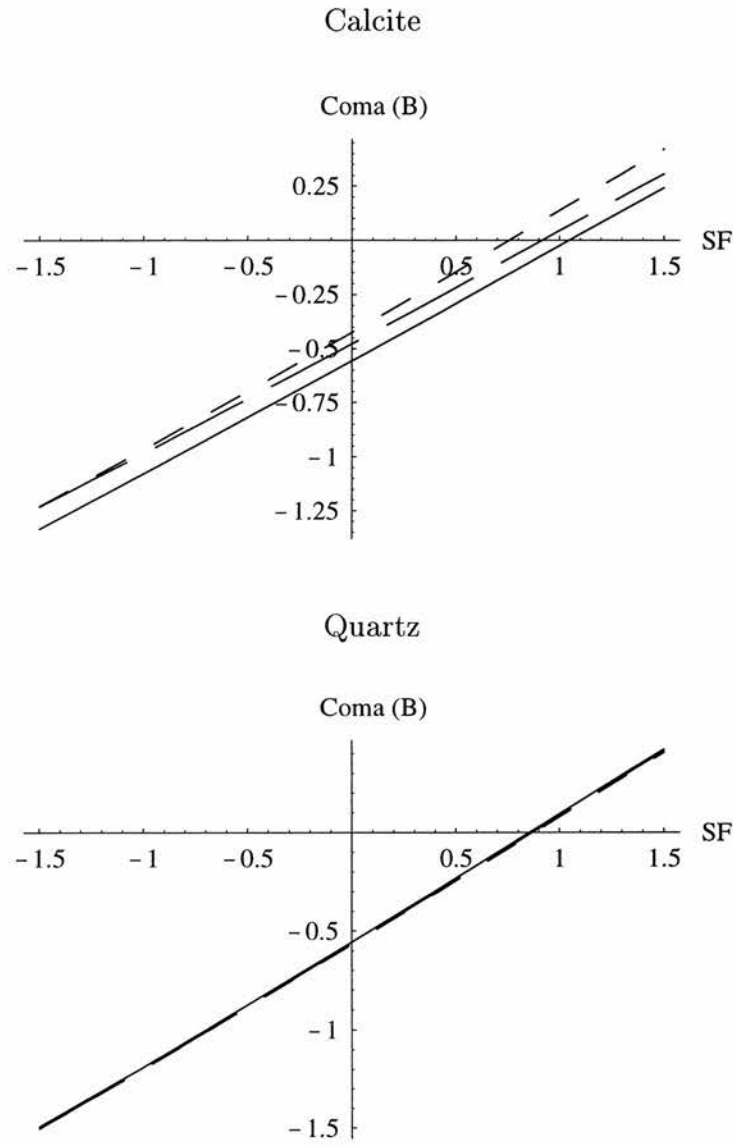


Figure 6.12: Graphs showing how coma varies in birefringent calcite and quartz lenses as a function of shape factor (SF). The solid line shows how coma varies for the o-ray. The two dashed lines show how coma varies for the e-ray when the incident ray bundle is parallel to the optic axis (short dashes) and perpendicular to the optic axis (long dashes).

Figure 6.13 shows the astigmatism for the e-ray polarisation in a birefringent lens as a function of shape factor and thickness. Note that the astigmatism increases in proportion to the thickness of the lens, as previously predicted[90], and in practice is much greater than the other aberrations. The e-ray astigmatism is minimised by selecting the shape factor of the lens that ensures the ray direction is perpendicular to the optic axis of the crystal. In general this shape factor is significantly different from that for the minimisation of spherical aberration and coma.

6.6 Combined aberrations

The separation of imaging imperfections into the Seidel aberrations, although a useful aid to design, is sometimes difficult to visualize in terms of the overall lens performance. It is often more intuitive to consider the point spread function or its geometrical equivalent the geometrical spot diagram (GSD) of the complete optical system.

As a representative example the GSD of a single birefringent lens when used at infinite conjugates was considered. Figures 6.14 to 6.18 show the GSDs for collimated bundles of on-axis and off-axis rays with incident angles of 0, 2.5 and 5 degrees. The GSDs are shown either side of the circle of least confusion for the on-axis rays using birefringent lenses of various shape factors fabricated from calcite. Note that in this case the diffraction limit corresponds to a GSD with a diameter of approximately $8\mu m$. The two field angles α and β are used to refer to the planes perpendicular and coplanar with the optic axis of the lens respectively. For the o-ray the lens is rotationally symmetric and so the GSD for variations in α or β are identical. However, for the e-ray the optic axis breaks the rotational symmetry and so

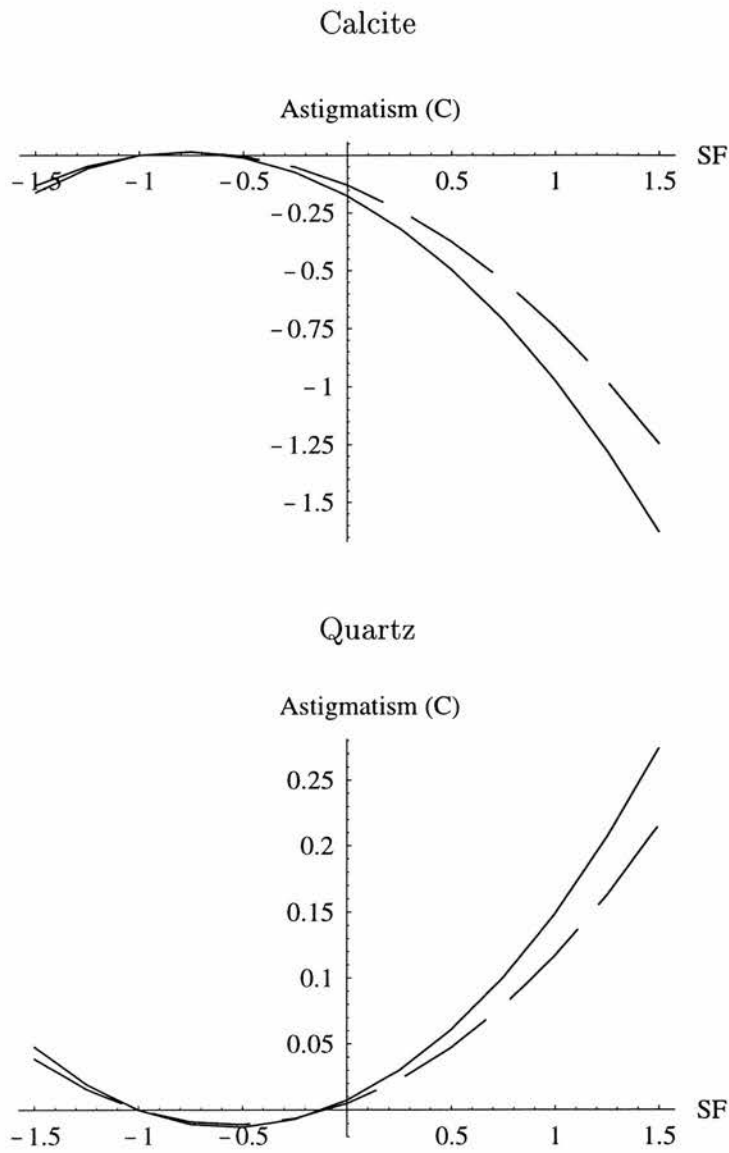


Figure 6.13: Graphs showing how astigmatism varies with shape factor (SF) for the e-ray in a birefringent lens. The solid lines are for a lens of thickness 0.5cm and the dashed lines for a lens of thickness 0.4cm

the GSD for both α and β need to be considered separately.

In general, the shape-factor that minimises the point-spread function for

the o-ray polarisation is not the optimum shape factor for the e-ray polarisation. A choice has to be made between minimising the astigmatism for the e-ray polarisation or minimising the impact of spherical aberration and coma.

6.7 Conclusions

With respect to both spherical aberration and coma the optimum shape factor for the e-ray polarisation differs slightly from the o-ray. However, for the e-ray polarisation both of these aberrations are dominated by astigmatism. The e-ray astigmatism arises from the breaking of rotational symmetry within the birefringent material. However if a lens of $SF = -1$ is used then the astigmatism is completely eliminated.

In general this additional aberration for the e-ray polarisation means that the corresponding point-spread function is always more aberrated than for the o-ray polarisation. Consequently, in a multi-focal optical system, the critical focus should be based on the o-ray polarisation. If both foci are important then the shape factor for the birefringent lens needs to be selected as a compromise between the optimum shape factors for the o-ray and e-ray polarisations. Finally, it is important to emphasise that the computer package we have developed in this work and applied to a one and two birefringent lens system, is quite general and can be applied to arbitrarily complex systems incorporating both isotropic and birefringent lens. This chapter is based upon a paper due for publication in Applied Optics.

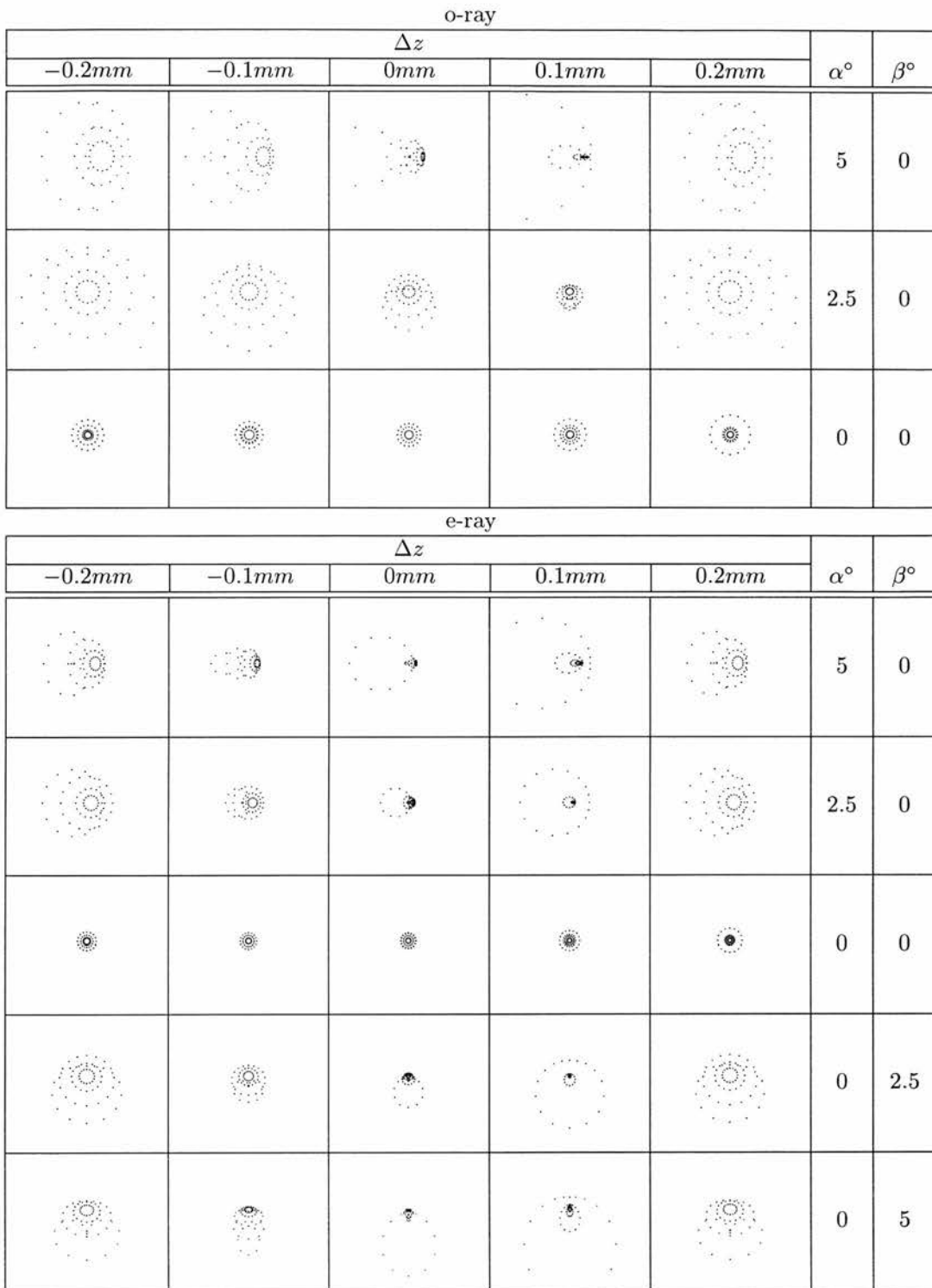


Figure 6.14: The geometrical spot diagrams for Calcite lens with shape factor $(SF) = -1$ and focal lengths $f_o \approx 90mm$ and $f_e \approx 120mm$ at $f/8$. All spot diagrams are contained in squares of dimensions $100\mu m$ by $100\mu m$. Δz represents the distance away from the circle of least confusion.

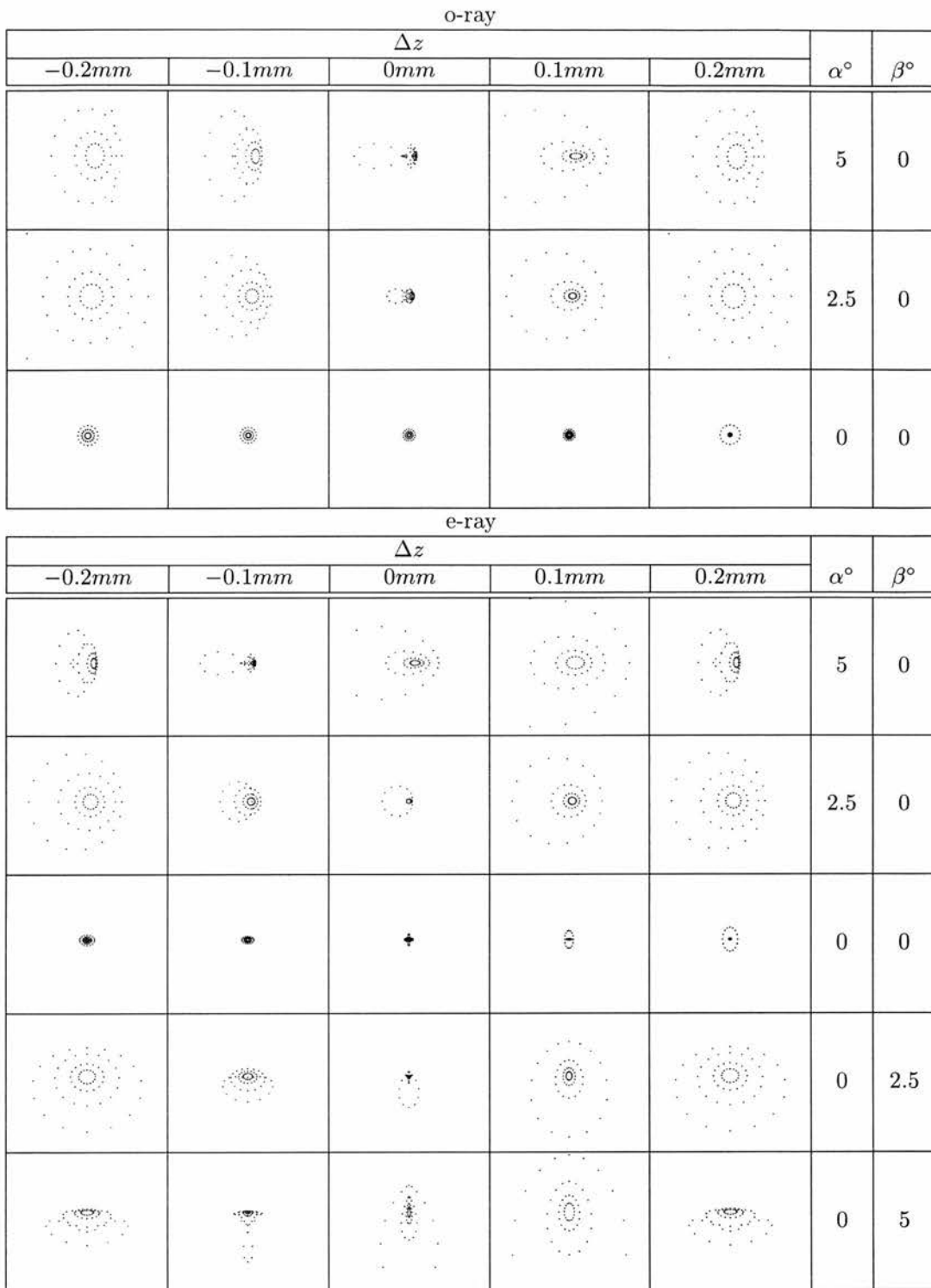


Figure 6.15: The geometrical spot diagrams for Calcite lens with shape factor $(SF) = -0.5$ and focal lengths $f_o \approx 90mm$ and $f_e \approx 120mm$ at $f/8$. All spot diagrams are contained in squares of dimensions $100\mu m$ by $100\mu m$. Δz represents the distance away from the circle of least confusion.

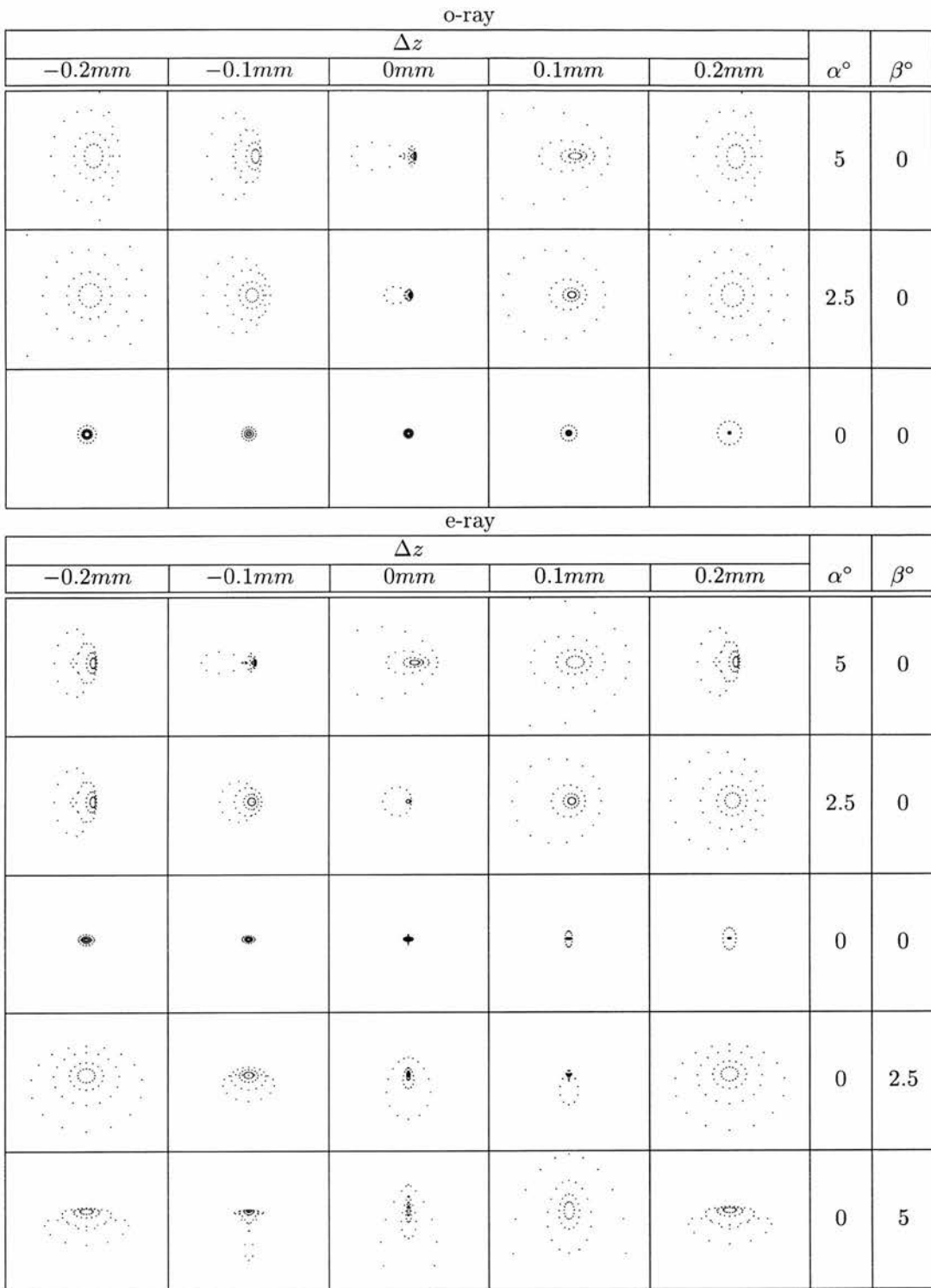


Figure 6.16: The geometrical spot diagrams for Calcite lens with shape factor (SF) = 0 and focal lengths $f_o \approx 90mm$ and $f_e \approx 120mm$ at $f/8$. All spot diagrams are contained in squares of dimensions $100\mu m$ by $100\mu m$. Δz represents the distance away from the circle of least confusion.

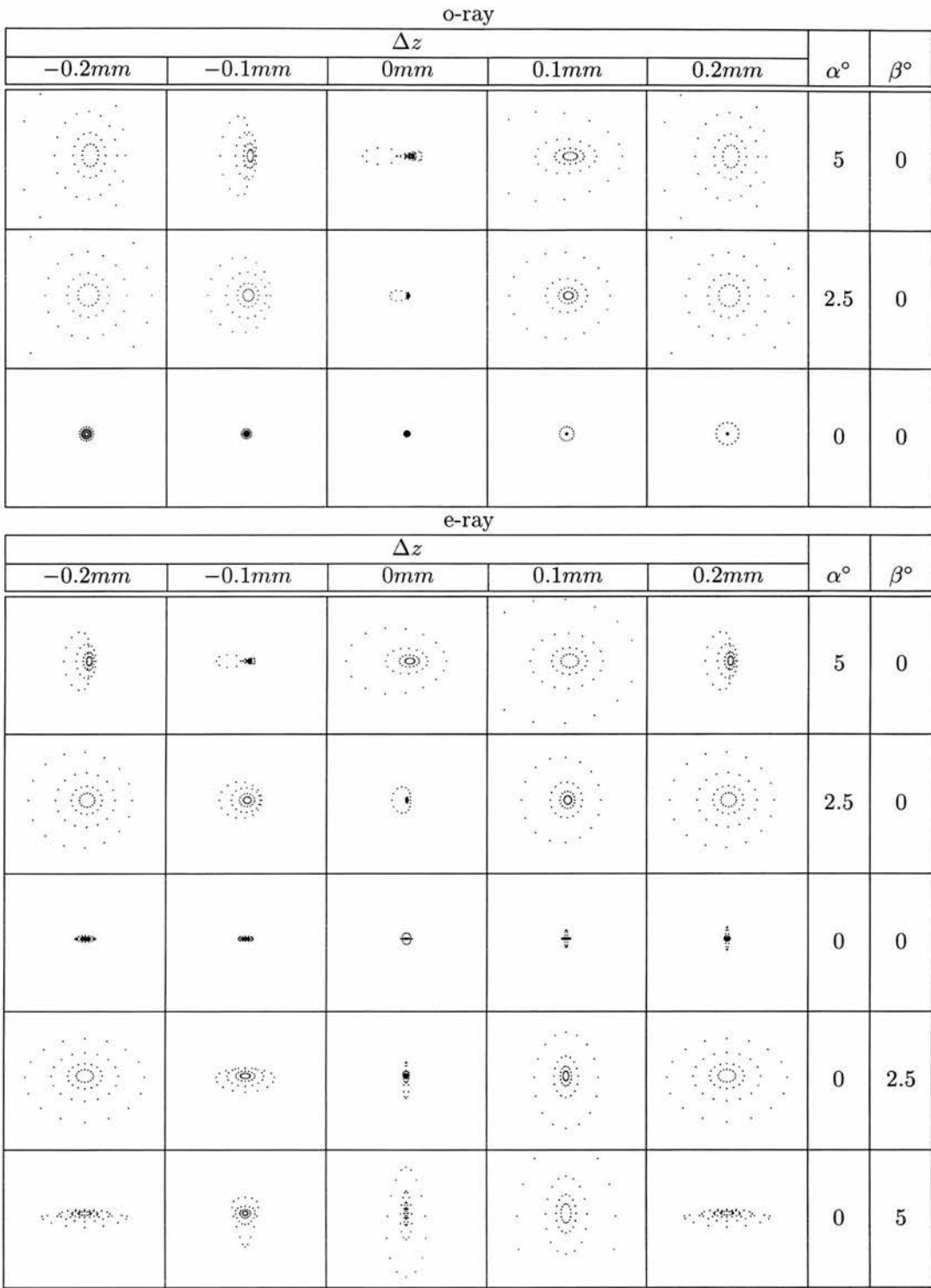


Figure 6.17: The geometrical spot diagrams for Calcite lens with shape factor $(SF) = 0.5$ and focal lengths $f_o \approx 90mm$ and $f_e \approx 120mm$ at $f/8$. All spot diagrams are contained in squares of dimensions $100\mu m$ by $100\mu m$. Δz represents the distance away from the circle of least confusion.

o-ray					α°	β°
Δz						
$-0.2mm$	$-0.1mm$	$0mm$	$0.1mm$	$0.2mm$		
					5	0
					2.5	0
					0	0

e-ray					α°	β°
Δz						
$-0.2mm$	$-0.1mm$	$0mm$	$0.1mm$	$0.2mm$		
					5	0
					2.5	0
					0	0
					0	2.5
					0	5

Figure 6.18: The geometrical spot diagrams for Calcite lens with shape factor $(SF) = 1$ and focal lengths $f_o \approx 90mm$ and $f_e \approx 120mm$ at $f/8$. All spot diagrams are contained in squares of dimensions $100\mu m$ by $100\mu m$. Δz represents the distance away from the circle of least confusion.

Chapter 7

Compensated shearing interferometry

As discussed in previous chapters shearing interferometry is a common-path interferometric technique, which uses two different regions of a surface for the reference and object. It is widely used in demanding environments where both interferometric accuracy and stability are required[15, 16, 17].

This chapter presents a novel method for measuring imperfections on a regularly corrugated surface. Of particular interest is detecting defects on surfaces such as a hard disc or a motor bearing. In addition to the corrugated surface structure these surfaces present another challenge - low reflectivity.

7.1 Regular surface structure

A simple way to detect defects on a flat surface is to interfere light reflected from the sample with a uniform flat reference beam. If the interferometer is biased into dark field then the defects show up in the interferograms as bright regions. However for a surface with corrugated structure, the corrugated stu-

structure shows up as bright regions as well. Image processing techniques can be used in conjunction with a computer to remove regular surface structure and examine the defects within the structure[91]. However if the processing is done optically then no computer is required and the processing is done real time[92]. Using a shearing interferometer is it possible to remove corrugated surface structure by arranging the shear so that it lies along the direction of the corrugated structure. Figure 7.1 shows how shearing interferometry can be used to do this.

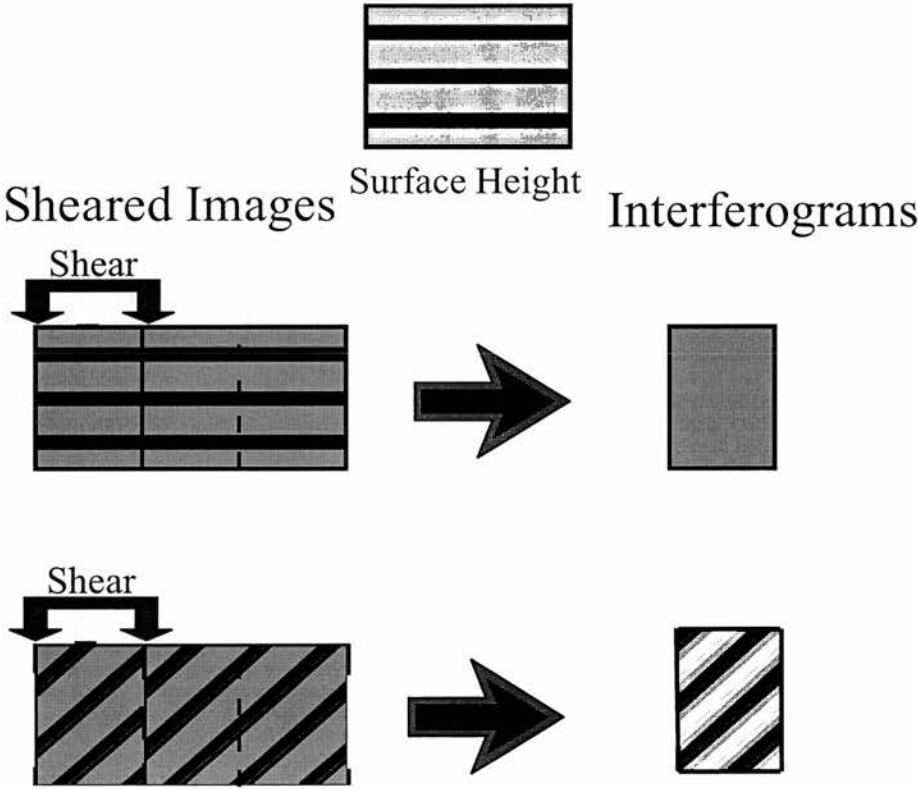


Figure 7.1: Illustration of how shearing interferometry can be used to remove surface structure.

7.2 Low Reflectivity

When examining surfaces with low reflectivity, unwanted reflections in the system can effectively swamp the light from the object - resulting in reduced fringe contrast within the interferogram. Even when anti-reflection coatings are used 0.2% of the illumination light can be reflected back[54]. Therefore the shearing interferometer described in chapter 2 cannot be used.

To avoid unwanted light reflecting in the system the illumination and imaging arms of the interferometer are separated as shown in figure 7.2. Whilst there is a slight loss of stability due to the separation of the interferometer arms, in practice the effects can be minimised and the system can be used to examine objects with a very low reflectivity.

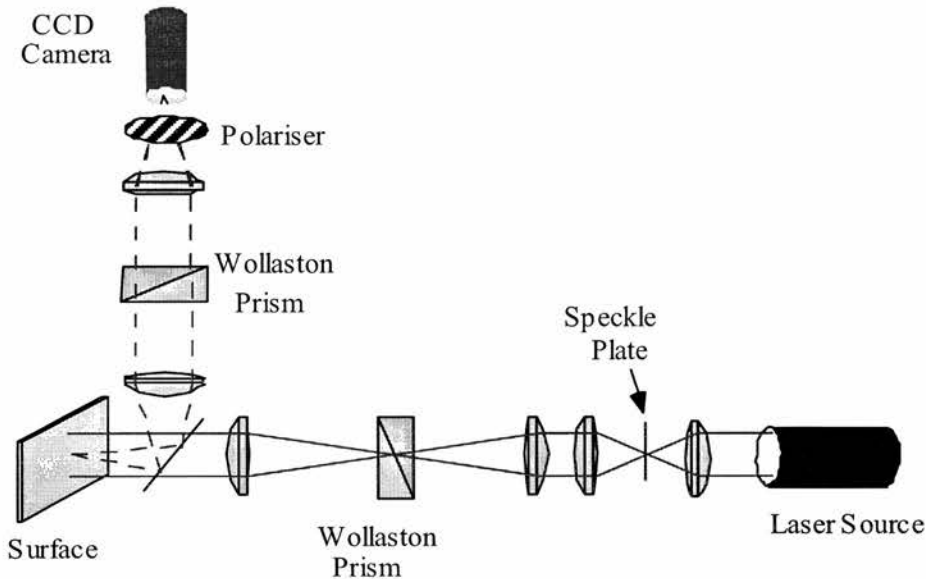


Figure 7.2: A shearing interferometer with its illumination and imaging arms separated

The high intensity that lasers can provide make them ideal for illuminating surfaces with a low reflectivity, but the high spatial coherence of the

beam leads to regular pattern or ‘speckle’ in the image[93]. It is well known that speckle can be removed from interferometric images, by destroying the spatial coherence of the illuminating laser beam. This can be done by passing the laser light thorough a spinning ground glass disc. Whilst this removes the speckle, it also creates problems obtaining high contrast interferograms.

7.3 Spatially coherent light sources

Using a spatially coherent source only one Wollaston prism would be needed in the illumination arm to shear the images onto the camera. The maximum distance the images could be sheared and still give high contrast interferograms depends upon the spatial coherence of the source. The spatial coherence of the source gives rise to an effective transverse coherence length. In the plane of the images the transverse coherence length a distance R from a source of width Δs and mean wavelength $\bar{\lambda}$ is given by[52]

$$l_{tc} = 2R \tan\left(\frac{\bar{\lambda}}{\Delta s} \frac{1}{2}\right) \quad (7.1)$$

Thus the transverse coherence length increases as the wave length increases and increases as the source width decreases. An alternative to using a small pinhole is to introduce a shear in the illumination arm which matches the shear in the imaging arm, *i.e.* the imaging arm brings the sheared light back to a single point. This design is referred to as a compensated shearing interferometer.

7.4 Illumination Optics

Figure 7.3 shows the illumination arm of the interferometer. A lens focuses the light onto a Wollaston prism, which splits the light into two orthogonally

polarised beams, which are collimated by the final lens.

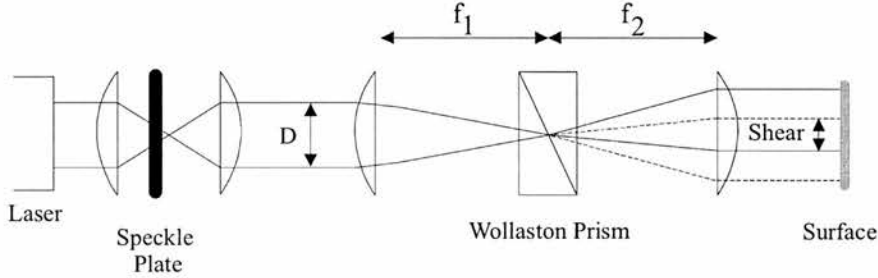


Figure 7.3: Illumination arm of interferometer

The two beams are sheared by a distance Δ_{shear1} , which is given by

$$\Delta_{shear1} = f_2 \alpha_1 \quad (7.2)$$

where α_1 is the splitting angle of the Wollaston given by

$$\alpha_1 = 2(n_e - n_o)\tan(\theta) \quad (7.3)$$

where θ is the angle internal to the Wollaston prism, and n_o and n_e are the ordinary and extra-ordinary refractive indices respectively. In order to ensure that the phase fronts of the collimated beams emerging from the Wollaston are uniform the incident angle of light must be within the field of view (FOV) of the Wollaston prism. The FOV of a Wollaston prism is approximately[17] given by

$$i_{max}^2 = \frac{\phi}{W} \frac{2n_o^2 n_e^2}{n_e^2 - n_o^2} \quad (7.4)$$

where ϕ is the maximum allowable phase variation across the beam and W is the thickness of the Wollaston prism. For a calcite Wollaston 5mm thick at $\lambda = 633nm$ allowing a $\lambda/10$ phase variation equation 7.4 gives $i_{max} = 0.76^\circ$. Figure 7.4 shows the phase difference between orthogonal polarisations emerging from Wollaston prism as a function of input angle, calculated using

the ray tracing package described in earlier chapters. The field of view is indicated by the small circle on the figure. As can be seen equation 7.4 gives a very good estimate of the FOV.

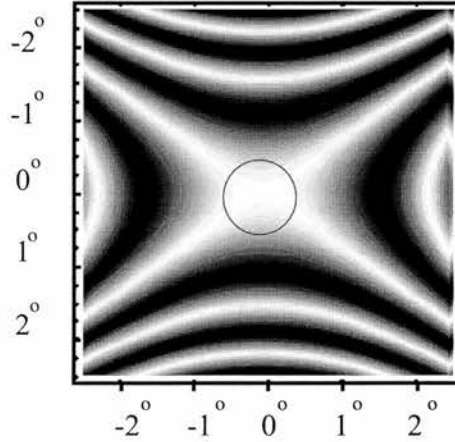


Figure 7.4: Field of view of a calcite Wollaston prism 5mm thick for $\lambda = 633\text{nm}$.

In practical terms equation 7.4 limits the maximum diameter of the beam to

$$D = 2f_1 \tan(i_{max}) \quad (7.5)$$

where D is the diameter of the beam as shown in figure 7.3.

7.5 Imaging optics

As discussed above in order to maintain fringe contrast the shear introduced by the illumination arm must match that introduced by the imaging arm. Figure 7.5 shows the imaging arm of the interferometer. The optics bring the two beams together such that they interfere on the camera. The images are sheared by a distance Δ_{shear2} , given by

$$\Delta_{shear2} = f_3 \cdot \alpha_2 \quad (7.6)$$

It must also be noted that the magnification m of the imaging optics is given by

$$m = \frac{f_4}{f_3} \quad (7.7)$$

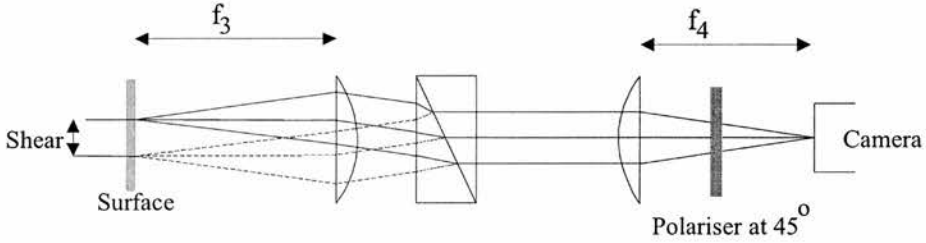


Figure 7.5: Imaging arm of interferometer

The condition for maximum fringe visibility is that the shear introduced by the illumination optics must match that of the imaging optics, *i.e.*

$$\Delta_{shear1} = \Delta_{shear2} \quad (7.8)$$

However an exact match depends on the component tolerances and what is important that difference between the shears is less than the transverse coherence length of the source, *i.e.*

$$|\Delta_{shear1} - \Delta_{shear2}| < l_{tc} \quad (7.9)$$

7.6 Experimental Results

A schematic of the interferometer used is shown in figure 7.6. The Wollastons result in a shear distance of approximately $131\mu m$. Figure 7.7 shows two interferograms from a surface with a regularly corrugated structure. The interferograms are $1mm$ by $0.6mm$.

The top interferogram shows both the surface defect and the regular surface texture (the grooves are aligned at 30° to the horizontal). However in the

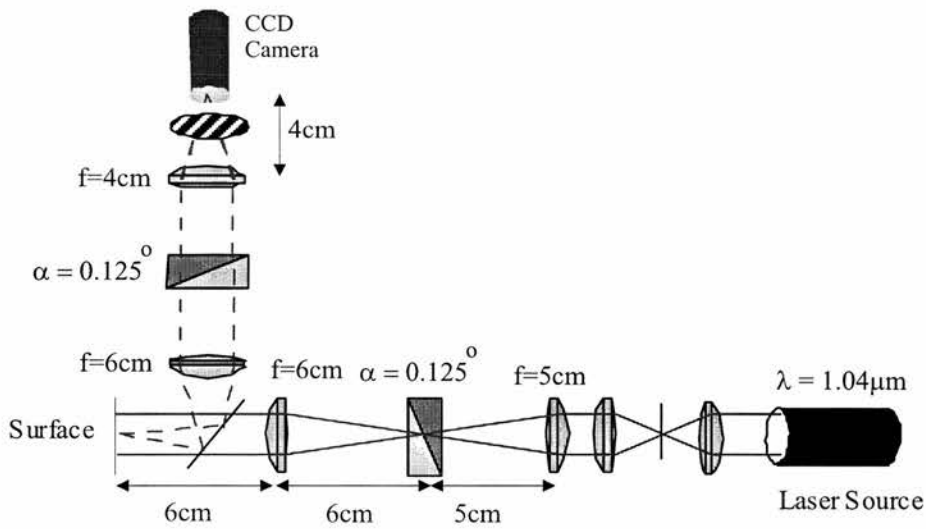


Figure 7.6: Detailed layout of compensated shearing interferometer.

lower interferogram, the grooves lie along the direction of shear and hence only the defects within the texture are seen. By use of suitable optics, such as a Dove prism (see Chapter 8), the direction along which the shear takes place can be changed hence allowing the regular surface texture to be ‘switched’ on and off. Usefully a Dove prism can be used to rotate the shear but not the polarisation, and it is interesting to compare this to a wave plate which rotates the polarisation but not the shear.

7.7 Conclusions

An alternative design of shearing interferometer has been presented which uses two Wollaston prisms, ideally suited to use with objects with low reflectivity and regular corrugated structure. By judicious choice of lenses and Wollaston prisms our system can obtain an arbitrary shear distance, overcoming the limits imposed by the transverse coherence length of the illumination beam. This chapter is based upon work both presented at CLEO ’99.

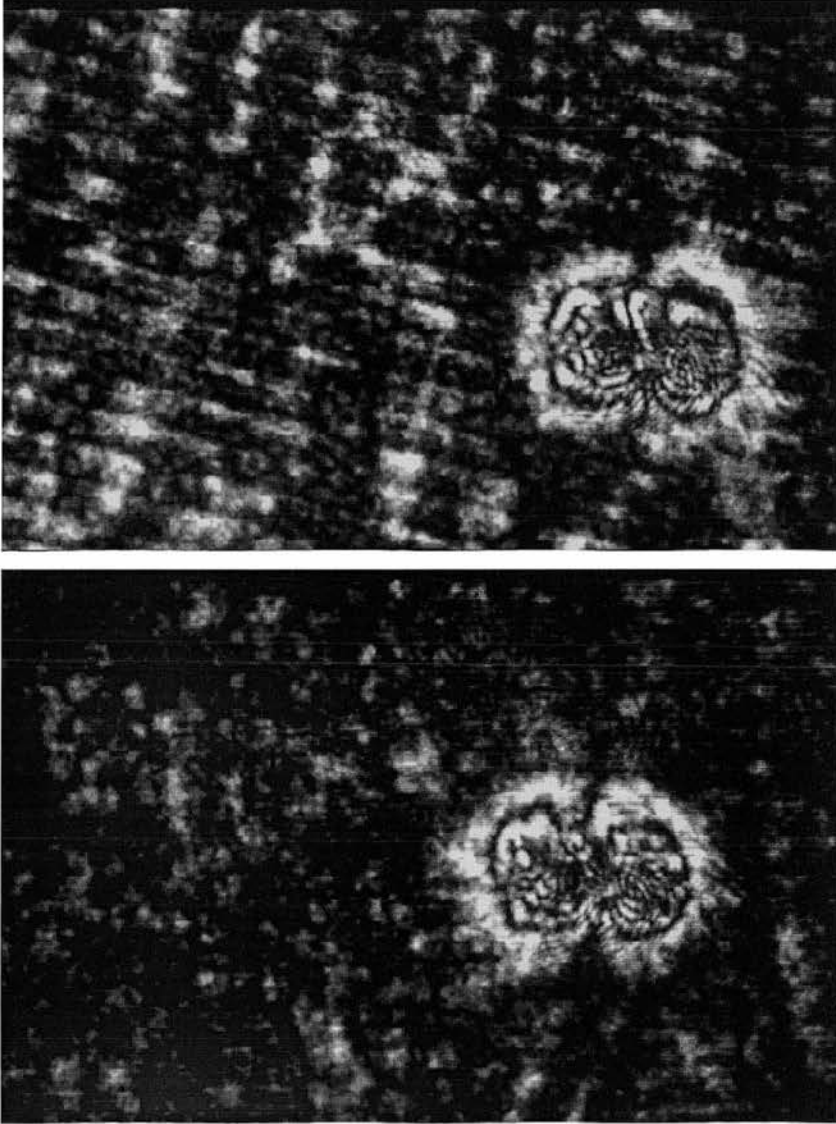


Figure 7.7: Experimental results showing the effect of using shearing interferometry to remove regular surface structure.

Chapter 8

Dove prisms and polarised light

This chapter is based upon a paper published in the Journal of Modern Optics, Vol. 46, No. 2, 1999

A Dove prism is usually formed from a truncated right angle prism[72] with a corresponding base angle, α , of 45° . After transmission through the prism, an incident ray parallel to the base undergoes no angular deviation but the total internal reflection from the base of the prism inverts the image, as shown in figure 8.1.

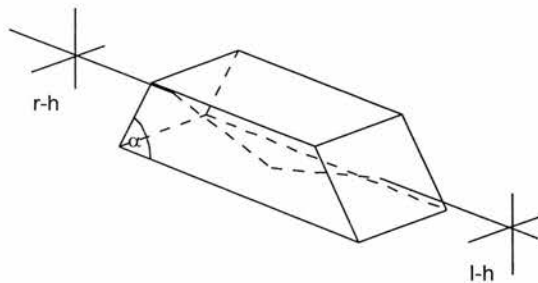


Figure 8.1: A Dove prism acting as an image inverter

As with other image inverters, if a Dove prism is rotated at a frequency

Ω a transmitted image rotates at 2Ω . This is analogous to a half-wave plate which when rotating at frequency Ω rotates the polarisation state of the transmitted light at 2Ω [94]. The inverting properties of a Dove prism mean that it is used frequently as an image rotator within optical viewfinders such as periscopes[48]. Dove prisms have also been used within interferometers to rotate one beam with respect to the other[95, 96]. In some solid-state laser systems, the active gain medium is shaped as a Dove prism within which the total internal reflection allows efficient coupling of the emission from a laser diode bar. Most recently, an acousto-optic equivalent of a Dove prism that gives none-mechanical image rotation has been reported[97]. Our current interest in Dove prisms arose from their use as a beam rotator within an experiment for observing the rotational frequency shift[98]. In this chapter, the effect of a Dove prism on the polarisation state of the transmitted light is considered and modified designs suggested.

8.1 Dove prism design

The choice of aperture, base angle and material govern the specific design of Dove prism. For a given aperture, the length of the prism needs to be such that after refraction at the input face, the central ray is reflected from the base and exits the centre of the exit face. The formula for the ratio between the length and aperture of the prism is given by[99]

$$\frac{Length}{Aperture} = \frac{1}{Sin(2\alpha)} \left(1 + \frac{\sqrt{n^2 - Cos^2(\alpha)} + Sin(\alpha)}{\sqrt{n^2 - Cos^2(\alpha)} - Sin(\alpha)} \right) \quad (8.1)$$

For a glass with a refractive index of 1.517, the optimum base angle giving a prism with shortest overall length is approximately 32.5° .

One might expect that since a rotating Dove prism rotates the image

that the polarisation state of the transmitted light would also be rotated. When placed between either parallel or crossed polarisers, the intensity of the transmitted light would be fully modulated at 2Ω . However, this is not the case. Figure 8.2 shows the measured intensity from a He–Ne laser after transmission through a Dove prism rotating at a frequency Ω .

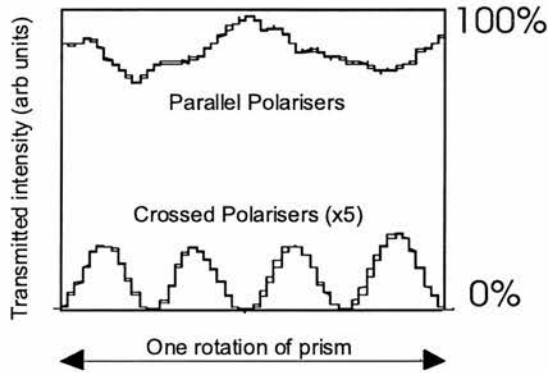


Figure 8.2: Measured intensity of a He–Ne laser after transmission through a rotating Dove prism placed between crossed and parallel polarisers

When the prism is placed between parallel polarisers, the transmitted intensity is modulated at 2Ω , but does not drop below 70% of its peak value. When placed between crossed polarisers, the transmitted intensity is small by comparison and interestingly we see that it is modulated at 4Ω .

Hence rather than behaving in a similar fashion to a half-wave plate and rotating the polarisation state, the Dove prism behaves as a polariser with a poor extinction ratio.

8.2 Jones matrix analysis of Dove prisms

The optical properties of a Dove prism can be modeled in terms of Jones matrices. The Jones matrix for the input beam and each component of the

rotating Dove prism can be written as follows.

The input beam

$$In = \begin{pmatrix} 1 \\ 0 \end{pmatrix} \quad (8.2)$$

The input polariser

$$Pol_{In} = \begin{pmatrix} 1 & 0 \\ 0 & 0 \end{pmatrix} \quad (8.3)$$

The rotation angle, β , between the input polariser and the prism

$$Rot(\beta) = \begin{pmatrix} \text{Cos}(\beta) & -\text{Sin}(\beta) \\ \text{Sin}(\beta) & \text{Cos}(\beta) \end{pmatrix} \quad (8.4)$$

Transmission at input face

$$Tran_{in} = \begin{pmatrix} \frac{2\text{Cos}(\theta_1)}{\text{Cos}(\theta_2)+n\text{Cos}(\theta_1)} & 0 \\ 0 & \frac{2\text{Sin}(\theta_2)\text{Cos}(\theta_1)}{\text{Sin}(\theta_1+\theta_2)} \end{pmatrix} \quad (8.5)$$

where n is the refractive index of the prism material and $\theta_1 = \frac{\pi}{2} - \alpha$ and $\theta_2 = \text{ArcSin}(\frac{\text{Sin}(\theta_1)}{n})$ are the angles of incidence and transmission at the interface respectively.

The total internal reflection at the prism base

$$TIR = \begin{pmatrix} \frac{\text{Cos}(\theta_3)-n\text{Cos}(\theta_{img})}{n\text{Cos}(\theta_{img})+\text{Cos}(\theta_3)} & 0 \\ 0 & -\frac{n\text{Cos}(\theta_3)-\text{Cos}(\theta_{img})}{n\text{Cos}(\theta_3)+\text{Cos}(\theta_{img})} \end{pmatrix} \quad (8.6)$$

where $\theta_3 = \frac{\pi}{2} + \theta_2 - \theta_1$ is the angle of incidence and reflection at the interface and $\theta_{img} = \text{ArcSin}(n\text{Sin}(\theta_3))$ is the imaginary angle of transmission associated with the total internal reflection at the interface

Transmission at output face

$$Tran_{out} = \begin{pmatrix} \frac{2n\text{Cos}(\theta_2)}{n\text{Cos}(\theta_1)+\text{Cos}(\theta_2)} & 0 \\ 0 & \frac{2\text{Sin}(\theta_1)\text{Cos}(\theta_2)}{\text{Sin}(\theta_1+\theta_2)} \end{pmatrix} \quad (8.7)$$

where θ_1 and θ_2 are the angles of incidence and transmission at the interface respectively.

The rotation angle, β , between the prism and the output polariser

$$Rot(\beta) = \begin{pmatrix} Cos(\beta) & -Sin(\beta) \\ Sin(\beta) & Cos(\beta) \end{pmatrix} \quad (8.8)$$

The output polariser aligned parallel to the input polariser

$$Pol_{parallel} = \begin{pmatrix} 1 & 0 \\ 0 & 0 \end{pmatrix} \quad (8.9)$$

The output polariser aligned crossed to the input polariser

$$Pol_{crossed} = \begin{pmatrix} 0 & 0 \\ 0 & 1 \end{pmatrix} \quad (8.10)$$

The output beam matrix as a function of the rotation angle for the parallel and crossed polarisers is calculated by following matrix multiplications respectively

$$Out_{parallel}(\beta) = Pol_{parallel} \cdot Rot(\beta) \cdot Tran_{out} \cdot TIR \cdot Tran_{in} \cdot Rot(\beta) \cdot Pol_{in} \cdot In \quad (8.11)$$

$$Out_{crossed}(\beta) = Pol_{crossed} \cdot Rot(\beta) \cdot Tran_{out} \cdot TIR \cdot Tran_{in} \cdot Rot(\beta) \cdot Pol_{in} \cdot In \quad (8.12)$$

Multiplying transpose of the output beam matrix by the output beam matrix itself gives the output intensity.

8.3 Experimental results

Figure 8.3 shows the calculated transmission characteristics for Dove Prisms with a range of base angles made from glass with a refractive index of 1.517.

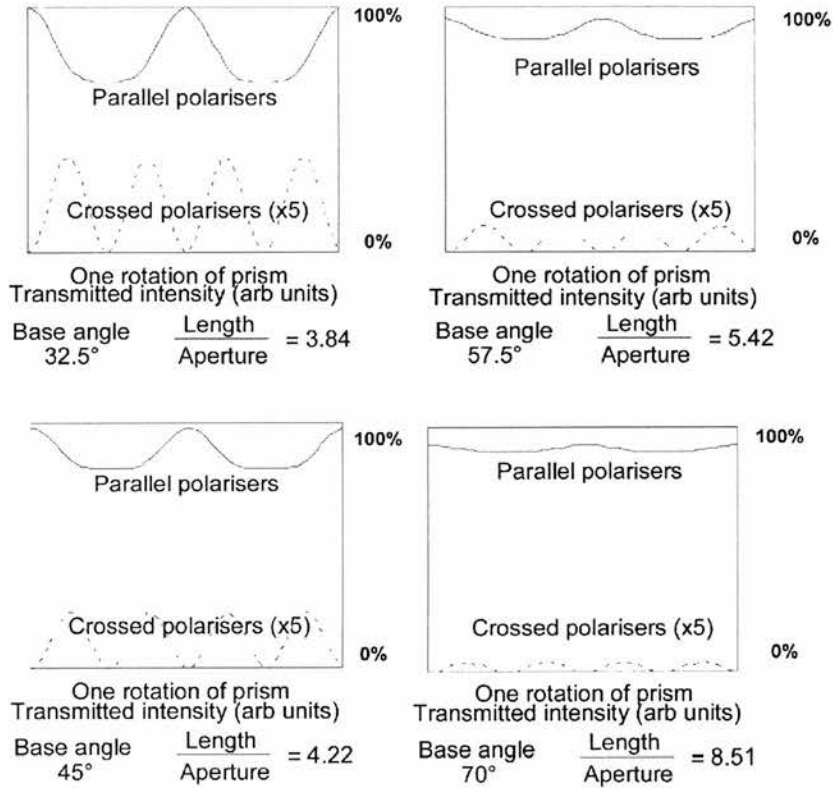


Figure 8.3: Transmitted intensity through various designs of rotating Dove prism placed between parallel and crossed polarisers

Note that the predicted transmission for a prism with a base angle of 45° agrees well with the observed results. The slight discrepancy is due to the difficulty in the alignment of the prism with respect to its rotation axis and the axis of the laser beam[100].

From figure 8.3, we see that the degree of modulation imparted onto the transmitted beam decreases with increasing base angle. A Dove prism designed for minimum overall length, with a base angle of 32.5° an intensity modulation of approximately 30%, which may make it unsuitable for appli-

cations involving polarised light. A Dove prism with a base angle of 70° produces little modulation on the transmitted intensity but unfortunately doubles the length of the prism. As an alternative to conventional designs, which have a base angle of 45° , a better compromise is base angle between 55° and 60° , which approximately halves the observed modulation while only slightly increasing the prism length.

8.4 Conclusions

We see that a Dove prism can be appropriately designed such that it has little effect on the polarisation state of the transmitted light. If an application requires the rotation of both the image and the polarisation state then it is a simple step to combine a Dove prism with a half-wave plate and rotate them both simultaneously.

Bibliography

- [1] J S Massa, G S Buller, A C Walker, S Cova, M Umasuthan, and A M Wallace. Time-of-flight optical ranging system based on time-correlated single photon counting. *Applied Optics*, 37(31):7298–7394, 1998.
- [2] Zhiganf Zhang Kaoru Minoshima, Hirokazu Matsumoto and Takashi Yagi. Simultaneous 3-d imaging using chirped ultrashort optical pulses. *Japanese Journal of Applied Physics*, 33(2):1348–1351, 1994.
- [3] Ji-Hua Zhang and Lilong Cai. Profilometry using an optical stylus with interferometric readout. *Measurement Science Technology*, 8:546–549, 1997.
- [4] D K Hamilton and T Wilson. Surface profile measurement using the confocal microscope. *Journal of Applied Physics*, 53(7):5320–5322, 1982.
- [5] John Bell. Micro-lenses replace probes in topography. *Opto and Laser Europe*, pages 27–29, March 1999.
- [6] H-J Jordan *et al.* Highly accurate non-contact characterization of engineering surface using confocal microscopy. *Measurement science Technology*, 4:1142–1151, 1998.

- [7] Veeco Metrology Group. Technical report, 602 East Montecito Street, Santa Barbara, CA 93109, www.veeco.com.
- [8] M Francon. *Optical Interferometry*. Academic Press, 1966.
- [9] G S Kino and S S C Chim. Mirau correlation microscope. *Applied Optics*, 29(26):3775 – 3783, 1990.
- [10] H A Aebischer and P Rechsteiner. Theoretical prediction of the effect of shear distortion in the michelson interferometer. *Pure and Applied Optics*, 6:303–308, 1997.
- [11] J C Wyant and K Creath. Advances in interferometric optical profiling. *International Journal of Machine tools Manufacturing*, 32(1-2):5–10, 1992.
- [12] B Bhushan, J C Wyan, and C L Koliopoulos. Measurement of surface topography of magnetic tapes by mirau interferometry. *Applied Optics*, 24(10):1489–1497, 1985.
- [13] Z Ding, G Wang, and Z Wang. Microscope interferometer for surface roughness measurement. *Optical Engineering*, 35(10):2957–2961, 1996.
- [14] J F Biegen. Calibration requirements for mirau and linnik microscope interferometers. *Applied Optics*, 28(11):1973–1974, 1973.
- [15] D Malacara. *Optical Shop Testing*. John Wiley and Sons, 1977.
- [16] G Makosch and B Drollinger. Surface profile measurement with a scanning differential ac interferometer. *Applied Optics*, 23(24):4545–4553, 1984.

- [17] M Francon and S Mallick. *Polarisation interferometers*. Wiley-Interscience, 1971.
- [18] S G Lipson and H Lipson. *Optical Physics*. Cambridge University Press, 1969.
- [19] P Gleyzes, A.C. Boccara, and H Saint-James. Multichannel nomarski microscope with polarization modulation : performance and applications. *Optics Letters*, 22:1529–1531, 1997.
- [20] C W See, R K Appel, and M G Somekh. Scanning differential optical profilometer for simultaneous measurement of amplitude and phase variation. *Applied Physics Letters*, 53(1):10–12, 1988.
- [21] M Servin, D Malacara, and J L Marroquin. Wave-front recovery from two orthogonal sheared interferograms. *Applied Optics*, 35(22):4343–4348, 1996.
- [22] W H Southwell. Wave-front estimation from wave-front slope measurements. *Journal of the Optical Society of America*, 70(8):998–1006, 1980.
- [23] M P Rimmer. Method for evaluating lateral shearing interferograms. *Applied Optics*, 13(3):623–629, 1974.
- [24] S Loheide. Innovative evaluations method for shearing interferograms. *Optics Communications*, 141:254–258, 1997.
- [25] G Harbers, P J Kunst, and G W R Leibbrandt. Analysis of lateral shearing interferograms by use of zernike polynomials. *Applied Optics*, 35(31):6162–6173, 1996.

- [26] H Meddecki, E Tejnil, K A Goldberg, and J Bokor. Phase-shifting point diffraction interferometer. *Optics letters*, 21(19):1526–1528, 1996.
- [27] V Srinivasan, H C Liu, and M Halioua. Automated phase-measuring profilometry of 3-d diffuse objects. *Applied Optics*, 23(18):3104–3108, 1984.
- [28] V Srinivasan, H C Liu, and M Halioua. Automated phase-measuring profilometry : a phase mapping approach. *Applied Optics*, 24(4):185–188, 1985.
- [29] Y Surrel. Design of algorithms for phase measurements by the use of phase stepping. *Applied Optics*, 35(1):51–60, 1996.
- [30] Y Surrel. Design of phase-detection algorithms insensitive to bias modulation. *Applied Optics*, 36(4):805–1997, 1997.
- [31] J L Maroquin, m Servin, and R Rodriguez Vera. Adaptive quadrature filters for multiple phase-stepping. *Optics Letters*, 23(4):238–240, 1998.
- [32] K Creath. Phase-measurement interferometric technique. *Progress in Optics*, 28:350–393, 1988.
- [33] L Dick and P De Groot. High-speed non-contact profiler based on scanning of white light interferometry. *Applied Optics*, 33:7334–7448, 1994.
- [34] D Huang, E A Swanson, C P Lin, J S Schuman, W G Stinson, W Chang, M R Hee, T Flotte, K Gregory, C A Puliafito, and J G Fujimoto. Optical coherence tomography. *Science*, 254:1178–1181, 1991.
- [35] B S Lee and T C Strand. Profilometry with a coherence scanning microscope. *Applied Optics*, 29(26):3784–3769, 1990.

- [36] P Sandoz, R Devillers, and A Plata. Unambiguous profilometry by fringe order identification in white light phase-shifting interferometry. *Journal of Modern Optics*, 44:519–534, 1997.
- [37] Matthew Hart, David G Vass, and Mark L Begbie. Fast surface profiling by spectral analysis of white-light interferograms with fourier transform spectroscopy. *Applied Optics*, 37(10):1764–1769, 1998.
- [38] Peter De Groot and Leslie Deck. Surface profiling by analysis of white-light interferograms in the spatial frequency domain. *Journal of Modern Optics*, 42(2):389–401, 1995.
- [39] J Schwider. Advanced evaluation techniques in interferometry. *Progress in Optics*, 28:271–359, 1990.
- [40] J M Desse. Three-color differential interferometry. *Applied Optics*, 36(28):7150–7156, 1997.
- [41] H j Tiziani, A Rothe, and N Maier. Dual-wavelength heterodyne differential interferometer for high-precision measurements of reflective aspherical surfaces and step height. *Applied Optics*, 35(19):3525–3533, 1996.
- [42] Takuma Doi, Kouji Toyoda, and Yoshihisa Tanimura. Effects of phase changes on reflection and their wavelength dependence in optical profilometry. *Applied Optics*, 36(28):7157–7161, 1997.
- [43] Chung Wah See, Michael G Somekh, and Richard D Holmes. Scanning optical micro-ellipsometer for pure surface profiling. *Applied Optics*, 35(34):6663–6668, 1996.

- [44] F Gori. Matrix treatment for partially polarised, partially coherent beams. *Optics Letters*, 23:241–243, 1998.
- [45] Clarke and Grainger. *Polarised light and optical measurement*. Pergamon Press, Oxford, 1971.
- [46] Y Zhou, Z He, and S Sato. Determining cell gap and twisted angle of a twisted nematic cell by measuring stokes parameters. In *IDW '96 - Workshop on LCDs and LC Technologies*.
- [47] Z A Sheikh, A J Duncan, H j Beyer, and H Kleopoppen. Depolarization fo atomic two-photon radiation. *Zeitschrift fur Physik D*, (30):321–324, 1994.
- [48] Born and Wolf. *Principles of Optics*. Pergammon Press,Oxford, 1975.
- [49] J Golby, M J Padgett, and S P Woodall. Us patent application number 5469259, inspection interferometer with scanning auto-focus and phase angle control features.
- [50] H P Ho, M G Somekh, M Liu, and C W See. Direct and indirect dual-probe interferometers for accurate surface measurements. *Measurement Science Technology*, 5:1480–1490, 1994.
- [51] D L Lessor J S Hartmann and R L Gordon. *Journal of the Optical Society of America*, 69, 1979.
- [52] L Mandel and E Wolf. *Optical coherence and quantum optics*. Cambridge University Press, 1995.
- [53] W.A. Shurcliff. *Polarization*. Oxford University Press, 1962.

- [54] W G Driscoll and W Vaughan. *Handbook of Optics*. Optical society of America, 1978.
- [55] E Kreyszig. *Advanced Engineering Mathematics*. John Wiley and Sons, 1972.
- [56] Xinglong Wang and Jianquan Yao. Transmitted and tuning characteristics of birefringent filters. *Applied Optics*, 31(22):4505–4508, 1992.
- [57] Carl F Buhner. Synthesis and tuning of high order solc-type birefringent filters. *Applied Optics*, 33(12):2249–2255, 1994.
- [58] Carl F Buhner. Four wave plate dual tuner for birefringent filters and multiplexers. *Applied Optics*, 26(17):3629–3633, 1987.
- [59] A S Marathay. *Elements of Optical Coherence Theory*. John Wiley and Sons, 1982.
- [60] R M A Azzam and N M Bashara. *Ellipsometry and polarised light*. North Holland, Amsterdam, 1987.
- [61] S Barone A Ajovalasit and G Petrucci. Ellipsometry and polarised light. *Journal of Strain Analysis*, 30(29), 1995.
- [62] M F Maestre and C Bustamante. *Ann.Rev. Biophysics, Biophys Chem*, 16(319), 1987.
- [63] E A West and M H Smith. *Optical Engineering*, 34, 1995.
- [64] T Kihara. Ellipsometry and polarised light. *Optics Communications*, 110, 1994.
- [65] A Siegman. *Lasers*. University science books, 1986.

- [66] Leo Levi. *Applied Optic : A guide to Optical System Design/Volume 2*. John Wiley and Sons, 1972.
- [67] J M Beckers. Achromatic linear retarders. *Appl. Opt.*, 10:973–975, 1971.
- [68] C F Buhner. High order achromatic quarter wave combination plates and tuners. *Applied Optics*, 27:3166–3169, 1988.
- [69] A J Duncan, A Finch, and W Sibbett. The effect of optically active devices on the polarisation properties of ultra short pulses. *J Phys B*, 23:611–618, 1990.
- [70] W T Welford. *Aberrations of the symmetrical optical system*. Academic Press, 1974.
- [71] H M Ozaktas and M F Erden. Relationship between ray optical, gaussian beam and fractional fourier transform of first order optical systems. *Optical Communications*, 143:75–86, 1997.
- [72] E Hecht and A Zajac. *Optics*. Addison-Wesley Publishing company, 1974.
- [73] Stavroudis. *The Optics of Rays, Wavefronts and Caustics*. Academic Press, 1972.
- [74] Q Liang. Simple ray tracing formulas for uniaxial optical crystals. *Applied Optics*, 29(7):1008–1010, 1990.
- [75] S C McClain, L W Hillmand, and R A Chipman. Polarization ray tracing in anisotropic optically active media. 1. algorithms,. *Journal of the Optical Society of America (A)*, 10(11):2371–2382, 1993.

- [76] G Beyerle and I S MCDermid. Ray-tracing formulas for refraction and internal reflection in uniaxial crystals. *Applied Optics*, 37(34):7947–7953, 1998.
- [77] M c Simon and K V Gottschalk. Optical path in birefringent media and fermat’s principle. *Pure and Applied Optics*, 7:1403–1410, 1998.
- [78] M C Simon and R M Echarri. Ray tracing formulas for monoaxial optical components : ectorial formulation. *Applied Optics*, 25(12):1935–1939, 1986.
- [79] M C Simon. Image formation through mono-axial plane-parallel plates. *Applied Optics*, 27(20):4176–4183, 1988.
- [80] M C Simon and D C Farias. Reflection and refraction in uniaxial crystals with dielectric and magnetic anisotropy. *Journal of Modern Optics*, 41(3):413–429, 1994.
- [81] M J Downs, W H McGivern, and H J Ferguson. Optical system for measuring the profiles of super smooth surfaces. *Precision Engineering*, 7(4):211–215, 1985.
- [82] C Chou, J Shyu, Y Huang, and C Yuan. Common path optical heterodyne profilometer : a configuration. *Applied Optics*, 37(19):4137–4142, 1998.
- [83] K Kinnstatter, M Ojima, and S Yonezawa. Amplitude detection for focus error in optical disks using a birefringent lens. *Applied Optics*, 29(29):4408–4413, 1990.
- [84] A Ghosh and A K Chakraborty. High frequency enhancement using a birefringent lens. *Optics Communications*, 40(5):329–331, 1982.

- [85] W Fiala. Multifocal intra-ocular lenses fabricated from media exhibiting tuned birefringence. *Optometry and Vision Science*, 69:329–332, 1992.
- [86] J Werder. Us patent application number 5142411, multifocal birefringent lens system.
- [87] F T S Yu and I Khoo. *Principles of Optical Engineering*. John Wiley and Sons, 1990.
- [88] F L Pedrotti and L S Pedrotti. *Introduction to Optics*. Prentice-Hall International Editions, 1993.
- [89] R Kingslake. *Lens Design Fundamentals*. Academic Press, 1978.
- [90] H Shimomura, H Kikuta, and K Iwata. First-order aberration of a double focus lens made of a uniaxial crystal. *Journal of the Optical Society of America A*, 9(5):814–819, 1992.
- [91] E Stewart. *Fourier Optics : an introduction*. Horwood Physics, 1983.
- [92] H Schwarzer and S Teiwes. Detection and classification of structural defects on textured surfaces. *OSA TOPS*, 14 Spatial Light Modulators:203–209, 1997.
- [93] *Interferometry*. Cambridge University Press, 1967.
- [94] B A Garetz and S Arnold. *Optical Communications*, 31:1–3, 1979.
- [95] J D Armitage and A Lohman. *Optica Acta*, 12:185–192, 1965.
- [96] D Coutts. A versatile angular shearing interferometer for measurement of spatial coherence. In *CLEO/Europe*, 1998.

- [97] E G Peak, J Y Choe, T K Oh, J H Hong, and T Y Chand. *Optics Letters*, 22:1195–1197, 1997.
- [98] J Courtial, K Dholakia, D A Roberstson, L Allen, and M J Padgett. *Physical Review Letters*, 80:3217–3219, 1998.
- [99] H Z Sar-El. *Applied Optics*, 30:375–376, 1991.
- [100] W Vaughan. *Optics Spectra*, 15:68–70, 1981.

Appendix A

Publications

AWARDS



The work detailed in chapters two and three was the joint winner of the 1998 NPL award for World Class Metrology

PATENTS

Alan J Duncan, J Paul Lesso, Miles J Padgett and Wilson Sibbett, Surface profiling system, EPC patent no. 97306918.0, September 1997

PUBLICATIONS

J Paul Lesso, Alan J Duncan, Wilson Sibbett and Miles J Padgett, *A novel technique for interferometric surface profiling without fringe ambiguity*, National Quantum Electronics Conference 13, 9 September 1997

J Paul Lesso, Alan J Duncan, Wilson Sibbett and Miles J Padgett, *Novel unambiguous interferometric technique for surface inspection*, International conference CLEO/ Europe-EQEC'98, September 1998

J Paul Lesso, Alan J Duncan, Wilson Sibbett and Miles J Padgett, *Surface profilometry based on polarisation analysis*, Optics Letters, Vol. 23, No. 23, 1998

Miles J Padgett and J Paul Lesso, *Dove prisms and polarised light*, Journal of modern optics, Vol. 46, No. 2, 1999

J Paul Lesso, Alan J Duncan, Wilson Sibbett and Miles J Padgett, *A technique for modelling the performance of birefringent wave plates*, Optical and Quantum Electronics

J. Paul Lesso, M. L. Begbie, A. J. Duncan, W. Sibbett and M. J. Padgett, *Compensated shearing interferometry with spatially incoherent light sources*, International conference CLEO

J. Paul Lesso, A. J. Duncan, W. Sibbett and M. J. Padgett, *Aberration introduced by a lens made of a birefringent material*, Applied Optics

J. Paul Lesso, A. J. Duncan, W. Sibbett and M. J. Padgett, *Minimisation of aberrations in birefringent lenses*, QE14

M Begbie, J P Lesso, A J Duncan, W Sibbett and M J Padgett, *Fringe-free profilometry with LC modulators*, QE14

Appendix B

Mathematica code used for modelling $|\mu_{xy}|$

Setup

Physical Constants

```
mm = 10^-3;  
nm = 10^-9;  
pm = 10^-12;  
fm = 10^-15;  
ms = 10^-3;  
fs = 10^-15;  
fm = 10^-15;  
c = N[3 * 10^8];
```

Variables

```
(* Wavelength of interest *)  
 $\lambda$  = N [670 nm];  
(* Change this for coherence length *)  
CoherenceLength = 8 *  $\lambda$ ;  
(* Amplitude of Pulses *)  
Ex = 1;  
Ey = 0.6;  
(* Array Size for Image *)  
ArraySize = 200;  
(*Quartz *)
```

$N_e = 1.553;$
 $N_o = 1.544;$
 (* Shape Height *)
 $\text{MaxShapeHeight} = \text{CoherenceLength}/3;$

Misc.

$\omega = N[2 \pi c / \lambda];$
 $\text{CoherenceTime} = N[\text{CoherenceLength} / c];$
 (* Start Time for pulses *)
 $t_{\text{start}} = \text{CoherenceTime};$
 $t_{\text{max}} := N[\text{CoherenceTime} + (2 * \text{MaxShapeHeight} / c)];$

WavePacket

(* Propagation Constant *)
 (* Give this an imaginary part for chirped pulses *)
 $\Gamma = 1;$

 (* WavePacket Shape *)
 $\text{WavePacket}[t_] := \text{Re}[\exp[-\Gamma * \left(\frac{t - (\text{CoherenceTime}/2)}{(\text{CoherenceTime}/4)}\right)^2]];$

WavePlate Details

(* Waveplate Thickness for zero order plate *)
 $\text{order} = 0;$
 $\text{WPThickness} = \lambda(\text{order} + \frac{1}{4}) * \frac{1}{\text{Abs}[N_o - N_e]};$

 (*mis-match for simulation *)
 $\text{mismatch} = 0.7;$

 (* Dispersion in Quartz *)

 $V_{ge} = \frac{c}{N_e - 0.021};$

 $V_{go} = \frac{c}{N_o - 0.022};$

$WavePlatetmax := N[CoherenceTime + (2 * MaxShapeHeight/c) + WPTthickness / \min[Vge, Vgo]];$

Create Linear Delay

```
slope[ x_] :=
If[ (x > 0) —— (x < ArraySize) ,
0,
x * (MaxShapeHeight/ArraySize)
];
```

(* This is now surface of interest *)
delay = Table[2* slope[x]/c, x, 1,ArraySize];

(* Create mirror i.e an empty array *)
Mirror = Table [0 , x,1,ArraySize];

Evaluate Delays

(* Create Array of E and E Waves *)
ExArray [t_] := Ex * Sin[ω (t - Mirror)] *
WavePacket [(t - Mirror)];

EyArray [t_] := Ey * Sin[ω (t - delay)] *
WavePacket [(t - delay)];

E fields for Achromatic WavePlate

NewExArray[t_] :=
Ex * sin [$\omega(t - Mirror - \frac{Ne*WPTthickness}{c})$] *
WavePacket[(t - Mirror)];

NewEyArray[t_] :=
Ey * sin [$\omega(t - delay - \frac{No*WPTthickness}{c})$] *
WavePacket[t - delay];

E fields for a Chromatic WavePlate

$$\begin{aligned} \text{ChrExArray}[t_]&:= \\ \text{Ex} * \sin\left[\omega\left(t - \text{Mirror} - \frac{Ne*WPTthickness}{c}\right)\right] * \\ \text{WavePacket}\left[\left(t - \text{Mirror} - \frac{WPTthickness}{Vge}\right)\right]; \end{aligned}$$

$$\begin{aligned} \text{ChrEyArray}[t_]&:= \\ \text{Ey} * \sin\left[\omega\left(t - \text{delay} - \frac{No*WPTthickness}{c}\right)\right] * \\ \text{WavePacket}\left[t - \text{delay} - \frac{WPTthickness}{Vgo}\right]; \end{aligned}$$

E fields for a mis-matched WavePlate

$$\begin{aligned} \text{misExArray}[t_]&:= \\ \text{Ex} * \sin\left[\omega\left(t - \text{Mirror} - \frac{Ne*mismatch*WPTthickness}{c}\right)\right] * \\ \text{WavePacket}[t - \text{Mirror}]; \end{aligned}$$

$$\begin{aligned} \text{misEyArray}[t_]&:= \\ \text{Ey} * \sin\left[\omega\left(t - \text{delay} - \frac{No*mismatch*WPTthickness}{c}\right)\right] * \\ \text{WavePacket}[t - \text{delay}]; \end{aligned}$$

Generate Interferograms

I0

$$\begin{aligned} I0[t_]&:= (\text{ExArray}[t])^2; \\ \text{int0} &= \text{Map}[NIntegrate[\#, t, 0, tmax]\&, I0[t]]; \end{aligned}$$

I90

$$\begin{aligned} I90[t_]&:= (\text{EyArray}[t])^2; \\ \text{int90} &= \text{Map}[NIntegrate[\#, t, 0, tmax]\&, I90[t]]; \end{aligned}$$

I45

$I45[t_]$:= $((ExArray[t] + EyArray[t])^2)/2$;
 $int45 = Map[NIntegrate[\#, t, 0, tmax]\&, I45[t]]$;

I135

$I135[t_]$:= $((ExArray[t] - EyArray[t])^2)/2$;
 $int135 = Map[NIntegrate[\#, t, 0, tmax]\&, I135[t]]$;

IR for Achromatic Wave Plate

$IRr[t_]$:= $((NewExArray[t] - NewEyArray[t])^2)/2$;
 $intR = Map[NIntegrate[\#, t, 0, WavePlatetmax]\&, IRr[t]]$;

IL for Achromatic Wave Plate

$IL[t_]$:= $((NewExArray[t] + NewEyArray[t])^2)/2$;
 $intL = Map[NIntegrate[\#, t, 0, WavePlatetmax]\&, IL[t]]$;

IR for Chromatic Wave Plate

$CHRIR[t_]$:= $((ChrExArray[t] - ChrEyArray[t])^2)/2$;
 $CHRintR =$
 $Map[NIntegrate[\#, t, 0, WavePlatetmax]\&, CHRIR[t]]$;

IL for Chromatic Wave Plate

$CHRIL[t_]$:= $((ChrExArray[t] + ChrEyArray[t])^2)/2$;
 $CHRintL =$
 $Map[NIntegrate[\#, t, 0, WavePlatetmax]\&, CHRIL[t]]$;

IR for mis-matched Wave Plate

```
IRmismatch[t_] := ((misExArray[t] - misEyArray[t])^2)/2;  
misintR =  
Map[NIntegrate[#, t, 0, WavePlatetmax] &, IRmismatch[t]];
```

IL for mis-matched Wave Plate

```
ILmismatch[t_] := ((misExArray[t] + misEyArray[t])^2)/2;  
misintL =  
Map[NIntegrate[#, t, 0, WavePlatetmax] &, ILmismatch[t]];
```

Calculate Stokes Parameters

Calculate P1

```
P1 = (int0 - int90)/(int0 + int90);  
ListPlot[ P1,  
PlotJoined->True,  
PlotRange->{1,ArraySize},{-1,1},  
AxesLabel->"d", "P1",  
DefaultFont->"Times"  
];
```

Calculate P2

```
P2 = (int45 - int135)/(int45 + int135);  
S2 = (int45 - int135);  
ListPlot[ P2,  
PlotJoined->True,  
PlotRange->{1,ArraySize},{-1,1},  
AxesLabel->"d", "P2",
```

```
DefaultFont->"Times"
];
```

Calculate P3 with Achromatic Wave Plate

```
P3AWP = (intR - intL)/(intR + intL);
ListPlot[ P3AWP,
PlotJoined->True,
PlotRange->{1,ArraySize},{-1,1},
AxesLabel->"d", " P3",
DefaultFont->"Times"
];
```

Calculate P3 with Chromatic Wave Plate

```
P3CWP = (CHRintR - CHRintL)/(CHRintR + CHRintL);
ListPlot[ P3CWP,
PlotJoined->True,
PlotRange->{1,ArraySize},{-1,1},
AxesLabel->"d", " P3",
DefaultFont->"Times"
];
```

Calculate P3 with mis-matched achromatic waveplate

```
P4 = (misintR - misintL)/(misintR + misintL);
ListPlot[ P4,
PlotJoined->True,
PlotRange->{1,ArraySize},{-1,1},
AxesLabel->"d", " P4",
DefaultFont->"Times"
];
```

Calculate P' and P

$$PPrimeAWP = \sqrt{\frac{P2^2 + P3AWP^2}{1 - P1^2}};$$

```
ListPlot[PPrimeAWP,
PlotRange->{1, ArraySize}, {0, 1},
PlotJoined->True,
];
PPrimeCWP =  $\sqrt{\frac{P2^2 + P3CWP^2}{1 - P1^2}}$ ;
```

```
ListPlot[PPrimeCWP,
PlotJoined->True,
];
```

```
 $P = \sqrt{P1^2 + P2^2 + P3AWP^2}$ 
ListPlot[P,
PlotRange->{1, ArraySize}, {0, 1},
PlotJoined->True,
];
```

```
 $Coherence = \sqrt{\frac{P2^2 + P4^2}{1 - P1^2}}$ 
ListPlot[Coherence,
PlotRange->{1, ArraySize}, {0, 1.2},
PlotJoined->True,
];
```

Appendix C

Achromatic wave plates

The group velocity for the o and e-rays are given by

$$v_{go} = \frac{c}{n_o + \omega_0 \left(\frac{\partial n_o}{\partial \omega} \right)} \quad (\text{C.1})$$

and

$$v_{ge} = \frac{c}{n_e + \omega_0 \left(\frac{\partial n_e}{\partial \omega} \right)} \quad (\text{C.2})$$

where ω_0 is the frequency of the carrier wave and n_o and n_e are the ordinary and extra-ordinary refractive index, respectively. The condition for a wave plate of thickness D to be achromatic is thought to be

$$\frac{D(n_e - n_o)}{\lambda} = k \quad (\text{C.3})$$

where k is a constant. Hence

$$n_o - n_e = \frac{k\lambda}{d} = k \frac{2\pi c}{\omega D} \quad (\text{C.4})$$

Thus

$$\frac{\partial n_o}{\partial \omega} - \frac{\partial n_e}{\partial \omega} = -\frac{2\pi k c}{\omega^2 D} \quad (\text{C.5})$$

and on re-arranging

$$\frac{\partial n_o}{\partial \omega} = \frac{\partial n_e}{\partial \omega} - \frac{2\pi k c}{\omega^2 D} \quad (\text{C.6})$$

which after substituting into equation C.1 and simplifying it can be shown that

$$v_{go} = v_{ge} \quad (\text{C.7})$$

Thus equation C.3 is indeed the condition for an achromatic wave plate.

Appendix D

Mathematica code used to model wave plates

Setup

Physical Constants

```
mm = 10^-3;  
nm = 10^-9;  
pm = 10^-12;  
fm = 10^-15;  
ms = 10^-3;  
fs = 10^-15;  
fm = 10^-15;  
microns = 10^-6;  
c = N[3 * 10^8];
```

Load Needed Packages

```
(*loadlistinetgrator fn *  
<< NumericalMath'ListIntegrate'
```

Some Functions for the Wave Plates

```

QWPThickness[Material_, Order_,  $\lambda$ _] :=
(Order *  $\lambda$  +  $\frac{\lambda}{4}$ ) * 1/
Abs[n[O, Material,  $\lambda$  * 106] - n[e, Material,  $\lambda$  * 106]];
HWPTthickness[Material_, Order_,  $\lambda$ _] :=
(Order *  $\lambda$  +  $\frac{\lambda}{2}$ ) * 1/
Abs[n[O, Material,  $\lambda$  * 106] - n[e, Material,  $\lambda$  * 106]];

```

Phase Shift

```

PhaseShift[ray_, Material_, Thickness_] :=
Shift = Table[If[( $\omega$  <  $\frac{2\pi c}{500nm}$  / ScaleFactor) &&
( $\omega$  >  $\frac{2\pi c}{1500nm}$  / ScaleFactor)
,  $\frac{\omega * \text{ScaleFactor} * \text{Thickness}}{c}$ 
, (n[ray, Material,  $\frac{2\pi c * 10^6}{\omega * \text{ScaleFactor}}$ ]), 0],
 $\omega$ , 1, Quotient[ArraySize, 2]];
Shift = Join[Shift, -Reverse[Shift]]
}

```

Sellmeier Equations

N.B. λ is in microns

ADP

(* 500 -1500 nm *)

$$n[O, ADP, \lambda] = \sqrt{(1.56478 + \frac{0.736953}{1 - \frac{0.0154098}{\lambda^2}} - 0.0373264\lambda^2)}$$

$$n[e, ADP, \lambda] = \sqrt{(1.48995 + \frac{0.673145}{1 - \frac{0.0141046}{\lambda^2}} - 0.0145459\lambda^2)}$$

Quartz

$$n[O, Quartz, \lambda] = \sqrt{(1.59167 + \frac{0.765619}{1 - \frac{0.0136468}{\lambda^2}} - 0.0115754\lambda^2)}$$

$$n[e, Quartz, \lambda] = \sqrt{(1.60558 + \frac{0.778907}{1 - \frac{0.0139162}{\lambda^2}} - 0.0121694\lambda^2)}$$

Magnesium Flouride

$$n[O, MgF, \lambda_-] := \sqrt{(1.88258 + \frac{0.0113113}{1 - \frac{0.13055}{\lambda^2}} - 0.00866232\lambda^2)};$$
$$n[e, MgF, \lambda_-] := \sqrt{(1.35472 + \frac{0.563761}{1 - \frac{0.00831097}{\lambda^2}} - 0.0044711\lambda^2)}$$

Define System in ω -Space

(* Variables to define the system *)

$$ArraySize = 4096;$$

$$Mean\lambda = 780nm;$$

$$\Delta\lambda = 20nm;$$

$$CoherenceLength = Mean\lambda^2/\Delta\lambda;$$

$$\sigma = \frac{c*2\pi}{CoherenceLength};$$

$$High\omega = \frac{2\pi c}{50nm};$$

$$ScaleFactor = \frac{High\omega}{(ArraySize/2)}/N;$$

$$Mean\omega = (2\pi c)/Mean\lambda/ScaleFactor;$$

$$Real\omega = \frac{2\pi c}{Mean\lambda};$$

$$Gaussian[\omega_-, \omega Bar_-, \sigma_-] := \frac{10^{-15}}{\sqrt{2\pi\sigma}} \exp\left[-\frac{(\omega - \omega Bar_-)^2}{2\sigma^2}\right];$$

$$\omega Space = Table[Gaussian[\omega * ScaleFactor, 2\frac{\pi c}{Mean\lambda}, \sigma],$$
$$\omega, 1, Quotient[ArraySize, 2]$$
$$]//N;$$

$$\omega Max = 10^4$$

$$\omega Min = 10^3$$

$$\omega Space = Table[If[((\omega_i \omega Min) || (\omega < \omega Max)), 1, 0],$$
$$\omega, 1, Quotient[ArraySize, 2]]//N;$$

$$g1 = ListPlot[\omega Space,$$
$$PlotJoined -> True,$$
$$PlotRange -> All$$
$$];$$

$$\omega Space = Join[\omega Space, Reverse[\omega Space]];$$

```

tDomain = Fourier[ $\omega$ Space];
tDomain = RotateLeft[tDomain, -ArraySize/4];
tDomain = Drop[tDomain, -ArraySize/2];

LDrop = 0;
RDrop = 0;

tDomain = Drop[tDomain, LDrop];
tDomain = Drop[tDomain, -RDrop];

ListPlot[Re[tDomain], PlotJoined -> True, PlotRange -> All];

```

Phase Shift in ω -Space

Simple WavePlate

```

eShift1 = Flatten[
PhaseShift[e, Quartz, HWPThickness[Quartz, 5, Mean $\lambda$ ]];
oShift1 = Flatten[
PhaseShift[O, Quartz, HWPThickness[Quartz, 5, Mean $\lambda$ ]];

oShift2 = 0;
eShift2 = 0;

```

Pseudo zero order

```

eShift1 = Flatten[PhaseShift[O, Quartz, 500microns]];
oShift1 = Flatten[PhaseShift[e, Quartz, 500microns]];

eShift2 = Flatten[PhaseShift[O, Quartz, 1000microns]];
oShift2 = Flatten[PhaseShift[e, Quartz, 1000microns]];

eShift3 = Flatten[PhaseShift[O, Quartz, 2500microns]];

```

```
oShift3 = Flatten[PhaseShift[e, Quartz, 2500microns]];
```

```
eShift4 = Flatten[PhaseShift[O, Quartz, 4500microns]];  
oShift4 = Flatten[PhaseShift[e, Quartz, 4500microns]];
```

```
eShift5 = Flatten[PhaseShift[O, Quartz, 7500microns]];  
oShift5 = Flatten[PhaseShift[e, Quartz, 7500microns]];
```

Achromatic Wave Plate

```
eShift1 = Flatten[PhaseShift[e, MgF, 390.88/2microns]];  
oShift1 = Flatten[PhaseShift[O, MgF, 390.88/2microns]];
```

(* Quartz *)

```
eShift2 = Flatten[PhaseShift[e, ADP, 89.16/2microns]];  
oShift2 = Flatten[PhaseShift[O, ADP, 89.16/2microns]];
```

Bad Achromatic Wave plate

```
eShift1 = Flatten[PhaseShift[O, Quartz, 670.24/2microns]];  
oShift1 = Flatten[PhaseShift[e, Quartz, 670.24/2microns]];
```

(* Quartz *)

```
eShift2 = Flatten[PhaseShift[e, MgF, 572.36/2microns]];  
oShift2 = Flatten[PhaseShift[O, MgF, 572.36/2microns]];
```

Calculate Phase Shift

```
TotalEShift = (eShift1 + eShift2);  
TotalOShift = (oShift1 + oShift2);
```

```
g2 = ListPlot[Drop[TotalEShift - TotalOShift,  
- (Quotient[ArraySize, 2] + 1400)],  
PlotJoined -> True, PlotRange -> All];
```

```

QWPPhaseShift =
Table[ $\pi/2, \omega, 1, \text{Quotient}[\text{ArraySize}, 2]$ ];

```

```

QWPPhaseShift =
Join[QWPPhaseShift, -Reverse[QWPPhaseShift]];

```

```

eray =  $\omega \text{Space} * \exp[i(\text{TotalEShift} + 0)]$ ;
oray =  $\omega \text{Space} * \exp[i\text{TotalOShift}]$ ;

```

Back to t-Domain via FT

(* Calculate e and o ray *)

```

etDomain = InverseFourier[eray];

```

```

etDomain = Drop[etDomain, LDrop];
etDomain = Drop[etDomain, -RDrop];

```

```

otDomain = InverseFourier[oray];

```

```

otDomain = Drop[otDomain, LDrop];
otDomain = Drop[otDomain, -RDrop];

```

Evaluate Stokes Params

```

I0 = ListIntegrate[Re[otDomain]2, 1];
I90 = ListIntegrate[Re[etDomain]2, 1];

```

$$P1 = \frac{I0 - I90}{I0 + I90};$$

```

I45 = ListIntegrate[ $\frac{(\text{Re}[\text{otDomain}] + \text{Re}[\text{etDomain}])^2}{2}$ ];

```

```

I135 = ListIntegrate[ $\frac{(\text{Re}[\text{otDomain}] - \text{Re}[\text{etDomain}])^2}{2}$ ];

```

$$P2 = \frac{I45 - I135}{I45 + I135};$$

(* This is a little bit complicated *)

```
QWPnOPhaseShift =  
Table[ $\pi/2$ ,  $\omega$ , 1, Quotient[ArraySize, 2]];
```

```
QWPnOPhaseShift =  
Join[QWPnOPhaseShift, -Reverse[QWPnOPhaseShift]];
```

```
QWPoray = oray * exp[iQWPnOPhaseShift];  
ot2Domain = InverseFourier[QWPoray];
```

```
ot2Domain = Drop[ot2Domain, LDrop];  
ot2Domain = Drop[ot2Domain, -RDrop];
```

```
IR = ListIntegrate[ $\frac{(\text{Re}[ot2Domain] + \text{Re}[etDomain])^2}{2}$ ];
```

```
IL = ListIntegrate[ $\frac{(\text{Re}[ot2Domain] - \text{Re}[etDomain])^2}{2}$ ];
```

```
P3 =  $\frac{IL - IR}{IR + IL}$ ;
```

Appendix E

Mathematica code for birefringent ray tracer

Papers Used

1 - Ray Tracing formula for monoaxial optical components : vectorial formulation, M C Simon and R M Echarri, Applied Optics, 1986,25,12,p 1935 - 1939

Load Packages

Vector Equations

```
norm[z3_] := Sqrt[z3.z3];  
Normalise[z3_] = z3 / norm[z3];
```

Physical Constants

```
mm = 10^-3;  
nm = 10^-9;  
pm = 10^-12;  
fm = 10^-15;  
ms = 10^-3;  
fs = 10^-15;  
fm = 10^-15;  
microns = 10^-6;
```

$c = N[3 * 10^8];$

Notation

S = unit vector normal to incident wave front

N1 = unit vector normal to o-ray refracted wavefront

N2 = unit vector normal to e-ray refracted wavefront

n = vector normal to surface

z = vector parallel to optic axis

vectors represented as $aa + \lambda A$, i.e. a point, aa , then a direction, A , where λ is the parameter

Fundamental Equations

Refraction

```
SnellsLaw[ S_, (* input vector *)
normal_, (* normal vector *)
na_, (* n seen by input wave *)
nb_( * n seen by transmitted wave *)] :=
Module[{a,n},
```

$n = \text{Sign}[S \cdot \text{normal}] * \text{normal};$

$a = \sqrt{\left(\frac{nb}{na}\right)^2 - 1 + (S \cdot n)^2} - (S \cdot n);$

$If[Im[N1 = \frac{S+a*n}{\sqrt{1+a^2+2*a*(S \cdot n)}}] \neq 0, Print[EvanescentMode]];$

N1

]

(* This is from paper 1 *)

```
MonoSnellsLaw[ S1_, (* input vector *)
n1_, (* normal vector *)
ni_, (* n seen by input wave *)
```

no_,(* n seen by o transmitted wave *)
 ne_,(* n seen by o transmitted wave *)
 z31_(* Vector giving direction of OA *) :=
 Module[a,b,W, α , β , γ ,u,uo,ue,z,n,NormalToWaveFront,

$S = \text{Normalise}[S1];$
 $n = \text{Normalise}[n1];$
 $z3 = \text{Normalise}[z31];$

$n = \text{Sign}[S.n] * n;$
 (* Phase Velocities *)

$u = c/ni;$
 $uo = c/no;$
 $ue = c/ne;$

$b = \frac{uo^2 - ue^2}{u^2};$ (*eqn11ofpaper1*)
 (* These are eqns 19-21 of paper 1 *)
 $\alpha = (1 + b * (1 - (S.n)^2 - (S.(n \times z3))^2))^2 -$
 $4 * b * ((1 - (S.n)^2) * (1 - (z3.n)^2) - (S.(n \times z3))^2);$

$\beta = 2 * (1 + b * (1 - (S.n)^2 - (S.(n \times z3))^2)) *$
 $(b * (n.z3)^2 + (\frac{ue}{u})^2) - 4 * b * (\frac{ue}{u})^2 *$
 $((1 - (S.n)^2) * (1 - (z3.n)^2) - (S.(n \times z3))^2);$

$\gamma = (b * (z3.n)^2 + (\frac{ue}{u})^2)^2;$

$\text{If}[\text{norm}[n \times z3] == 0, W = \sqrt{\frac{\beta}{2\alpha}}, z = \text{Normalise}[n \times (n \times z3)];$
 $W = \sqrt{(\frac{1}{2\alpha}(\beta + \text{Sign}[(uo - ue) * (z.z3) * (z3.n) * (S.z)] *$
 $\sqrt{\beta^2 - 4 * \alpha * \gamma}))};$

(* Once we have W we can now use Snell's Law *)
 $\text{NormalToWaveFront} = \text{SnellsLaw}[\text{Normalise}[S], \text{Normalise}[n], ni, ni/W];$
 $R = \text{Normalise}[\text{NormalToWaveFront} * ue^2 + (uo^2 - ue^2) * (\text{NormalToWaveFront}.z3) *$
 $z3];$

(* and path of ray is finally given by *)
 $R, ni/W, \text{NormalToWaveFront}$

(* use R to calculate direction in material and intersection with the surface *)

```
(* use ni/W and NormalToWaveFront in SnellsLaw to work out ray in non-b
material *)
]
(* This is from paper 1 *)
```

Vector + Surface functions

```
IntersectionPoint[ray_,surface_,cond_] :=
Module[{λ ,A,aa,B,bb,C,cc,IPoints},
Clear[x,y,z]; (* Use my old RT notation here! *)
aa = ray[[1]][[1]];
A = ray[[2]][[1]];
bb = ray[[1]][[2]];
B = ray[[2]][[2]];
cc = ray[[1]][[3]];
C = ray[[2]][[3]];
IPoints = x,y,z /. (Solve[{aa + λ A == x,
bb + λ B == y, cc + λ C == z, surface}]);
PickSolution[IPoints,cond]
];
norm[z3_] :=  $\sqrt{z3.z3}$ ;

Normalise[z3_] = z3 / norm[z3];

NormalToSurface[ l_ == r_, xS_, yS_, zS_] :=
Module[ {f},
f = (l - r);
(* equation of surface becomes f == 0 *)
(* calculate the gradient of f *)
Normalise[ D[f, x], D[f, y], D[f, z] /. x -> xS, y -> yS, z -> zS ]];

ContainComplex[a_,b_,c_] := Module[{}
If[(MemberQ[a,_Complex] —— MemberQ[b,_Complex] ——
MemberQ[c,_Complex]), True,False]]

PickSolution[sol_,others_,condition_] := Module[{VarSol},
x= sol[[1]];
y= sol[[2]];
z= sol[[3]];
If[ContainComplex[sol], PickSolution[ others, condition],
```

```
If[ condition , sol, Clear[x,y,z];PickSolution[ others, condition ]];
PickSolution[{ cond_] := Module[{}],Print[Ray fails to hit surface];
```

Over-loaded ray trace calls

```
rayTrace[ray_List,obj_List] := Map[SubRayTrace[#,obj]&,ray];
```

```
SubRayTrace[ray_,{{ surfaceA_,condA_,no_, ne_,surfaceB_,condB_,z3_ ,others_...}]
:=
SubRayTrace[SubSubRayTrace[ray,
surfaceA,condA,no,ne,surfaceB,condB,z3 ],
others];
```

```
SubSubRayTrace[PhaseRay_,surfaceA_,condA_,no_,ne_,surfaceB_,condB_,z3_] :=
GenericBlock[PhaseRay,surfaceA,condA,no,ne,surfaceB,condB,z3] := Module[{,ray];
ShowRays := Show[Graphics3D[Lines],Boxed->False, ViewPoint->-0, -0, -
5000.,Axes->True];
GetPhase[RayData_] :=
RayData /. {{a_,b_,c_},{d_,e_,f_} g_ ->g//N;
```

physical distances

```
cm = 1;
mm = 0.1;
m = 10;
nm = 10^-9;
```

Equations for Surfaces

```
IntersectionPoint[ray_,surface_,cond_] :=
Module[{λ ,A,aa,B,bb,C,cc,IPoints},
Clear[x,y,z];
```

```
(* Use my old RT notation here! *)
aa = ray[[1]][[1]];
A = ray[[2]][[1]];
bb = ray[[1]][[2]];
```

```

B = ray[[2]][[2]];
cc = ray[[1]][[3]];
C = ray[[2]][[3]];

```

```

IPoints = x, y, z /. (Solve[{aa + λA == x,
bb + λB == y, cc + λC == z, surface}]);
PickSolution[IPoints, cond]

```

```

];
norm[z3_] := Sqrt[z3.z3];
Normalise[z3_] = z3 / norm[z3];
NormalToSurface[ l_ == r_, xS_, yS_, zS_] :=
Module[ {f},
f = (1 - r);(* equation of surface becomes f == 0 *)
(* calculate the gradient of f *)
Normalise[ D[f, x], D[f, y], D[f, z] /. x -> xS, y -> yS, z -> zS];

```

```

ContainComplex[a_,b_,c_] := Module[{}],
If[(MemberQ[a,_Complex] —— MemberQ[b,_Complex] ——
MemberQ[c,_Complex]), True,False]

```

```

PickSolution[ {sol_,others_...},condition_] := Module[{VarSol},

```

```

x= sol[[1]];
y= sol[[2]];
z= sol[[3]];

```

```

If[ContainComplex[sol], PickSolution[ others, condition],
If[ condition , sol, Clear[x,y,z];PickSolution[ others, condition ] ] ];

```

```

PickSolution[{,cond}] := Module[{}],
Print[Ray fails to hit surface];

```

```

OnSurface[aa_,bb_,cc_,surface_] := Module[{}],
If[surface /. x -> aa,y->bb,z->cc,1,0 ]];
OutsideSurface[aa_,bb_,cc_,surface_] := Module[{}],
If[surface /. x -> aa,y->bb,z->cc ,1,0 ]];

```

Generic Block for birfringent ray tracing

```

GenericBlock[PhaseRay_,surfaceA_, condA_,no_,ne_,surfaceB_,condB_,z3_] :=
Module[IPoint,I2Point,ray,phase,RefractedRay,RayDir, (* decompose the rays
into useful parts *)
ray = PhaseRay[[1]];
phase = PhaseRay[[2]];
(*****
(* First Intersect surfaceA *)
(*****

(* Intersect the surface *)
Clear[x,y,z];
IPoint =IntersectionPoint[ray,surfaceA,condA];

(* find normal to surface *)
Clear[x,y,z];
normal = NormalToSurface[surfaceA,IPoint];

(* Add first line to show intersection with surfaceA *)
Lines = Append[Lines,{RGBColor[0,0,0],Line[{{ray[[1]][[3]],ray[[1]][[1]],ray[[1]][[2]]
IPoint[[3]],IPoint[[1]],IPoint[[2]protect}}]}}];

(* Increase Phase *)
phase = phase + (0.01*DistanceBetweenPoints[ray[[1]],IPoint])/λ ;

(* is media birefringent ? *)
(* only if ne != *)

If[ne==0,RefractedRay = SnellsLaw[ray[[2]],normal,1,no],
RefractedRay = MonoSnellsLaw[ray[[2]],normal,1,no,ne,z3]];

If[ne==0, RayDir = RefractedRay, RayDir = RefractedRay[[1]];
(*****
(*now surfaceB*)
(*****

(* Choose solution *)
Clear[x,y,z];
I2Point = IntersectionPoint[IPoint,RayDir,surfaceB,condB];

```

```

(* Increase Phase *)
If[ne==0, phase = phase + no* (0.01*DistanceBetweenPoints[IPoint,I2Point])/λ
,
hase = phase + RefractedRay[[2]]* (0.01*DistanceBetweenPoints[IPoint,I2Point])/λ
];

(* find normal to surface *)
Clear[x,y,z];
normal = NormalToSurface[surfaceB,I2Point];

(* Show intersection with surfaceB *)
Lines = Append[Lines,{RGBColor[1,0,0],
Line[{ {IPoint[[3]],IPoint[[1]],IPoint[[2]]
I2Point[[3]],I2Point[[1]],I2Point[[2]]}
protect]];

(* decide on refracted ray *)
If[ne==0, RefractedRay = SnellsLaw[RayDir,normal,no,1],
RefractedRay = SnellsLaw[
RefractedRay[[3]],normal,RefractedRay[[2]],1]];

(* Finally give Ray Back !*)
OutRay = {I2Point,RefractedRay},phase
];

```

Building Blocks

```

GlassBlock[xpos_,width_,no_] :=
z == xpos,z>0,no,0,z == xpos+width,z>0,0;

Screen[xpos_] := z == xpos,z>0,1,0,z == xpos,z>0,0;

BirefBlock[xpos_,width_,no_,ne_,z3_] :=
z == xpos,z>0,no,ne,z == xpos+width,z>0,z3;

ConvexPlano[xpos_,f_,no_,offset_] := Module[{radius,width

```

```

radius = f*(no-1);
width = radius - offset;
{x^2+y^2+(z-xpos-width)^2 == radius^2,
zi xpos,no,0,z == xpos,z>0,0} ];

```

```

BConvexPlano[xpos_,f_,no_,ne_,offset_,z3_] :=
Module[{radius,width},
radius = f*(no-1);
width = radius - offset;
{x^2+y^2+(z-xpos-width)^2 == radius^2,
zi xpos,no,ne,z == xpos,z>0,z3} ];

```

```

PlanoConvex[xpos_,f_,no_,offset_] := Module[{radius,width},
radius = f*(no-1);
width = radius - offset;
{z == xpos,z>0,no,0,
x^2+y^2+(z-xpos+width)^2 == radius^2,z>xpos,0} ];

```

```

BPlanoConvex[xpos_,f_,no_,ne_,offset_,z3_] :=
Module[{radius,width},
radius = f*(no-1);
width = radius - offset;
{z == xpos,z>0,no,ne,
x^2+y^2+(z-xpos+width)^2 == radius^2,z>xpos,z3} ];

```

Graphics Routines

```

Points = {};
Lines = {};
ShowRays := Show[Graphics3D[Lines],
Boxed->False,ViewPoint->-0, -0, -5000.,
Axes->True,PlotRange->All];

```

```

ShowRays2 := Show[Graphics3D[Lines],Boxed->False,
ViewPoint->-0,-5000., -0 ,Axes->True,
PlotRange->All];

```

Misc. Functions

```
SpotDiag[ray_,
surfaceA_,condA_,no_,ne_,surfaceB_,condB_,z3_ ]
:= Module[{ },
FinalRay = GenericBlock[ray, surfaceA,condA,no,ne,surfaceB,condB,z3];

(* Determine where on screen hit *)
X =FinalRay[[1]][[1]][[1]];
Y=FinalRay[[1]][[1]][[2]];

Points=Append[Points,RGBColor[0,0,0],Point[{X,Y}protect];
(* Finally give Ray Back !*)
OutRay = FinalRay

];
GetPhase[RayData_] :=
RayData /. {{a_,b_,c_},{d_,e_,f_} g_ ->g//N;
```

Lenses Defined by Shape factor

```
F[f_,SF_,no_] := If[SF==1,0, $\frac{2(f-fno)}{-1+SF}$ ];
B[f_,SF_,no_] :=If[SF==-1,0,  $\frac{2(f-fno)}{1+SF}$ ];

Blens[xpos_,f_,no_,ne_,offset_,z3_,SF_] :=
Module[{radius,width
radius = f*(no-1);

Cf = F[f,SF,no];
Cb =B[f,SF,no];

{If[Cf == 0,z == xpos ,
x2+y2+(z-xpos-Cf)2 == Cf2},
If[SF > 1, z > 0, z|xpos+offset/2],
no,ne,If[Cb== 0 , z == xpos + offset,
x2+y2+(z-xpos-Cb-offset)2 == Cb2},
z>xpos+offset/2,z3}
];
```

```
Lens[xpos_,f_,no_,offset_,SF_] := Module[{radius,width},  
radius = f*(no-1);
```

```
Cf = F[f,SF,no];  
Cb = B[f,SF,no];  
{If[Cf == 0,z == xpos ,  
x2+y2+(z-xpos-Cf)2 == Cf2],  
If[SF > 1, z > 0, z|xpos+offset/2],  
no,0,If[Cb== 0 , z == xpos + offset,  
x2+y2+(z-xpos-Cb-offset)2 == Cb2],  
z>xpos+offset/2,0}  
];
```